

Abstract

Time-bin Entanglement Between Remote Superconducting Cavity Resonators

Evan Zalys-Geller

2022

Generation of entanglement between qubits connected by a lossy channel is an important primitive for large-scale, modular, quantum information processing. Photon loss errors occurring in the channel can be detected by a time-bin entanglement protocol. We present an experiment for time-bin, pitch-and-catch entanglement between remote superconducting cavities. A particular four-wave mixing process performs an entangling gate between a flying photon, source/target system, and an ancillary mode. Through local measurement of the ancillary modes, we detect photon loss errors in the channel and successfully herald the creation of entangled Fock states between the remote cavities. We demonstrate experimentally that the fidelity of the generated entangled state, after post-selecting for no photon loss, is limited mainly by the coherence times of the ancillary modes, as predicted by theory. Our experiment could be improved to generate entanglement with higher fidelity.

Time-bin Entanglement Between Remote Superconducting Cavity Resonators

A Dissertation
Presented to the Faculty of the Graduate School
of
Yale University
in Candidacy for the Degree of
Doctor of Philosophy

by
Evan Zalys-Geller

Dissertation Director: Michel Devoret

May, 2020

Copyright © 2020 by Evan Zalys-Geller
All rights reserved.

Contents

1	Introduction and Overview	1
1.1	The importance of modularity in quantum computation	1
1.2	Circuit-QED is well-suited for the modular architecture	3
1.3	Photon loss error detection with time-bin encoding	5
1.4	Dissertation overview	6
2	Quantum Processing Modules	8
2.1	The transmon qubit/cavity architecture	8
2.1.1	The Josephson junction in the transmon regime	8
2.1.2	Coupling a transmon to a cavity	12
2.1.3	Storage cavity	15
2.2	Theory of parametric drives	16
2.2.1	Synthesizing a SWAP gate between two internal modes	19
2.2.2	Synthesizing a generalized SWAP gate between three modes	21
2.2.3	Stationary-to-propagating conversion	23
2.3	Our quantum processing module suitable for demonstrating photon-loss ro- bust remote entanglement	23
2.3.1	Long-term quantum information storage with a post cavity embedded in a waveguide	23
2.3.2	Frequency tuning a 3D post cavity	25
2.3.3	Reducing the influence of higher cavity modes	26
2.3.4	Bridge-transmon architecture	27

2.3.5	Driving a transmon at the base of a waveguide	27
2.4	Experimental characterization of our quantum processing modules	29
2.4.1	Coupling between internal degrees of freedom	31
3	Opening the Module to the Network: Q-Switching	35
3.1	Tunable Q-switch: Theory	36
3.1.1	High-level overview of Q-switching	36
3.2	Implementing Q-switching in our quantum processing module	41
3.2.1	Stark shift compensation	42
3.2.2	Dispersion compensation	45
3.2.3	Drive induced decoherence	46
3.2.4	Experimental verification of Q-switching and extraction of process susceptibility to drive	48
4	Single Photon Transfer Between Two Nodes of a Quantum Network: Principle and Practical Realization	52
4.1	A survey of different methods for quantum network connectivity	53
4.2	Two modules and a one-way channel: Cascaded quantum systems	55
4.2.1	Schemes for the connection of two quantum processing modules	56
4.2.2	Theory of cascaded microwave quantum systems	57
4.3	Simulating the full cascaded system	61
4.3.1	Benchmarking our quantum channel	62
4.4	Synthesis of optimal pitch and catch drive waveform	64
4.4.1	Compensating for Stark shift and dispersion	66
4.4.2	Pulse truncation	67
4.5	Experimental results and analysis	68
5	Time-Bin Entanglement	70
5.1	Introduction to our time-bin entanglement protocol	70
5.2	Implementation of time-bin entanglement	74
5.3	Experimental verification of time-bin entanglement	78

5.3.1	Joint qubit readout and tomography	78
5.3.2	Postselection errors	81
5.3.3	Two-qubit tomography	82
5.3.4	Gate verification	84
5.3.5	Entanglement verification protocol: Experimental results	86
6	Perspectives of This Work Towards Future Entanglement Experiments	89
6.1	Incremental improvements of the experiment	90
6.2	Scaling time-bin entanglement	90
A	Wiring of the Experimental Setup	92
A.1	First-round drives	92
A.2	Second-round drives	92
B	Exact Pitch-Catch Solution for the Envelope	97
	Bibliography	101

List of Figures

1.1	Modular architecture	2
1.2	Cavity QED and circuit QED	4
1.3	Time-bin encoding	5
2.1	Transmon qubit	9
2.2	Gates realized by parametric drives	19
2.3	Quantum processing module diagram	24
2.4	Coherence and decay measurements of Alice and Bob modes	30
2.5	Rabi oscillations between qubit and storage modes of Alice system	32
2.6	Characterization of SWAP gate between qubit and storage modes	33
3.1	Tunable coupling	36
3.2	Driving $\mathbf{q}^\dagger \mathbf{b} + \text{h.c.}$ with dissipation on \mathbf{b}	38
3.3	Driving $\mathbf{b}^\dagger \mathbf{q}^\dagger \mathbf{s} + \text{h.c.}$ with dissipation on \mathbf{b}	39
3.4	Stark shifting of modes: diagram	42
3.5	Stark shift compensation: Experimental data	43
3.6	Dispersion compensation: experimental data	45
3.7	Drive induced decoherence	47
3.8	Verification of Stark shift compensation	48
3.9	Extraction of g vs. drive amplitude	49
4.1	Concurrent and sequential remote entanglement	53
4.2	Direct connection between two quantum processing modules	56
4.3	Cascading microwave cavities using a circulator	58

4.4	Measuring quantum efficiency of a cascaded quantum system	62
4.5	Cavity Stark shift due to drive on buffer modes	63
4.6	Mode populations during photon transfer	68
5.1	High level schematic of protocol	71
5.2	Joint readout for a cascaded circuit QED system	78
5.3	Joint readout verification	80
5.4	Postselection readout	81
5.5	Entanglement verification protocol	86
5.6	State tomography of heralded and unheralded protocol	87
A.1	Dilution refrigerator wiring	93
A.2	System block diagram for pump generation	94

Nomenclature

Acronyms

ADC Analog to Digital converter

DAC Digital to Analog converter

HEMT High Electron Mobility Transistor

POVM Positive Operator Valued Measure

QED Quantum Electrodynamics

RWA Rotating Wave Approximation

SNAIL Superconducting Nonlinear Asymmetric Inductive eLement

SNR Signal-to-Noise Ratio

SPA SNAIL Parametric Amplifier

VNA Vector Network Analyzer

Constants

\hbar Reduced Planck Constant

Φ_0 Magnetic Flux Quantum

ϕ_0 Reduced magnetic flux quantum

e Electron charge

k_B Boltzmann constant

Symbols

\bar{n} Average photon number

\mathcal{F}_i POVM for measurement i

φ Phase difference operator

χ Dispersive shift between a qubit and buffer cavity

χ_{ij} Generalized dispersive shift between modes i and j

χ_{qq} Transmon qubit anharmonicity

Δ_i Detuning from mode i

Δ_m Resonant Stark shift due to a drive near the buffer mode

$\Delta_{q,b,s}$ Stark shift on the qubit, buffer, or storage mode due to a drive

η Quantum efficiency of a channel

η Quantum measurement efficiency

Γ Decay rate

Γ_ϕ Dephasing rate

Γ_m Measurement induced decay rate rate

Γ_m Measurement induced dephasing due to a drive near the buffer mode

κ_i Cavity/resonator bandwidth of buffer mode for module i

$|0\rangle$ Vacuum state or Fock state with zero photon number

$|i\rangle$ Fock state of photon number i

$\langle i \rangle$ Average value of i

- $\mathbf{a}_{\text{in}}^i, \mathbf{a}_{\text{out}}^i$ Input and output field for mode \mathbf{a} residing in module i
- $\mathbf{b}_i, \mathbf{b}_i^\dagger$ Annihilation and creation operators for the buffer mode of the i module
- $\mathbf{H}_{\text{drive}}$ Drive Hamiltonian
- \mathbf{O} Observable
- $\mathbf{q}_i, \mathbf{q}_i^\dagger$ Annihilation and creation operators for the qubit mode of the i module
- $\mathbf{s}_i, \mathbf{s}_i^\dagger$ Annihilation and creation operators for the storage mode of the i module
- \mathbf{U} Unitary operation
- $\mathbf{X}, \mathbf{Y}, \mathbf{Z}$ Pauli operators or matrices for a single qubit
- \mathcal{C} Concurrence
- $\mathcal{D}[\cdot]$ Dissipation superoperator
- ω Angular frequency
- ω_1, ω_2 Qubit drive and buffer drive frequencies for $\mathbf{b}^\dagger \mathbf{q} + \text{h.c.}$ process
- ω'_1, ω'_2 Storage drive and buffer drive frequencies for $\mathbf{s}^\dagger \mathbf{q} + \text{h.c.}$ process
- ω_3 Drive frequency for $\mathbf{b}^\dagger \mathbf{q}^\dagger \mathbf{s} + \text{h.c.}$ process
- ω_b^i Buffer mode frequency for the i module
- ω_q^i Qubit mode frequency for the i module
- ω_s^i Storage mode frequency for the i module
- ψ Wave function
- ρ Density matrix
- σ Standard deviation of a Gaussian distribution or a Gaussian pulse
- $\text{diag}(M)$ Column vector of the diagonal elements of M

tr	Trace of a matrix
$\tilde{\chi}$	Stark shift calibration referred to DAC voltage
$\tilde{V}(t)$	Complex voltage corresponding to DACs controlling in-phase and quadrature component of drive signal
$\varphi_{b,q,s}$	Zero point fluctuations corresponding to the buffer, qubit, or storage mode
ξ'_1, ξ'_2	Displacement due to qubit drive and storage drive for $\mathbf{s}^\dagger \mathbf{q} + \text{h.c.}$ process
ξ_1, ξ_2	Displacement due to qubit drive and buffer drive for $\mathbf{b}^\dagger \mathbf{q} + \text{h.c.}$ process
ξ_3	Displacement due to drive for $\mathbf{b}^\dagger \mathbf{q}^\dagger \mathbf{s} + \text{h.c.}$ process
E_C	Charging energy
E_J	Josephson energy
F	Fidelity
$f = \frac{\omega}{2\pi}$	Frequency
g_2	Strength of $\mathbf{b}^\dagger \mathbf{q} + \text{h.c.}$ process
g'_2	Strength of $\mathbf{s}^\dagger \mathbf{q} + \text{h.c.}$ process
g_3	Strength of $\mathbf{b}^\dagger \mathbf{q}^\dagger \mathbf{s} + \text{h.c.}$ process
I_0	Critical current of a Josephson junction
P_0, P_1	Probability of measuring $ 0\rangle$ or $ 1\rangle$ in a particular mode
P_{00}	Probability of measuring that both the Alice and Bob qubits are in their ground states, using a joint measurement
$R_{X,Y}^i(\theta)$	Single qubit rotation around X or Y axis of angle θ , for qubit in module i
$S_{\text{lines}}[\omega]$	Response function of the lines from DAC to qubit
T_1	Qubit relaxation time

T_ϕ	Qubit dephasing time
T_m	Measurement time
$T_{1,\text{Cav}}$	Storage cavity lifetime
T_{2E}	Qubit Hahn-echo decoherence time
T_{2R}	Qubit Ramsey decoherence time
I,Q	In-phase and quadrature components of a microwave signal

Acknowledgements

I would like to first thank my advisor, Michel Devoret, for having me as his student. Michel's boundless curiosity and understanding of the scientific method at every level are truly inspirational. Talking to Michel, you have the impression that every physics problem can be tackled with sufficient imagination and intuition. Any time I found my head stuck in the clouds of abstraction, Michel always guided me back to earth with humble, patient understanding grounded in lucid physical analogies. I could not have hoped for a better person to shepherd me into the world of physics. I will always cherish our whirlwind conversations that bounced from stochastic master equations to Deluze to black holes.

I would also like to thank the other members of my dissertation committee. Rob Schoelkopf's extensive understanding of both experimental physics and engineering is truly greater than the sum of its parts. Rob has a disciplined understanding of how to approach a problem in a systematic way, and an encyclopedic knowledge of how to approach problems the "right" way. Talking to Rob you understand that every experiment is built on a sound foundation of well thought out engineering practices. It has also been a privilege to serve as a teaching assistant for Rob's microwave electronics course. Dan Prober is a model educator. I have found it nearly impossible to pass his office without learning something about the history of science or engineering. I deeply appreciate our conversations about ham radio and the spirit of tinkering with electronics.

I was incredibly fortunate to have worked closely with postdocs Michael Hatridge, Shyam Shankar, and Philippe Campagne-Ibarcq. Michael has the invaluable ability to slash through the weeds of a complex problem and quickly arrive at a working, elegant solution. Shyam seems to carry with him an aura that untangles the knots of whatever you

happen to be troubled with. I fondly remember the times we sat together with a pen and notepad like walks in the park. The two of them made an incredible team, and I'm a far better physicist today for their loving guidance in the earlier stages of my PhD. In the latter half of my PhD, Phillippe's boundless energy, intellect, and passion were a true inspiration. I cherish the memories of rapidly bouncing ideas back and forth with him about error correction and entanglement. I will forever strive to bring his level of electric enthusiasm to my pursuits.

I want to thank Anirudh Narla for teaching me how to build and run a quantum computer. Anirudh methodically and systematically taught me all the important little details – what flux to use for stainless coax, how to fabricate a transmon, what to do if you get an ice plug in the dilution unit. Anirudh gives the well deserved impression that he has his experiment under control. His patience and care left me feeling capable of supporting any low temperature physics experiment. I also want to thank Luigi for his support of all the experimental activity on the fourth floor. One can't make a high quality qubit without a very well maintained fab. The fact that one rarely need think much about the details of Josephson Junction fabrication while working with the tools he maintains is a true testament to his skill and hard work. On the occasion that some element of fabrication was not working, Luigi's laugh and stories were always the perfect salve for the rough patches.

In addition to all of those listed above, I've enjoyed the friendship of of many others who worked in Becton, including Jacob Blumoff, Teresa Brecht, Ben Chapman, Kevin Chou, Yiwen Chu, Alec Eickbusch, Yvonne Gao, Sumita Ghosh, Alex Grimm, Reinier Heeres, Vijay Jain, Prash Kharel, Angela Kou, Zaki Leghtas, Brian Lester, Zlatko Minev, Mazyar Mirrahimi, Shantanu Mundhada, Wolfgang Pfaff, Kyle Serniak, Vladimir Sivak, Clarke Smith, Katrina Sliwa, Matt Reagor, Phil Reinhold, Steven Touzard, Jaya Venkatraman, Uri Vool, and Xu Xiao.

I'm endlessly grateful to my parents, Elena and Alan, for all their encouragement and support of my interests. I can't imagine I would have turned out the same without the time spent with my father in his ham radio shack, soldering gizmos together, or reading through Horowitz and Hill together. Finally, I want to thank my partner Caitlin for her love and support through thick and thin. Thank you for being my light in the darkness.

Chapter 1

Introduction and Overview

1.1 The importance of modularity in quantum computation

A large-scale, fault-tolerant, gate-based quantum computer would be a highly complex machine, leading us to ask: How should one tackle the problem of designing a complex system that must behave quantum-mechanically even at the level of signals and control variables? One strategy, pervasive in the discipline of classical engineering, and emergent in the natural world, is to split the system into discrete modules with separable optimization strategies. Modules, viewed externally, perform tasks according to simple rules, even though their internal behavior may be rather complicated. For instance, an operational amplifier may be implemented using upwards of twenty transistors [1], though the circuit in totality is well approximated by one single law. An electrical engineer may build a circuit from many operational amplifiers without concerning herself with what any particular transistor within an operational amplifier is doing. In biology, the organelles of a cell have seemingly well-separated functions implemented internally by complex chemical processes. Reasoning about a system of connected modules reduces to reasoning about how their interfaces react. It is this hiding of internal complexity that makes reasoning about such modular complex systems feasible.

The construction of a large-scale quantum computer is a monumentally complex task. Reasoning about the interactions and imperfections of thousands of qubits is not straightforward. The modular approach we are following here proposes that this task becomes easier

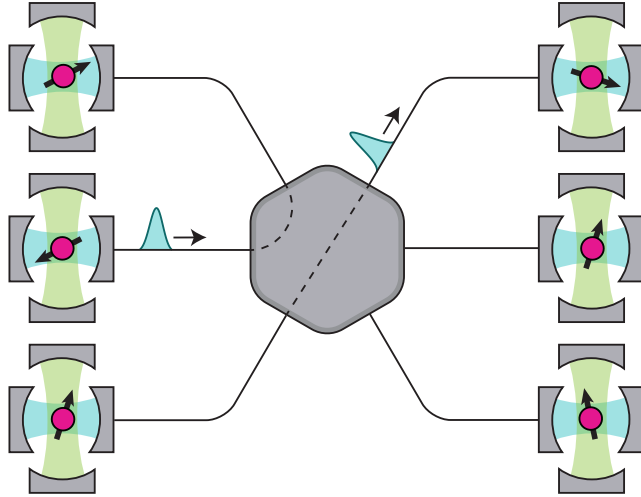


Figure 1.1: **Modular architecture** | We consider a quantum network consisting of quantum processing modules connected by a quantum router (rounded hexagon.) Each quantum processing module contains a storage cavity (vertical Fabry-Perot with green field), which is well isolated from the environment but strongly coupled to a communication qubit (pink circle with black arrow). A buffer cavity (horizontal Fabry-Perot with blue field) is coupled to the qubit as well as a communication channel (black line). A configurable quantum router (grey hexagon) then routes messages (blue wavepackets) between any pair of quantum processing modules on demand.

if one constructs a quantum computer in a modular fashion [2, 3]. A modular quantum computer consists of quantum processing modules connected by a router module, where the job of the quantum processing module is to store, recall, and manipulate quantum information in a robust manner, and the job of the router module is to establish connections between any two modules on demand for the generation of quantum entanglement. These connections involve only linear couplings between electromagnetic modes. It is this linear character of inter-module connections that ensures that each module can be tested separately before being assembled to form a complex quantum system. Obviously, no system spontaneously retains quantum information with perfect fidelity, for indefinite periods. It is through the magic of error correcting codes that an error-prone physical system may become a more suitable vessel for quantum information. In the following, we refer to logical qubits, two-state manifolds of a larger Hilbert space that have a higher level of protection against decoherence than the two lowest energy levels in the same Hilbert space [4]. These logical qubits are then placed in individually shielded modules to ensure they are well controlled,

and well isolated to mitigate crosstalk and decoherence. Communication between the logical qubit and the outside world is done in a carefully engineered manner. In the modular architecture pictured in 1.1, the logical qubit encoded in the Hilbert space of the storage cavity (green Fabry-Perot) is only allowed to interact with the communication channel using the qubit (pink circle with slanted arrow) and buffer cavity (blue Fabry-Perot), protecting the logical qubit, but presenting a well-controlled interface for the transmission and reception of quantum information.

Quantum information exported from the module must then face the imperfections of the communication channel. Cables, connectors, and switches in the real world are not perfect conduits for quantum information. In our approach, generating high-quality entanglement between quantum processing modules through imperfect channels is a responsibility shouldered by the quantum processing modules themselves. In this dissertation, we present a quantum processing module that demonstrates this functionality. Through time-bin encoding [5, 6, 7], losses due to imperfections of a channel are detected and weeded out. We demonstrate such time-bin encoding in a system that has already proven itself as an excellent platform for a logical qubit [8], the architecture of circuit quantum electrodynamics, circuit QED.

1.2 Circuit-QED is well-suited for the modular architecture

The modular architecture detailed previously requires quantum processing modules that have well controlled interactions between degrees of freedom internal to the module and the environment at large. For instance, a control signal which was intended to have an effect on one module must have minimal effects on neighboring modules. Additionally, for a qubit to be long-lived, its coupling to radiation modes must be well controlled [10]. One possible approach to designing a quantum computer is to use the atomic spins, Nature’s qubits. The weak interaction between the electromagnetic field and atomic spins is both a blessing and a curse, affording atomic qubits long lifetimes with the caveat of slow gates. The field of cavity QED [11, 12] was born of using a resonant cavity to enhance this coupling, wherein an atom embedded within a cavity interacts with the light flying through it, multiplying the

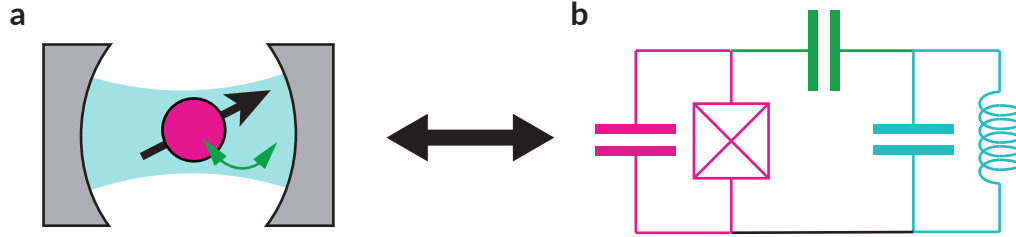


Figure 1.2: **Cavity QED and circuit QED** | The design for a superconducting two-level atom coupled to a linear cavity inspired by experiments in cavity QED (left), in which a natural atom (green) interacts with the quantized light of an optical cavity (blue) as it flies through it. In circuit QED (right) the atom is replaced by a nonlinear artificial atom while the optical cavity is replaced by a linear cavity. Both objects are macroscopic and coupled by a capacitor (green), which allows for independent control of the frequencies and coupling between both modes. Figure and caption adapted from Vool [9]

interaction strength by the quality factor of the cavity.

Inspired by cavity QED, circuit QED [13] couples a superconducting artificial atom to a cavity. The effective spin-1/2 system of this artificial atom corresponds not to an atomic degree of freedom, but to the quantum degrees of freedom of the electromagnetic field in a macroscopic superconducting circuit. Such circuits are built from combinations of lumped circuit elements. Choice of elements and their parameters determines the frequencies and internal impedances of modes of the artificial atom, leading to a large variety of devices [14, 15, 16]. Of particular interest are devices where the internal impedance of the artificial atom is well matched to the vacuum impedance, yielding strong coupling with electromagnetic modes. In contrast to atomic qubits, such atoms in free space have short lifetimes due to their large dipole moments, but the strong coupling affords nanosecond time-scale gates.

The key insight of circuit QED is to embed this *strongly* interacting artificial atom in an *off-resonant* cavity to prevent the atom from radiating, in contrast to cavity QED, which uses this cavity to enhance the coupling. In addition to providing protection for the qubit, the cavity also acts as a qubit-state dependent phase shifter [17]. Light traveling through the cavity thus acquires qubit state information, which may be decoded by heterodyne detection.

Superconducting qubits may serve dual usage as both storage elements for quantum information, as well as a source of nonlinearity for the generation of parametric interactions, controlled by strong drives [18, 19, 20]. Such interactions are useful for implementing gates

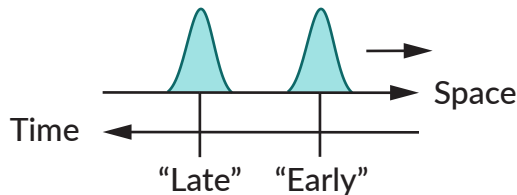


Figure 1.3: **Time-bin encoding** | Time-bins are quasi-orthogonal wavepacket envelopes, which form the two quantum states of a protected flying qubit when occupied by a single photon. In this picture we imagine the wavepackets propagating to the right in real space. The photon can be in either the early or late state or any superposition thereof. Figure and caption adapted from Weihs et al. [25].

between modes within the module. In particular, one may swap half an excitation from the qubit into a buffer cavity, where the excitation will leak out into the attached transmission line [21, 22, 23, 24], yielding a qubit entangled with a flying photon. Importantly, we are also afforded the reverse process, where a photon impinging upon the buffer cavity may be completely and efficiently absorbed into the qubit, providing a means for the generation of entanglement between remote modules in a pitch-and-catch remote entanglement scheme. Crucially, such a scheme is not robust to losses in the transmission line. In this dissertation, we extend pitch-and-catch remote entanglement to form a photon-loss robust scheme.

1.3 Photon loss error detection with time-bin encoding

Quantum error detection requires that the consequences of errors can be separated from the intended message emitted by the sender, by the message recipient. Let us suppose two parties, Alice and Bob, wish to communicate one bit of quantum information through a channel. Let us also suppose Alice and Bob agree on a protocol where Alice trivially maps her one qubit onto a flying photon. Alice’s $|e\rangle$ state maps onto a transmitted photon, and Alice’s $|g\rangle$ state maps onto no transmitted photon. Bob decodes this by mapping a received photon onto $|e\rangle$ and no received photon onto $|g\rangle$. Such an encoding will work as long as the channel faithfully transmits the photon. However this encoding will fail if the photon is lost. When the photon is lost under this protocol, then only one outcome is possible for Bob, regardless of what Alice sent.

We can make this protocol robust to such flaws in the channel by redundantly encoding

the transmitted information. Instead, if Alice transmits two photons, mapping $|g\rangle \rightarrow |01\rangle$ and $|e\rangle \rightarrow |10\rangle$, then a photon loss event will result in Bob receiving the state $|00\rangle$, signaling a message corrupted by photon loss. A quantum error correction code requires verification of successful transmission without measuring the encoded data. Measurement of the encoded data inevitably collapses quantum correlations associated with the encoded state. In particular, we require a measurement that is agnostic towards which of the two received modes is excited.

Time-bin remote entanglement [5, 6, 7] encodes one logical flying qubit into two physical flying qubits, namely two well-separated quasi-orthogonal temporal wavepackets on a transmission line [25] as shown in Fig. 1.3. We write the Hilbert space of the combined system $\mathcal{H} = \mathcal{H}_L \otimes \mathcal{H}_E$ where \mathcal{H}_E is the Hilbert space of the early arriving wavepacket mode, and \mathcal{H}_L is the Hilbert space of the late arriving wavepacket mode. Following the previous section, the protected subspace of this system is spanned by $\{|1, 0\rangle, |0, 1\rangle\}$. Chiefly, these two states correspond to a single photon which arrives late in time, and a single photon which arrives early in time.

1.4 Dissertation overview

This dissertation introduces a protocol for photon-loss robust, time-bin remote entanglement in the framework of circuit QED. We implement the protocol in a simple quantum network between two quantum information processing modules, and verify the ability of the protocol to detect photon loss, yielding entangled states mostly limited by local qubit decoherence.

In Chapter 2, we introduce in greater detail the framework of circuit QED and the transmon qubit. We then discuss the theory of parametric drives, which we used both to apply multi-qubit gates within the module, and will be used to construct the multi-module gates used in the time-bin entanglement protocol. We then present a hardware quantum information processing module amenable to the time-bin-entanglement protocol. The coherence times, gate fidelities, mode frequencies, and other crucial parameters of the module are then characterized.

In Chapter 3, we discuss how to use the parametric drives described in chapter 2 to cou-

ple the qubit and storage mode to the transmission line. The chapter begins with treating the qubit-buffer mode system under pumping and dissipation, and explains how the parametric drives implement a Q-switch. We then explain the implementation details of this setup. In particular, the frequency and amplitude compensation required to contend with the intervening AC-Stark shift terms generated by the drives. The chapter concludes with data showing that the AC-Stark shift terms were properly compensated for all four parametric processes necessary for the time-bin entanglement protocol, and that these processes are under our control.

In Chapter 4, we consider these modules in the context of a network. The chapter begins with a brief discussion of various networks used in circuit QED entanglement experiments. We then introduce the theoretical tools used to model the modules connected to the communication channel. We then characterize the communication channel realized in experiment, and then how we perform joint qubit readout with the connectivity we use. We then use the mechanics developed in chapter 3 to implement gates that efficiently convert stationary states into propagating states with controlled temporal modes. With the shape of the temporal mode under control, we additionally show that the reverse process is possible: with known flying temporal mode, it is possible to efficiently convert a photon impinging upon a module into a stationary state inside the module. We then demonstrate parametric processes necessary for our time-bin entanglement protocol may be used to transfer an excitation from one module to the other.

In Chapter 5, we introduce our time-bin entanglement protocol in detail, and describe how we implemented it. We then put the protocol to the test and entangle the storage modes of two quantum information processing modules, and detect photon loss. We then apply joint tomography on the storage modes of the modules, and characterize the fidelity of the generated entanglement with and without error detection.

We conclude by examining some potential ways to improve the fidelity of the entangled states generated by our hardware, as well as some potential future experiments to extend upon the work in this dissertation.

Chapter 2

Quantum Processing Modules

In this chapter, we detail the design and characterization of the individual modules of our elementary quantum network, which will be reduced to only two modules connected by a directional transmission line.

2.1 The transmon qubit/cavity architecture

2.1.1 The Josephson junction in the transmon regime

To create a quantum computer, we require well-behaved, controllable, quantum mechanical degrees of freedom. In contrast to atomic physics, where microscopic degrees of freedom such as spin are the focus, we focus on the macroscopic degrees of freedom of electrical circuits, such as current and voltage. Electrical circuits fit into our overall modular approach, where well-understood building blocks like resistors, capacitors, and inductors, are combined in simple, well understood ways. A key advantage of building our custom, artificial atom from tunable elements, is the freedom to tailor the atom to our own needs. Placing our atom's transition frequency in the microwave band means that all control fields may be generated and manipulated through off-the-shelf microwave hardware. We also have a wealth of knowledge from microwave electrical engineers to lean on for the design of attenuators, filters, and mixers.

We build our circuits from superconducting aluminum. Aluminum, when cooled well below its critical temperature of 1 K, exhibits no dissipation for signal frequencies below

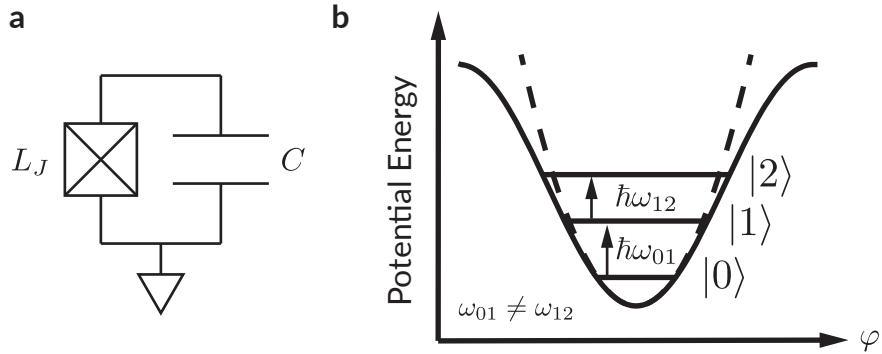


Figure 2.1: The left panel displays a Josephson junction with inductance L_J shunted by a capacitance C , implementing a transmon qubit. The right panel displays the quantized energy spectrum of the transmon qubit (horizontal lines) residing in the cosine potential energy well of the transmon (solid black sinusoid), overlaid with the quadratic potential corresponding to a linearization of the cosine potential (dotted lines). Due to anharmonicity, level spacing between levels $|0\rangle$ and $|1\rangle$ differs from that of $|1\rangle$ and $|2\rangle$

the gap [26]. This makes circuits fabricated from superconducting aluminum especially suitable for the long-term storage of quantum information. To function as a usable qubit our artificial atom must be in an environment where the typical energy $k_B T$ of thermal fluctuations is much less than the energy quantum $\hbar\omega_{01}$ associated with transitions between the ground and first excited state of the artificial atom to avoid spurious thermal excitations [27]. A frequency of $\omega_{01} = 2\pi \cdot 5$ GHz corresponds to a characteristic temperature of 250 mK. Temperatures corresponding to $T \ll T_c$ and $k_B T \ll \hbar\omega_{01}$ are readily obtained by cooling the artificial atom with a commercially available dilution refrigerator.

Our artificial atom requires a source of nonlinearity to realize a system with individually addressable energy levels. The Josephson junction is an ideal candidate, being both nearly dissipationless and implementing a dynamical nonlinear inductance. A Josephson junction consists of two superconductors sandwiching a thin insulating layer [28]. We separate the Josephson junction into a Josephson capacitance C_J , set by the overlap area of the two pads and the oxide thickness, in parallel with a nonlinear dynamical inductance element which we

call the Josephson element. The Josephson element is governed by the following equations

$$V(t) = \frac{\hbar}{2e} \frac{\partial \varphi}{\partial t} \quad (2.1)$$

$$I(t) = I_0 \sin(\varphi), \quad (2.2)$$

where $V(t)$ and $I(t)$ are the voltage and current across the junction, $\varphi(t)$ is the phase difference across the junction, and I_0 is the parameter characterizing the Josephson element [29]. This parameter is readily measured at room temperature through the normal state resistance R_n of the junction, related to I_0 by the Ambegaokar-Baratoff [30] relation

$$I_0 = \frac{\pi \Delta}{2eR_n}. \quad (2.3)$$

Plugging $I(t)$ into $V(t)$, we find that the Josephson element behaves like a nonlinear inductance L_J depending upon φ

$$L_J(\varphi) = \frac{L_{J0}}{\cos(\varphi)}, \quad (2.4)$$

where $L_{J0} = \varphi_0/I_0$, and $\varphi_0 = \hbar/2e$ is the reduced magnetic flux quantum.

The Cooper-pair box is a device that consists of a Josephson junction connected to an external voltage source V_g through a capacitor C_g [31]. We can write the Hamiltonian for this system as:

$$\mathbf{H}/\hbar = 4E_C (\mathbf{n} - n_g)^2 - E_J \cos(\varphi) \quad (2.5)$$

where the number operator \mathbf{n} counts how many Cooper pairs have crossed the Junction. The phase difference across the junction has been promoted to an operator, and now obeys the commutation relation $[\varphi, \mathbf{n}] = i$. We also write the gate charge n_g , referring to the charge on the superconducting island induced by the gate capacitance. $E_C = e^2/2C_\Sigma$ is the charging energy and $E_J = \varphi_0 I_0 = \varphi_0^2/L_{J0}$ is the Josephson energy, and $C_\Sigma = C_J + C_g$ is the combined capacitance of the gate and junction. The ratio E_J/E_C characterizes the nonlinearity of the device and sensitivity to charging. We may also write the plasma frequency $\omega_q = 1/\sqrt{L_J C_J}$ corresponding to the frequency of classical oscillations at the base of the cosine well.

In the regime where $E_J/E_C \approx 1$, this Hamiltonian is sensitive to $1/f$ charge noise fluctuations due to its energy dispersion. By shunting the junction with a capacitance, the system may be moved into the transmon regime [14], characterized by $E_J/E_C \approx 30 - 100$. Here we alter C_Σ with a the additional shunting capacitance $C_\Sigma = C_J + C_g + C_s$ where C_s is the shunting capacitance. In this regime, the wave-function is well-localized in the flux basis and poorly localized in the charge basis. The mean square fluctuation of the flux operator $\Phi = \varphi_0 \varphi$ may be calculated

$$\langle 0 | \Phi^2 | 0 \rangle = \frac{1}{2} \hbar Z_c, \quad (2.6)$$

where $Z_c = \sqrt{\frac{L_J}{C_\Sigma}}$ is the characteristic impedance of the oscillator, which for typical parameters of $L_J = 10$ nH and $C \approx 85$ fF, $Z_c \approx 300 \Omega$ making $\sqrt{\langle 0 | \Phi^2 | 0 \rangle} \approx 0.06 \Phi_0$, meaning the wavefunction is well localized inside the cosine potential. Conversely, the wavefunction is spread out in the charge basis, making the transmon minimally sensitive to charge noise.

In this transmon regime, the offset charge n_g may be removed from the equation by applying a gauge transformation $U = \exp(-in_g \varphi)$ [31]. Furthermore, the flux operator may be written in terms of the lowering operator \mathbf{q} as $\Phi = \Phi_{ZPF} (\mathbf{q} + \mathbf{q}^\dagger)$, where $\Phi_{ZPF} = \sqrt{\hbar Z_c / 2}$. The Hamiltonian may then be rewritten

$$H = \hbar \omega_p \mathbf{q}^\dagger \mathbf{q} - E_J \left(\cos(\varphi) + \frac{\varphi^2}{2} \right), \quad (2.7)$$

splitting the Hamiltonian into the harmonic mode and nonlinear terms.

With previously given typical parameters, the characteristic impedance $Z_c \approx 300 \Omega$ is within a factor of unity of the vacuum impedance $Z_{\text{vac}} \approx 377 \Omega$. This implies that our transmon will be relatively well matched to any pair of leads. This is in stark contrast to atoms, which are very poorly matched to the electromagnetic vacuum. This strong coupling provides for fast gates and fast readout, but requires some additional technical sophistication to tame.

2.1.2 Coupling a transmon to a cavity

A crucial insight in the field of cavity QED was the use of a high-Q cavity to enhance the coupling of atoms to the electromagnetic field. The impedance of an atom [27] may be crudely approximated by the impedance quantum $R_K = h/e^2$. We live in a universe where the ratio $Z_{vac}/2R_K$, also known as the fine structure constant $1/137.0$, is a small number. By placing an atom in a cavity, this coupling may be enhanced by a factor of the cavity's Q . Circuit QED [13], on the other hand, operates in the regime where the artificial atom impedance is relatively compatible with the vacuum impedance. While this means that control and readout fields will interact strongly with the artificial atom, yielding fast gates and readout, it also means that the artificial atom will readily radiate energy.

Crucially, a cavity may also be used to *reduce* the coupling of the artificial atom to the electromagnetic environment. To see how, let us suppose a transmon capacitively coupled to a single mode of a cavity with annihilation operator \mathbf{b} ,

$$H_{JC}/\hbar = \omega_b \mathbf{b}^\dagger \mathbf{b} + \omega_q \mathbf{q}^\dagger \mathbf{q} + g (\mathbf{b} \mathbf{q}^\dagger + \text{h.c.}). \quad (2.8)$$

Here, the annihilation operator \mathbf{q} corresponds to the transmon mode, ω_b corresponds to the cavity mode frequency, and g characterizes the coupling between cavity and transmon modes. Here we take $g \ll \Delta$, where $\Delta = \omega_q - \omega_b$ is the mutual detuning between qubit and cavity. This is known as the dispersive regime, where eigenstates of qubit and cavity are only slightly modified by the coupling. Using Fermi's golden rule, the decay rate of the transmon mode will be given by

$$\Gamma = 2\pi g^2 D(\omega_q). \quad (2.9)$$

The density of states $D(\omega)$ due to the cavity is given by [32]

$$D(\omega) = \frac{1}{\pi} \frac{\kappa/2}{(\omega - \omega_b)^2 + (\kappa/2)^2}. \quad (2.10)$$

Here we have supposed that the cavity mode loses energy to the environment at a rate κ ,

yielding the decay rate due to coupling to the cavity of

$$\Gamma_P \approx \left(\frac{g}{\Delta}\right)^2 \kappa, \quad (2.11)$$

where we have taken $\Delta \gg \kappa$. With appropriate choice of couplings and detunings, radiative losses to the transmission line of interest may be demonstrated to be vanishing relative to other loss mechanisms [10].

Besides protecting our delicate qubit from the environment, putting the qubit in a box confers other features, one of which being a mechanism for reading out the qubit. Applying the so-called dispersive approximation [13], which uses that $g \ll \Delta$, we obtain the following Hamiltonian

$$\mathbf{H}/\hbar = \omega_b \mathbf{b}^\dagger \mathbf{b} + \omega_q \mathbf{q}^\dagger \mathbf{q} - \chi \mathbf{b}^\dagger \mathbf{b} \mathbf{q}^\dagger \mathbf{q} \quad (2.12)$$

with $\chi = \frac{2g^2}{\Delta}$ is defined as the dispersive shift, the qubit state dependent shift of the cavity frequency. We also neglect a small shifting of the cavity mode due to the Lamb shift. We will later introduce techniques for probing the frequency of the cavity so that we may probe the state of the qubit, giving us the ability to read out the state of the qubit on demand.

Now, let us analyze the coupling of the buffer mode to the outside world in more detail. We suppose that this coupling to the environment is due to an attached transmission line with associated input mode \mathbf{t}_{in} associated with electromagnetic waves traveling towards the cavity, and output mode \mathbf{t}_{out} associated with electromagnetic waves traveling away from the cavity, with a coupling to the cavity of κ . Under these conditions, input-output theory [33] yields the following Langevin equation

$$\dot{\mathbf{b}} = \frac{i}{\hbar} [\mathbf{H}, \mathbf{b}] - \frac{\kappa}{2} \mathbf{b} - \sqrt{\kappa} \mathbf{t}_{\text{in}}(t) \quad (2.13)$$

$$= -i \left(\omega_b - \frac{\chi}{2} \boldsymbol{\sigma}_{\mathbf{Z}} - \frac{\kappa}{2} \right) \mathbf{b} - \sqrt{\kappa} \mathbf{t}_{\text{in}}(t). \quad (2.14)$$

If we drive write these equations of motion for a classical driving field $\langle \mathbf{t}_{\text{in}}(t) \rangle = \boldsymbol{\epsilon}(t)$ and

condition upon the qubit state, we find equations for the classical cavity responses $\beta(t)$

$$\dot{\beta}_g = - \left(i \left(\omega_c + \frac{\chi}{2} \right) + \frac{\kappa}{2} \right) \beta_g - \sqrt{\kappa} \epsilon(t) \quad (2.15)$$

$$\dot{\beta}_e = - \left(i \left(\omega_c - \frac{\chi}{2} \right) + \frac{\kappa}{2} \right) \beta_e - \sqrt{\kappa} \epsilon(t). \quad (2.16)$$

Taking a Fourier transform of the above equations, we obtain

$$\beta[\omega] = \frac{\sqrt{\kappa} \epsilon[\omega]}{i \left((\omega - \omega_c) \pm \frac{\chi}{2} \right) - \frac{\kappa}{2}}, \quad (2.17)$$

with $+$ ($-$) associated with $|g\rangle$ ($|e\rangle$).

Importantly, the measurement field will have influence the qubit by proxy of the cavity in the same way that the cavity is influenced by the qubit. We can rewrite Eq. 2.12 in the form

$$\mathbf{H}/\hbar = \omega_b \mathbf{b}^\dagger \mathbf{b} + \left(\omega_w - \chi \mathbf{b}^\dagger \mathbf{b} \right) \frac{\boldsymbol{\sigma}_Z}{2} \quad (2.18)$$

making clear that photon population in the cavity will result in a frequency shift of the qubit. We quote the results of Gambetta et al. [34], which finds that the qubit frequency is shifted by a frequency

$$\Delta_m(t) = \chi \text{Re} [\beta_g(t) \beta_e^*(t)]. \quad (2.19)$$

Additionally, the intracavity field during measurement contains shot noise due to the coupling of the mode to the transmission line. This field noise results in fluctuations of the $\chi \boldsymbol{\sigma}_Z \mathbf{b}^\dagger \mathbf{b}$ term in the Hamiltonian, and thus fluctuations of the qubit frequency, resulting in dephasing. This results in an additional dephasing rate of

$$\Gamma_m(t) = \chi \text{Im} [\beta_g(t) \beta_e^*(t)]. \quad (2.20)$$

This dephasing is a necessary consequence of measurement. Let us imagine an incoming measurement field divided up into equal duration temporal wavepackets. During the process of measurement, we imagine a small amount of qubit information written upon the amplitude and phase of the each temporal wavepacket traveling through the cavity. When amplitude and phase information of each wavepacket is acquired by a measurement apparatus, we then

acquire the qubit information associated with that wavepacket. Measurement of each wavepacket betrays information about the qubit, and therefore has the consequence of projecting the qubit slightly towards one of the poles of the Bloch sphere. Excluding all information acquired through the measurement, the kicks to the qubit result in qubit dephasing at a rate Γ_m . Including all information acquired through the measurement, we understand that Γ_m is the rate at which the measurement chain acquires information about the qubit state. This is why Γ_m is referred to as the measurement rate. For a rigorous explanation of this process, we recommend the reader explore the treatment detailed in Korotkov [35] or one of the various experimental explorations of this process [36, 37].

2.1.3 Storage cavity

While the cavity made an effective shield and readout mechanism, microwave cavities have additional applications in the field of circuit QED. Their ease of fabrication and superb quality factors make them excellent candidates for the long term storage of quantum information [38]. However, as was discussed earlier, a harmonic mode does not possess uniquely addressable energy levels. We may couple a transmon to a high-Q cavity, and use the nonlinearity of the transmon to control a cavity dedicated to the storage of quantum information, or “storage cavity.” The previously described Hamiltonian generalizes to three modes, with the fundamental mode of the storage cavity associated with the annihilation operator \mathbf{s} . Here we take a slightly different route to deriving the Hamiltonian, in which we start from the cosine potential of the Josephson element with additional harmonic buffer and cavity modes, with participation of each mode in the Josephson element characterized by zero point fluctuations φ_b , φ_q , and φ_s .

$$\mathbf{H}/\hbar = \omega_b \mathbf{b}^\dagger \mathbf{b} + \omega_q \mathbf{q}^\dagger \mathbf{q} + \omega_s \mathbf{s}^\dagger \mathbf{s} \quad (2.21)$$

$$- E_J \left(\cos(\varphi) + \frac{\varphi^2}{2} \right) \quad (2.22)$$

$$\varphi = \varphi_b (\mathbf{b} + \mathbf{b}^\dagger) + \varphi_q (\mathbf{q} + \mathbf{q}^\dagger) + \varphi_s (\mathbf{s} + \mathbf{s}^\dagger) \quad (2.23)$$

We may expand this Hamiltonian to fourth order and apply a rotating wave approximation to obtain

$$\mathbf{H}/\hbar = \omega_b \mathbf{b}^\dagger \mathbf{b} + \omega_q \mathbf{q}^\dagger \mathbf{q} + \omega_s \mathbf{s}^\dagger \mathbf{s} \quad (2.24)$$

$$- \sum_{a=b,q,s} \frac{\chi_{aa}}{2} (\mathbf{a}^\dagger \mathbf{a})^2 \quad (2.25)$$

$$- \chi_{bq} \mathbf{b}^\dagger \mathbf{b} \mathbf{q}^\dagger \mathbf{q} - \chi_{bs} \mathbf{b}^\dagger \mathbf{b} \mathbf{s}^\dagger \mathbf{s} - \chi_{qs} \mathbf{q}^\dagger \mathbf{q} \mathbf{s}^\dagger \mathbf{s}, \quad (2.26)$$

with the coefficients $\hbar\chi_{aa} = E_J\varphi_a^4/2$, $\hbar\chi_{bq} = E_J\varphi_b^2\varphi_q^2$, $\hbar\chi_{bs} = E_J\varphi_b^2\varphi_s^2$, and $\hbar\chi_{qs} = E_J\varphi_q^2\varphi_s^2$. This Hamiltonian will constitute the undriven module system examined for the remainder of the dissertation.

In the limit where the qubit line width is much smaller than χ_{qs} , the qubit will split into number resolved peaks corresponding to the storage mode population. By driving the qubit with a calibrated gaussian envelope pulse with $\sigma \ll 1/\chi_{qs}$, the individual lines of the number split qubit may be addressed, such that the qubit is only excited by the pulse when the pulse is resonant with the peak corresponding to the storage population. Such a pulse is referred to as a selective π -pulse, and is the first tool in our arsenal for communicating with the storage mode.

2.2 Theory of parametric drives

The nonlinearity present in a transmon qubit is typically introduced as serving to lift the energy level spacing degeneracy of the linear LC circuit. This nonlinearity may also serve as an effective on-demand frequency converter and squeezer through the use of parametric driving [39]. The idea is to avoid direct coupling between two or more modes, preferring instead to engineer an effective coupling mediated by one or more strong drive tones and the nonlinearity of the junction. In this setup, the amplitudes and phases of the drives directly control the amplitude and phase of the realized interaction terms.

Let us start by simply driving a Harmonic oscillator of frequency ω with a classical drive: an electric field $E(t) = E_0(A(t) + \xi(t))$, following Z. Leghtas (personal communication,

2014). Here, E_0 is a normalization factor which has the dimension of an electric field. A has units of square root of photon number, and constitutes the amplitude of the field that we impose on the oscillator. $\xi(t)$ is a noise term which is a gaussian noise of average 0 and standard deviation 1. This noise, called the shot noise, is intrinsic to any classical electric field and is unavoidable. The resultant Hamiltonian is

$$\mathbf{H}/\hbar = \omega_0 \mathbf{a}^\dagger \mathbf{a} + \mu E(t) (\mathbf{a} + \mathbf{a}^\dagger), \quad (2.27)$$

where μ is a coupling term between the oscillator and the field $E(t)$. We denote $\epsilon(t) = \mu E_0 A(t)$ and $\delta\epsilon(t) = \mu E_0 \xi(t)$. Despite this noise term, we would like the field seen by the oscillator to be as noiseless as possible. To this aim, we go to the limit $\mu \rightarrow 0$ and $A \rightarrow \infty$ such that $\epsilon(t)$ stays constant, and $\delta\epsilon \rightarrow 0$. This brings us to this Hamiltonian:

$$\mathbf{H}/\hbar = \omega_0 \mathbf{a}^\dagger \mathbf{a} + \epsilon(t) (\mathbf{a} + \mathbf{a}^\dagger), \quad (2.28)$$

where $\epsilon(t)$ is a completely deterministic function of time with no noise. In this case where the drive amplitude is much larger than the quantum fluctuations, we treat the drive completely classically. This is known as the stiff-pump approximation, as the drive now acts as a sort of voltage source where the drive transfers energy to the cavity without being depleted.

Now, we consider one transmon qubit coupled to a buffer cavity and storage cavity. Following Campagne-Ibarcq et al. [24] and Nigg et al. [40]. we split the Josephson junction into a linear inductor and a purely nonlinear element. The environment seen by this nonlinear element is a series of coupled linear modes with low dissipation (the plasma excitations of the junction shunted by the antennas and the modes of the cavity.) One can then find a decoupled mode basis (Foster decomposition) of this environment, whose two first resonant modes are labeled q and b correspond to excitations of the transmon and cavity. We neglect higher frequency modes. We consider N drives, which can drive the transmon and the cavity modes ($a = \mathbf{q}, \mathbf{b}, \mathbf{s}$) with strengths ϵ_{aj} , the Hamiltonian of the system reads

$$\mathbf{H}/\hbar = \omega_q \mathbf{q}^\dagger \mathbf{q} + \omega_b \mathbf{b}^\dagger \mathbf{b} + \omega_s \mathbf{s}^\dagger \mathbf{s} - \frac{E_J}{\hbar} \left(\cos(\varphi) + \frac{\varphi^2}{2} \right) + \sum_{\substack{a=q,b,s \\ j=1..N}} 2\text{Re}(\epsilon_{aj} e^{-i\omega_j t}) (\mathbf{a} + \mathbf{a}^\dagger) \quad (2.29)$$

where Re denotes the real part, and the phase across the nonlinear element φ is the sum of the contributions from the transmon and cavity modes (zero point fluctuations $\varphi_q, \varphi_b, \varphi_s$)

$$\varphi = \varphi_q (\mathbf{q} + \mathbf{q}^\dagger) + \varphi_c (\mathbf{b} + \mathbf{b}^\dagger) + \varphi_s (\mathbf{s} + \mathbf{s}^\dagger) \quad (2.30)$$

Then, following Leghtas et al. [19], we move to a $3N$ displaced frame with the unitary

$$\mathbf{U} = \prod_{\substack{a=q,b,s \\ j=1..N}} e^{-\tilde{\xi}_{aj} \mathbf{a}^\dagger + \tilde{\xi}_{aj}^* \mathbf{a}} = e^{i(\theta_q + \theta_c + \theta_s)} e^{\sum_{aj} -\tilde{\xi}_{aj} \mathbf{a}^\dagger + \tilde{\xi}_{aj}^* \mathbf{a}} \quad (2.31)$$

where the phases $\theta_{q,c}$ resulting from the non-commutation of $\tilde{\xi}_{ai,aj} \mathbf{a}^\dagger + \tilde{\xi}_{ai,aj}^* \mathbf{a}$ when $i \neq j$ give a global phase not physically relevant. The displacements are chosen to be $\tilde{\xi}_{aj} = \xi_{aj} e^{-i\omega_j t}$ with $\xi_{aj} = \frac{\epsilon_{aj}}{\frac{\kappa_a}{2} + i(\omega_a - \omega_j)}$. Here, κ_a is the dissipation rate of mode a and can be neglected in the transmon case. Note that each displacement corresponds to the steady state amplitude of the considered mode when subjected to the drive. Finally, we place ourselves in the interaction picture with respect to the Hamiltonian $H = \sum_{a=q,b,s} (\omega_a - \delta_a) \mathbf{a}^\dagger \mathbf{a}$, where δ_a are arbitrary detunings that will be used to cancel the Stark shifts due to the Kerr effect, leading to

$$\tilde{\mathbf{H}}/\hbar = \sum_{a=q,b,s} \delta_m \mathbf{a}^\dagger \mathbf{a} - \frac{E_J}{\hbar} \left(\cos(\tilde{\varphi}) + \frac{\tilde{\varphi}^2}{2} \right) \quad (2.32)$$

$$\tilde{\varphi}' = \sum_{a=q,b,s} \varphi_a \left(\mathbf{a} e^{-i(\omega_a - \delta_a)t} + \mathbf{a}^\dagger e^{i(\omega_a - \delta_a)t} \right) \quad (2.33)$$

$$\tilde{\varphi}'' = \sum_{a=q,b,s} \varphi_a \left(\sum_j (\xi_{aj} e^{-i\omega_j t} + \xi_{aj}^* e^{i\omega_j t}) \right), \quad (2.34)$$

where we have written $\tilde{\varphi} = \tilde{\varphi}' + \tilde{\varphi}''$. Here, $\tilde{\varphi}'$ contains terms corresponding to dynamical degrees of freedom, and $\tilde{\varphi}''$ contains terms corresponding to oscillating currents induced in the junctions, which are completely enslaved to the drive tones with no degrees of freedom. We may rewrite $\tilde{\varphi}''$ in terms of drive frequency components

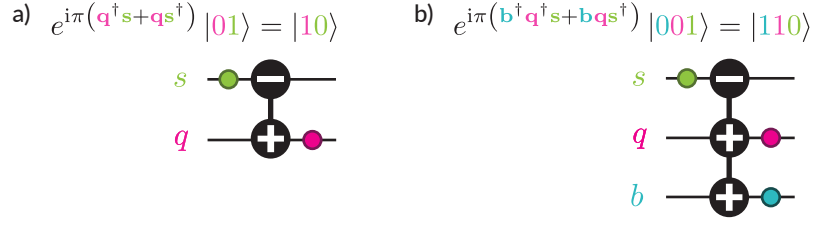


Figure 2.2: **Gates realized by parametric drives** | Here we introduce the symbols we use to refer to gates realized through applying the $\mathbf{q}^\dagger\mathbf{s}+\mathbf{q}\mathbf{s}^\dagger$ process (left panel) and $\mathbf{b}^\dagger\mathbf{q}^\dagger\mathbf{s}+\mathbf{b}\mathbf{q}\mathbf{s}^\dagger$ (right panel) for half a Rabi cycle. Plusses and minuses (white symbol on solid black circle) refer to annihilation and creation operators applied to modes denoted by horizontal lines, labeled by their annihilation operator. Colored circles denote a single photon in the mode, where the symbols denote the coherent removal of this photon and placement in one or more modes by the gate. We remark that this symbol seemingly ignores the conjugate process, but in general, the gate is applied in a context where it plays no role.

$$\tilde{\varphi}'' = \sum_j P_j e^{-i\omega_j t} + P_j^* e^{i\omega_j t} \quad (2.35)$$

$$P_j = \sum_{a=q,b,s} \varphi_a \xi_{aj} = \sum_{a=q,b,s} \frac{\varphi_a \epsilon_{aj}}{\frac{\kappa_a}{2} + i(\omega_a - \omega_j)}. \quad (2.36)$$

where we have substitute in the definition for ξ_{aj} . This makes clear that the current flowing in the junction is filtered by the modes of the system. Let us now specialize this Hamiltonian to particular drives to form useful gates.

2.2.1 Synthesizing a SWAP gate between two internal modes

A particularly useful interaction between electromagnetic modes in quantum information is the beam splitter. Here we synthesize a beamsplitter interaction between between two modes: storage (\mathbf{s}) and (\mathbf{q}) given by the Hamiltonian $g(\mathbf{s}^\dagger\mathbf{q} + \mathbf{q}^\dagger\mathbf{s})$. For this section we neglect the remaining buffer mode (\mathbf{b}), which is expected to stay in vacuum. We synthesize such an interaction with parametric drives by placing drives at $\omega_1 = \omega_s + \Delta - \delta_s$ and another at $\omega_2 = \omega_q + \Delta - \delta_q$. We first remark that if $\Delta \ll |\omega_q - \omega_s|$, these drives will participate predominantly in the modes to which they are closest in frequency. Again, following following Campagne-Ibarcq et al. [24], we define complex drive amplitudes

$$\xi_1' = \xi_{1s} + \frac{\varphi_q}{\varphi_s} \xi_{1q} \quad (2.37)$$

$$\xi_2' = \xi_{1q} + \frac{\varphi_s}{\varphi_q} \xi_{1s}. \quad (2.38)$$

This situation is therefore identical to the simplified case where we consider that each drive addresses only one mode, except that the proportionality factor between the drive strength ϵ_j and the effective displacement ξ_j is a priori unknown and can vary with the drive frequencies. Developing 2.32 to fourth order and considering only terms that may be resonant,

$$\mathbf{H}_2 \approx \mathbf{H}_{\text{Stark}} + \mathbf{H}_{\text{Kerr}} + \mathbf{H}_{\text{BS}} \quad (2.39)$$

$$\mathbf{H}_{\text{Stark}}/\hbar = (\delta_q + \Delta_q) \mathbf{q}^\dagger \mathbf{q} + (\delta_s + \Delta_s) \mathbf{s}^\dagger \mathbf{s} \quad (2.40)$$

$$\mathbf{H}_{\text{Kerr}}/\hbar = -\frac{\chi_{qq}}{2} (\mathbf{q}^\dagger \mathbf{q})^2 - \frac{\chi_{ss}}{2} (\mathbf{s}^\dagger \mathbf{s})^2 - \chi_{qs} \mathbf{q}^\dagger \mathbf{q} \mathbf{s}^\dagger \mathbf{s} \quad (2.41)$$

$$\mathbf{H}_{\text{BS}}/\hbar = g_2' \mathbf{q}^\dagger \mathbf{s} + \text{h.c.} \quad (2.42)$$

$$\Delta_q = -2\chi_{qq} |\xi_2'|^2 - \chi_{qs} |\xi_1'|^2 \quad (2.43)$$

$$\Delta_s = -2\chi_{ss} |\xi_1'|^2 - \chi_{qs} |\xi_2'|^2 \quad (2.44)$$

$$g_2' = -\chi_{qs} \xi_1' (\xi_2')^*, \quad (2.45)$$

with the coefficients $\hbar\chi_{aa} = E_j\varphi_a^4/2$ and $\hbar\chi_{qs} = E_j\varphi_q^2\varphi_s^2$. We have neglected terms of the form $\mathbf{a}^\dagger \mathbf{a}$ arising from the normal ordering of the 4th order term, since they simply shift the bare frequencies ω_a by a fixed amount [20]. We also labeled the qubit and storage mode Stark shifts Δ_q and Δ_s , and choose reference frames $\delta_a = -\Delta_a$ to cancel these shifts. To stay on resonance, we need to adapt the drive frequencies such that

$$\omega_1' = \omega_s + \Delta - 2\chi_{ss} |\xi_1'|^2 - \chi_{qs} |\xi_2'|^2 \quad (2.46)$$

$$\omega_2' = \omega_q + \Delta - 2\chi_{qq} |\xi_2'|^2 - \chi_{qs} |\xi_1'|^2 \quad (2.47)$$

yielding the following Hamiltonian

$$\mathbf{H}/\hbar = (g'_2 \mathbf{q}^\dagger \mathbf{s} + \text{h.c.}) - \frac{\chi_{qq}}{2} (\mathbf{q}^\dagger \mathbf{q})^2 - \frac{\chi_{ss}}{2} (\mathbf{s}^\dagger \mathbf{s})^2 - \chi_{qs} \mathbf{q}^\dagger \mathbf{q} \mathbf{s}^\dagger \mathbf{s}, \quad (2.48)$$

which realizes a **SWAP** between qubit and storage modes of the system. Under the influence of these drives, excitations will **SWAP** between qubit and storage modes at a rate $g'_2 = \chi_{qs} \xi'_1 (\xi'_2)^*$. If we restrict the system to the first two levels, all self-Kerr terms may be absorbed into the bare frequencies of the modes, and cross-Kerr terms vanish when considering states involved in Rabi oscillations between $|q=0, s=1\rangle \leftrightarrow |q=1, s=0\rangle$. By enabling ξ'_1 and ξ'_2 for time $t_g = \pi/|g'_2|$, we realize a **SWAP** gate between qubit and storage modes through the unitary

$$\mathbf{U} = e^{-i\mathbf{H}t_g} = \exp \left[-i\pi (\mathbf{q}^\dagger \mathbf{s} + \text{h.c.}) \right] \quad (2.49)$$

In coming chapters, we will refer to **SWAPs** between these modes using the notation detailed in Fig. 2.2a.

Additionally, we define unprimed $\xi_{1,2}$ displacements and $\omega_{1,2}$ drive frequencies corresponding to driving a **SWAP** between the qubit and buffer mode, implementing the process:

$$g_2 \mathbf{q}^\dagger \mathbf{s} + \text{h.c.} \quad (2.50)$$

2.2.2 Synthesizing a generalized **SWAP** gate between three modes

With one single drive, using the four-wave mixing nature of the Josephson junction, it is possible to synthesize couplings between three chosen modes of our system. We place one drive at the frequency

$$\omega_3 = (\omega_q - \delta_q) + (\omega_b - \delta_b) - (\omega_s - \delta_s). \quad (2.51)$$

As in the previous section, we define one complex drive amplitude

$$\xi_3 = \xi_{3b} + \frac{\varphi_s}{\varphi_b} \xi_{3s} + \frac{\varphi_q}{\varphi_b} \xi_{3q} \quad (2.52)$$

noting that the drive will predominantly live in the buffer mode, as $|\omega_s - \omega_q| \ll |\omega_b - \omega_q|$. Again, developing 2.32 to fourth order and considering only terms that may be resonant,

$$\mathbf{H} \approx \mathbf{H}_{\text{Stark}} + \mathbf{H}_{\text{Kerr}} + \mathbf{H}_{\text{BS}} \quad (2.53)$$

$$\mathbf{H}_{\text{Stark}}/\hbar = \left(\delta_b - 2\chi_{bb}|\xi_3|^2\right) \mathbf{b}^\dagger \mathbf{b} + \left(\delta_q - \chi_{bq}|\xi_3|^2\right) \mathbf{q}^\dagger \mathbf{q} + \left(\delta_s - \chi_{bs}|\xi_3|^2\right) \mathbf{s}^\dagger \mathbf{s} \quad (2.54)$$

$$\mathbf{H}_{\text{Kerr}}/\hbar = \sum_{a=q,s,b} -\frac{\chi_{aa}}{2} \left(\mathbf{a}^\dagger \mathbf{a}\right)^2 - \chi_{bq} \mathbf{b}^\dagger \mathbf{b} \mathbf{q}^\dagger \mathbf{q} - \chi_{bs} \mathbf{b}^\dagger \mathbf{b} \mathbf{s}^\dagger \mathbf{s} - \chi_{qs} \mathbf{q}^\dagger \mathbf{q} \mathbf{s}^\dagger \mathbf{s} \quad (2.55)$$

$$\mathbf{H}_{\text{BS}}/\hbar = g_3 \mathbf{b}^\dagger \mathbf{q}^\dagger \mathbf{s} + \text{h.c.} \quad (2.56)$$

$$g_3 = -\frac{E_J}{\hbar} \xi_3 \phi_b^2 \phi_q \phi_s = -\xi_3 \sqrt{\chi_{bq} \chi_{bs}}, \quad (2.57)$$

with the coefficients $\hbar\chi_{aa} = E_J\varphi_a^4/2$, $\hbar\chi_{bq} = E_J\varphi_b^2\varphi_q^2$, $\hbar\chi_{bs} = E_J\varphi_b^2\varphi_s^2$, and $\hbar\chi_{qs} = E_J\varphi_q^2\varphi_s^2$. We have, as before, neglected terms from $\mathbf{a}^\dagger \mathbf{a}$ due to normal ordering, and choose $\delta_b = 2\chi_{bb}|\xi_3|^2$, $\delta_q = \chi_{bq}|\xi_3|^2 + \chi_{bq}$, and $\delta_s = \chi_{bs}|\xi_3|^2$, chosen to cancel the Stark shift induced by the drives, where the additional term of χ_{bq} in δ_q is added to cancel the cross-Kerr that crops up in states involved in the gate of interest. To stay on resonance, we adapt drive frequencies such that

$$\omega_3 = \omega_q + \omega_b - \omega_s - \chi_{bq} - (2\chi_{bb} + \chi_{bq} - \chi_{bs})|\xi_3|^2 \quad (2.58)$$

yielding the following Hamiltonian

$$\mathbf{H}'_3 = \left(g_3 \mathbf{b}^\dagger \mathbf{q}^\dagger \mathbf{s} + \text{h.c.}\right) \quad (2.59)$$

$$+ \sum_{a=q,s,b} -\frac{\chi_{aa}}{2} \left(\mathbf{a}^\dagger \mathbf{a}\right)^2 - \chi_{bq} \left(1 - \mathbf{b}^\dagger \mathbf{b}\right) \mathbf{q}^\dagger \mathbf{q} - \chi_{bs} \mathbf{b}^\dagger \mathbf{b} \mathbf{s}^\dagger \mathbf{s} - \chi_{qs} \mathbf{q}^\dagger \mathbf{q} \mathbf{s}^\dagger \mathbf{s}. \quad (2.60)$$

Again we restrict ourselves to the first two levels of all modes, and trivially absorb self-Kerr terms into the bare mode frequencies. The choice of $\delta_{b,q,s}$ cancels all cross-Kerr terms for both involved states. This Hamiltonian generates Rabi oscillations between $|b=0, q=0, s=1\rangle \leftrightarrow |b=1, q=1, s=0\rangle$, implementing a **SWAP**-like gate that moves excitations from one mode into two, and vis. versa. The symbol used to refer to this gate is

shown in Fig. 2.2b.

2.2.3 Stationary-to-propagating conversion

A photon present in this buffer mode will leak out at a rate corresponding to its coupling to the transmission line. Combining this with the drives from earlier, excitations can be released into the environment at will. The buffer mode thus serves to buffer interactions with the environment. Additionally, the time-reversed process is also available, where quantum-information-carrying photons impinging upon the buffer mode may be captured to the storage and qubit modes through parametric drives. Therefore, beyond readout and protecting the qubit from the environment, the buffer mode buffers communication of qubit and storage modes with the outside world. At this point, we defer detailed discussion of this process to coming chapters, but remark that parametric drives will be used to form a tunable coupler between qubit and transmission line.

2.3 Our quantum processing module suitable for demonstrating photon-loss robust remote entanglement

With the Hamiltonian of interest written down, we now need to engineer a device which implements it. In this section, we explain the various choices that went into the design of our quantum processing module, starting with the nearly-linear buffer and storage modes. We then explain how we couple a qubit to these modes.

2.3.1 Long-term quantum information storage with a post cavity embedded in a waveguide

A crucial requirement for the storage mode is that it be able to maintain the coherence of quantum information for as long as possible. Superconducting microwave cavities are known to have exceptionally high-quality factors, with Q s in the 10^9 to the 10^{10} range [41]. Superconducting cavities may also be designed to be relatively easy to fabricate. In the field of circuit QED, superconducting cavities are routinely milled out of a single block of

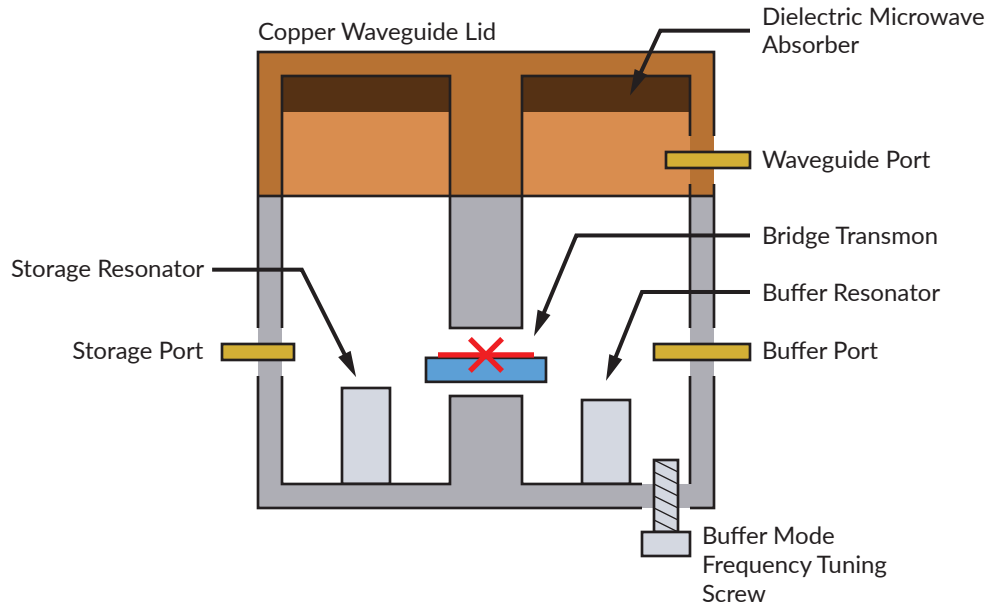


Figure 2.3: **Quantum processing module diagram** | Here we show the schematic diagram of the quantum processing module. The module consists of two linear post cavity modes, named **s** for storage (left), and **b** for buffer (right), and a nonlinear transmon qubit mode **q** (red cross). We couple the qubit mode to the storage and readout modes by using the qubit to bridge both modes. The storage and buffer post cavities are located at the base of waveguide sections with cutoffs set to block radiative loss from all modes. Both subsections feature coupling pins designed to couple to the fundamental mode of the post cavity. The buffer mode subsection features a pin inserted at the opposite end of the waveguide section designed to couple in strong drives, as well as a tuning screw used to make small adjustments to the buffer mode frequency. The module features a microwave absorbing dielectric material in the copper cap of the module designed to cool higher parasitic modes of the system.

aluminum, with integral features for locating coupling pins, mounting screws, and trenches for locating chips, making for easy integration [42].

In practice, surface losses and radiative losses limit the quality factor of superconducting cavities[43]. Any cavity realized through the process of machining will require an entry point for tooling to remove material, resulting in potential pathways for energy to radiate. The 3D post cavity design [38] minimizes radiative losses by localizing cavity fields away from radiative pathways. A section of transmission line of length $\lambda/4$ is formed at the base of a cavity in a piece of superconducting material, as shown in Fig. 2.3. Modeled as an end-shortened post waveguide coupled to a rectangular waveguide, we pick the cross-section of the rectangular waveguide such that the fundamental 3D post cavity mode propagates evanescently in the rectangular section. We additionally choose the length of the rectangular section such that the mode’s energy is well-protected from radiation out the unprotected end of the rectangular waveguide section.

2.3.2 Frequency tuning a 3D post cavity

Our quantum processing modules, by use of previously described parametric processes, communicate quantum information using photons near their buffer mode frequency. It is for this reason that the buffer mode frequencies of both modules must be matched. We achieve frequency tunability through the placement of a superconducting aluminum screw in the base of the cavity (see Fig. 2.3), where the mode’s B field is strongest. Advancing the screw into the cavity then raised the frequency of the mode. Aluminum 3D post cavities have the important property that their normal-state losses are low enough that their resonant frequency may be extracted using a vector network analyzer (VNA) while the cavity is at room temperature and the tuning screw accessible.

To tune the buffer modes of our two systems into resonance, we apply the following procedure: First, the resonant frequency of both Alice buffer mode and Bob buffer mode are measured at room temperature. A screw is inserted into the tuning screw hole of the cavity with the lower frequency to raise its room temperature frequency to the room temperature frequency of the other module’s buffer mode. Next, the modules are cooled to 20 mK, and the frequencies of the buffer modes remeasured, and the detuning noted. Next, the modules

are warmed back up, and the tuning screw adjusted to move the tuned cavity by exactly the detuning, such that the modules are expected to be on resonance once cold. Finally, the buffer modes are recharacterized cold, and this process repeated until the buffer mode frequencies are within a line width of each other.

2.3.3 Reducing the influence of higher cavity modes

The desired Hamiltonian we wish to implement only includes three degrees of freedom, corresponding to the fundamental storage mode, fundamental buffer mode, and the qubit plasma oscillation mode. In practice, we expect many additional modes of our system to contribute to the observed physics. Any mode a with dispersive coupling χ_{aq} to the qubit will shift the qubit's frequency when populated. If the mode is populated by thermal photons with mean photon number $\bar{n}_{\text{th},a}$, the mode population will be noisy, and thus contribute a dephasing rate proportional to $\bar{n}_{\text{th},a}$

$$\Gamma_{\phi}^{\text{th},a} = \frac{\bar{n}_{\text{th},a} \kappa_a \chi_{aq}^2}{\kappa_a^2 + \chi_{aq}^2}, \quad (2.61)$$

where κ_a is the line width of the mode, and $\bar{n}_{\text{th},a} \ll 1$. In a survey by [44] the author reports a range of \bar{n}_{th} populations in circuit QED systems as high as 0.15, corresponding to an effective mode temperature of 140 mK, substantially higher than the dilution refrigerator base temperature, supposed to be caused by poorly thermalized microwave components coupled to these modes. In this work, the author additionally proposes and characterizes a cold microwave attenuator for shielding the qubit-cavity system from the warm environment, and a substantially improved upper bound on residual photon population of 2×10^{-4} , confirming the hot electromagnetic environment.

Here, we take the more conservative goal of trying to cool all modes besides the fundamental storage mode, fundamental buffer cavity mode, and the qubit plasma oscillation mode. We design our module such that these three modes occur at frequencies *below* the waveguide cutoff frequency, and such that all higher modes occur *above* the waveguide cutoff frequency, coupling the higher stationary modes to traveling waveguide modes. This has the result of increasing κ in the above expression for the higher modes, reducing $\Gamma_{\phi}^{\text{th}}$. We remark

that that due to the choice of cutoff frequency, the qubit is forbidden from radiating through the waveguide, and thus will not Purcell limit the qubit. Finally, we suppose that the traveling waveguide modes to which we couple are well thermalized to the dilution refrigerator. This is done through the use of a microwave cold load made out of a dielectric microwave absorber, pictured in Fig. 2.3. This microwave absorber is made out of a 1:1 mix by volume of Apiezon W wax and copper powder, with the wax chosen for minimal heat release, and the copper powder suspension chosen to maximize skin losses. The absorbing material is cured in the copper lid of the module, which is thermalized with copper thermalization straps to the mixing chamber of the dilution refrigerator.

2.3.4 Bridge-transmon architecture

With the implementation of our buffer and storage modes worked out, we now focus on the qubit mode. The Junction of our transmon qubits is a superconductor-insulator-superconductor junction made of Al/AlO_x/Al fabricated by the deposition of two layers of thin-film Al with an intermediate oxidation step to create the insulating barrier. We fabricate our transmons using the bridge-free electron-beam lithography technique [45] on double-side-polished chips of *c*-plane sapphire. The junctions are connected via leads to two circular pads that act as the shunting capacitance of the transmon as well as the coupling capacitance to each cavity.

For ease of coupling, we place two 3D post cavity systems back to back, separated by a thin 1 mm wall, as in Fig. 2.3. We then machine a tunnel through this wall and sides of the module, allowing the insertion of the sapphire chip such that each antenna pad may capacitively couple to the fundamental mode of each cavity, and each side of the chip protrudes slightly from either side of the module. This design additionally has the advantage that the chip may be clamped on both sides of the module, controlling any vibrational modes of the chip itself. The transmon qubit and cavity parameters as well as their couplings are designed using finite-element simulations and black-box quantization [40].

2.3.5 Driving a transmon at the base of a waveguide

The pads of the transmon couple not only to modes of the 3D post cavity, but to all modes of the enclosing waveguide section as well, which has advantages for parametric driving.

From the previous sections, we understand that the strength of the parametric process of interest will be set by how much power, at the drive frequency, can be introduced to the modes of the system. In the harmonic approximation of a single mode of the system, the internal field of a mode at frequency ω_a and coupling to a transmission line κ is given by input output theory with a drive $\epsilon[\omega]$

$$\xi[\omega] = \frac{\sqrt{\kappa}\epsilon[\omega]}{i(\omega - \omega_a) - \frac{\kappa}{2}}. \quad (2.62)$$

We may increase circulating drive power by increasing the coupling of the mode to the environment κ , moving the drive tone ϵ closer to resonance, or simply by increasing ϵ . Each of these has serious drawbacks. Increasing κ will increase exposure of the qubit to the environment, reducing qubit coherence time through the Purcell effect as in Eq. 2.11. Moving the drive tones may not be an option whatsoever, where the drive tones are fixed absolutely as in Eq. 2.58. In Eq. 2.46, the drives may be moved by changing Δ , but too small a Δ risks excitation of the qubit mode. Finally, simply increasing ϵ by turning up the output power on our microwave generator may induce more of a heat load on the dilution refrigerator than is reasonable.

The environment that our qubit sees however is not just that of the storage and buffer modes, but additionally the continuum of cold waveguide modes due to the cold load. Qubit excitations are forbidden from propagating in the waveguide due to choice of cutoff frequency. A drive with frequency above the waveguide, however, will propagate. By ensuring all waveguide modes have $\kappa \gg g$, drive stiffness is additionally ensured. Said another way, we expect that the cold attenuator will dissipate much more power than is ever used by the driven process, and thus again, the drive is well approximated by classical drive in the Hamiltonian.

To introduce drives to the waveguide modes, we insert a coupling pin in the lid of the module. We avoid heating the waveguide modes with the hot electromagnetic environment of the dilution refrigerator input lines by ensuring that the coupling of the waveguide modes to the pin is small relative to the loss introduced by the absorber. We therefore expect the waveguide modes to thermalize to the absorber, and not the dilution refrigerator input lines.

	Alice	Bob
$\omega_b/2\pi$	7908.99 MHz	7909.17 MHz
$\omega_q/2\pi$	5984.17 MHz	5789.10 MHz
$\omega_s/2\pi$	5346.64 MHz	5030.51 MHz
$\kappa_b/2\pi$	252 kHz	248 kHz
$\chi_{qq}/2\pi$	157 MHz	174 MHz
$\chi_{qs}/2\pi$	4.88 MHz	2.11 MHz
$\chi_{bq}/2\pi$	834 kHz	686 kHz
T_1	70 μ s	71 μ s
T_{2R}	5.7 μ s	33 μ s
T_{2E}	43 μ s	54 μ s
$T_{1,Cav}$	226 μ s	520 μ s

Table 2.1: **Alice and Bob Intrinsic Parameters** | This table lists the resonant frequencies, dispersive shifts, and decay times for the various modes of the Alice and Bob quantum processing modules.

2.4 Experimental characterization of our quantum processing modules

We now proceed to characterize each module in isolation, showing the results of the characterization in Table 2.1. First, a first approximation of the cavity resonance frequency was determined by transmission VNA measurement. The qubit $g \leftrightarrow e$ transition frequency ω_q was then determined by two-tone spectroscopy. Next, in an amplitude Rabi experiment, we sweep the amplitude of a gaussian-shaped pulse ($\sigma = 8$ ns) to extract amplitudes corresponding to calibrated π and $\pi/2$ rotations, which we refer to as π and $\pi/2$ pulses. In contexts where the axis of rotation is significant, we refer to rotations around the x (y) axis of the Bloch sphere for an angle θ as $R_X(\theta)$ ($R_Y(\theta)$). In the upper three panels of Fig. 2.4, we show traces from standard decay (T_1) and Ramsey coherence measurements (with and without echo, corresponding to T_{2E} and T_{2R}) [46] for characterizing the coherence times of the qubit modes. The extreme disparity between Alice’s T_{2R} and T_{2E} times is not currently understood. We determine χ_{qq} by searching for the qubit transition coupling $|0\rangle$ and $|2\rangle$ levels, occurring at $\omega_q - \chi_{qq}/2$ [46], by spectroscopy.

Buffer mode frequencies and couplings are determined first using VNA measurement in transmission and fitting of the Lorentzian line-shape. Due to the cascade of Alice and Bob systems, separating the lines of the two systems in the presence of reflections in the lines

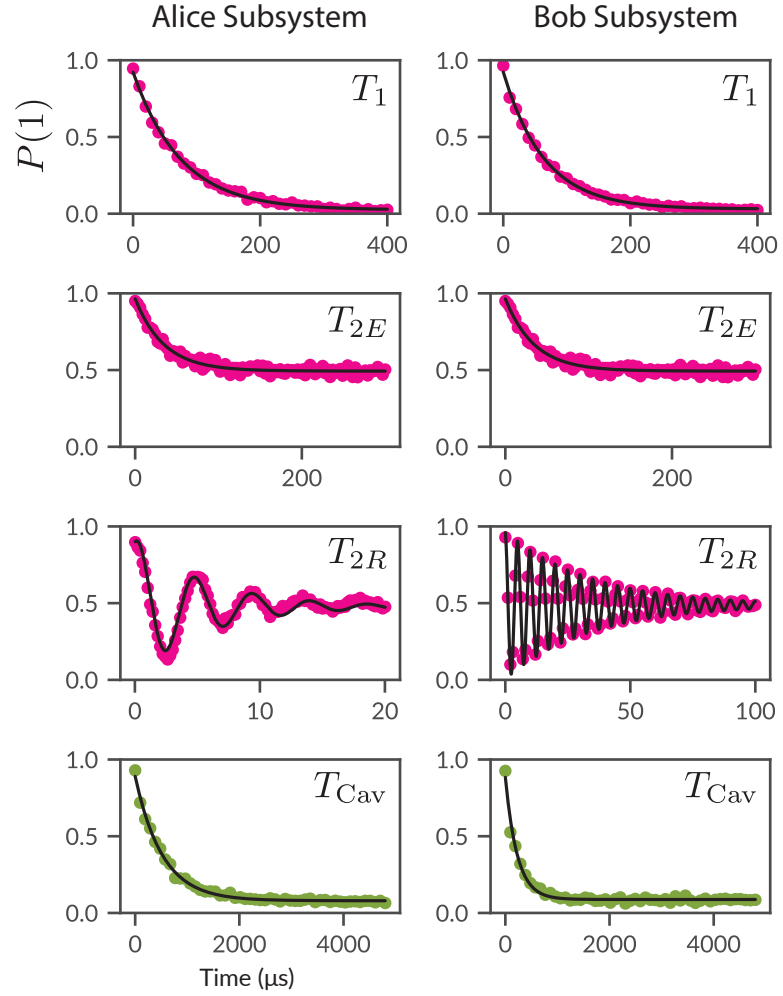


Figure 2.4: **Coherence and decay measurements of Alice and Bob modes** | Alice (left column) and Bob (right column) qubits subjected to Decay (T_1), and Ramsey measurements, with echo (T_{2E}) and without (T_{2R}) experiments (top 3 rows.) for characterization of their decay and coherence times. In the bottom row, the Alice and Bob storage modes were prepared in the $|1\rangle$ state and then after a variable delay, their population measured using a selective π pulse followed by qubit readout, extracting the cavity decay time.

becomes difficult. A more precise characterization of the buffer mode frequencies, couplings, and dispersive shifts is done using a dressed Ramsey interference experiment, explained in detail in Section 4.3.1.

The storage mode frequency for each system is determined using the dispersive coupling between qubit and storage mode. Two tones, one at the qubit frequency, and one swept near the storage mode, are driven for a time long relative to $1/\chi_{qs}$, where χ_{qs} here is assumed from simulation. When the storage drive tone is resonant, the storage mode will be displaced, Stark shifting the qubit away from resonance, preventing it from being excited by the qubit drive tone.

We extract the qubit-storage dispersive shift χ_{qs} through a variable amplitude pulse applied to the storage mode on resonance, followed by spectroscopy of the qubit. The variable amplitude pulse generates a coherent state in the storage mode, resulting in photon-number resolved peaks at $\omega_q - \chi_{qs}n$ for Fock state $|n\rangle$, corresponding to the dispersively shifted qubit. The spacing of these peaks then corresponds to χ_{qs} [47].

We next characterize the storage mode $T_{1,\text{Cav}}$. We begin measuring $T_{1,\text{Cav}}$ by the preparation of the Fock state $|1\rangle$ (discussed in the next section) in the storage mode. After waiting for a variable decay time t , the $|1\rangle$ state probability is mapped onto the qubit through a photon-number selective π pulse followed by qubit readout. The exponential decay of population corresponds to the storage mode $T_{1,\text{Cav}}$.

2.4.1 Coupling between internal degrees of freedom

In this section, we discuss the calibration of a **SWAP** gate between the qubit and storage modes of each module. First, as shown in Fig. 2.5, two blue detuned tones are applied to the qubit and storage modes of a compute module, first prepared with the qubit in the excited state, and the coherent oscillation of population between modes is observed. To tune the process on resonance, the qubit tone is swept until qubit population is minimal after half a cycle. As the transfer pulse is of constant amplitude, the Stark shift correction is incorporated into this frequency calibration. A sinusoid is fit to the curves in the right pane of 2.5 to extract the time needed to **SWAP** one full excitation between qubit and storage, namely 600 ns for Alice, and 500 ns for Bob.

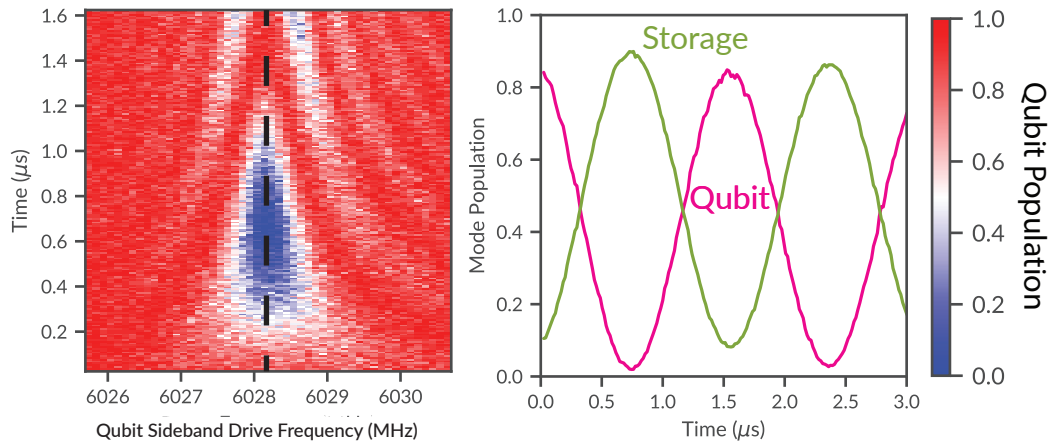


Figure 2.5: **Rabi oscillations between qubit and storage modes of Alice system** | We show the coherent oscillation of energy between the qubit and storage mode under the application of two tones, blue detuned from the qubit and storage by 20 MHz. The left pane shows the characteristic chevron pattern from detuned Rabi oscillations. The vertical black dotted line highlights the frequency at which the drives are resonant, and correspondingly where the drives are applied to generate full **SWAPs** between qubit and storage modes. The left pane shows the coherent exchange of population between qubit and storage modes. Note that no correction has been applied to correct for readout contrast, and thus the amplitude of oscillation and vertical offset is not representative of the actual mode population. Bob subsystem displays qualitatively similar chevron pattern and Rabi oscillations.

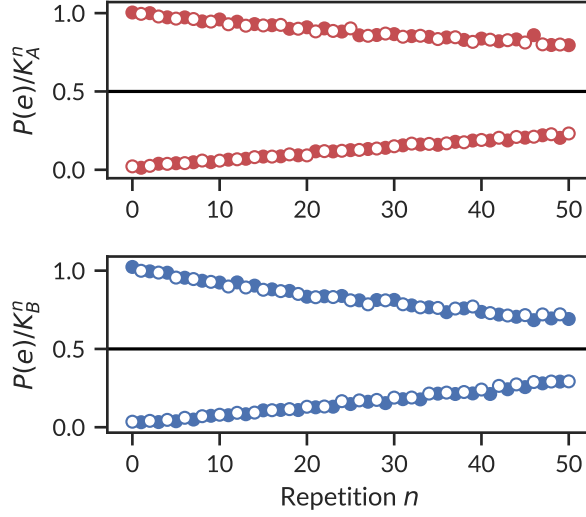


Figure 2.6: **Characterization of SWAP gate Between qubit and storage modes** | We show the results of the repeated application of our calibrated qubit-storage **SWAP** gate on Alice and Bob. The qubit is first prepared in the excited state, n **SWAP** gates are applied, and then the population of the qubit mode and storage mode are read out. Here we plot the readout contrast corrected population of the qubit (solid circle) and storage mode (hollow circle) after division by the expected loss of coherence per round due to decay of both the qubit and storage modes for each module, $K^n = \exp\left(-\frac{1}{2}t_{\text{gate}}\left(T_{1,\text{cav}}^{-1} + T_1^{-1}\right)^{-1}\right)^n$, with K_A^n (K_B^n) having coherence times corresponding to the Alice (Bob) module.

To characterize the error of the gate, the qubit is prepared in the excited state, and then the **SWAP** gate repeatedly applied. The loss of population is well explained by intrinsic decay time scales of each mode, as shown in Fig. 2.6.

Chapter 3

Opening the Module to the Network: Q-Switching

In the previous chapter, we have laid the groundwork for a quantum processing module that can store, manipulate, and recall quantum information in isolation. To be useful in a large-scale quantum computer, it needs to export and import quantum information to facilitate entanglement over a network. Namely, we need a set of quantum-coherent gates which operate between stationary qubits and flying qubits, where these flying qubits shuttle information in and out of our quantum processing modules, establishing entanglement over our quantum network.

One could imagine as many gates to do this as there are potential encodings of flying qubits. In our experiment, we choose to encode our flying qubits in Fock states. The photon-loss robust protocol we develop in this dissertation gains its robustness from how an imperfect, lossy communication channel acts upon such Fock states. In this chapter, we develop gates that exchange quantum information between stationary degrees of freedom and flying Fock states. We will show in the later in the next chapter, how to assemble them into a robust entanglement protocol.

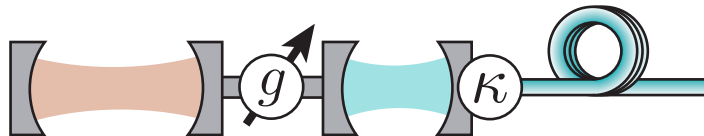


Figure 3.1: **Tunable coupling** | Here we show two modes, a high-Q mode (orange), and a low-Q mode (blue), where the Q is set by the coupling κ to a transmission line, also in blue. We also have a variable linear coupling g between orange and blue modes, which provides an effective tunable coupling with the transmission line, by proxy of the blue mode.

3.1 Tunable Q-switch: Theory

3.1.1 High-level overview of Q-switching

The term Q-switch is appropriated from laser physics, where the quality factor of a laser cavity may be manipulated in time to produce a pulsed output beam. Here, we suppose two different modes at two different frequencies, with two different quality factors. We couple these modes through the process of amplitude tunable frequency conversion Ch. 2.2. A photon converted from the high-Q mode to the low-Q mode may be lost to dissipation in the low-Q mode, making for an effective tunable dissipation in the high-Q mode. We may then dump energy from the high-Q mode into the environment at will. Such a Q-switch has an excellent on-off ratio, as the frequency conversion process is forbidden by energy conservation when the necessary drives are disabled.

Crucially, we require that the dissipation of the low-Q mode is well-controlled, such that the photon is not merely lost, but shuttled from a well-controlled mode to a well-controlled transmission line, making up our quantum channel as in Fig. 3.1. In this setup, the Q-switch serves not only for sending quantum information, but also for receiving. Suppose that a flying photon in this transmission line impinges upon the module and then occupies the low-Q mode. By appropriately activating a frequency conversion process in time with the impinging photon, this photon is converted and shuttled into the high-Q mode. This Q-switching mechanism therefore provides bidirectional single-photon communication with a transmission line. Absorbing a photon efficiently requires knowledge of the shape of the incoming wavepacket to tailor the conversion amplitude. We will leave details of this process to Ch. 4. In this configuration, the low-Q mode buffers communication with the transmission

line, and thus we refer to it as the buffer mode.

Let us now explore the process of Q-switching in detail. We suppose a high-Q, dissipationless qubit mode with annihilation operator \mathbf{q} and low-Q mode buffer mode with annihilation operator \mathbf{b} with coupling to a transmission line κ . We consider the following Hamiltonian modeling tunable frequency conversion with real amplitude $g_2(t)$, written in the doubly-rotating frame of the qubit mode and buffer mode.

$$\mathbf{H}/\hbar = g_2(t) \left(\mathbf{q}^\dagger \mathbf{b} + \mathbf{b}^\dagger \mathbf{q} \right). \quad (3.1)$$

Writing the classical equations of motion, we obtain

$$\dot{q}(t) = -g_2(t) b(t) \quad (3.2)$$

$$\dot{b}(t) = g_2(t) q(t) - \frac{\kappa}{2} b(t). \quad (3.3)$$

This system has two timescales, and thus two interesting regimes where $\kappa \gg g_2(t)$ and one where $\kappa \ll g_2(t)$. When $\kappa \gg g_2(t)$, the buffer mode stays approximately in vacuum and thus steady stated ($\dot{b}(t) \approx 0$), and we can write

$$\dot{q}(t) = -\frac{2g_2^2(t)}{\kappa} q(t).$$

Here, the buffermode has been effectively eliminated as a degree of freedom and we see an effective tunable coupling to our transmission line of $2g_2^2(t)/\kappa$. The alternative regime, where $\kappa \ll g_2(t)$ admits a solution of Rabi oscillations between qubit and buffer mode, as demonstrated in Ch. 2.4.1. We may also fix g_2 constant and solve these coupled equations exactly to obtain

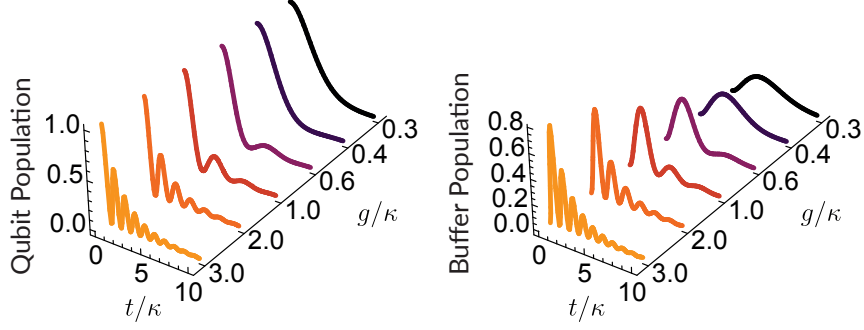


Figure 3.2: **Driving $\mathbf{q}^\dagger\mathbf{b} + \text{h.c.}$ with dissipation on \mathbf{b}** | We suppose two bosonic modes, named qubit (\mathbf{q}) and buffer (\mathbf{b}), under the influence of the Hamiltonian $g(\mathbf{q}^\dagger\mathbf{b} + \text{h.c.})$ with dissipation on the buffer mode at rate κ . We initialize the system with the qubit mode in $|1\rangle$ and the buffer mode in $|0\rangle$, and plot the mode populations as a function of time. In the limit $g \ll \kappa$, the photon in the qubit mode decays out the transmission line at the approximate rate $2g^2/\kappa$. In the limit of $g \gg \kappa$, population sloshes between qubit and buffer while a fraction of population is lost to the transmission line each cycle.

$$q(t) = q(0) e^{-\frac{\kappa}{4}t} \left(\cosh\left(\frac{\gamma t}{4}\right) + \frac{\kappa}{\gamma} \sinh\left(\frac{\gamma t}{4}\right) \right) \quad (3.4)$$

$$b(t) = \frac{4q(0)}{\gamma} g_2 e^{-\frac{\kappa}{4}t} \sinh\left(\frac{\gamma t}{4}\right), \quad (3.5)$$

where we have taken $b(0) = 0$, and defined $\gamma = \sqrt{\kappa - 16g_2^2}$. In the lab, we measure the mode populations, available as $|q(t)|^2$ and $|b(t)|^2$. Plotting these two equations as a function of time with $q(0) = 1$ in Fig. 3.2, we see population sloshing between q and b , resulting in decaying Rabi oscillations, when $g_2 > \kappa_{\text{Out}}/4$, and the smooth, exponential decay of population from the q mode through the b mode into the transmission line when $g_2 < \kappa/4$. Crucially, these equations are a function of the well characterized coupling between b mode and transmission line, κ , and the well controlled initial populations of the modes, leaving the only free parameter the conversion strength g_2 . We will later use these equations to characterize the relationship between our drive power and the strength of the conversion process.

We may also consider processes other than conversion for coupling the relevant modes. Let us consider the following process, which will be a crucial ingredient for our time-binning

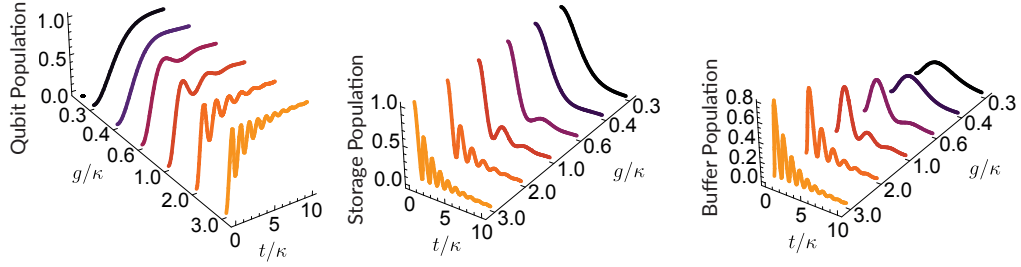


Figure 3.3: **Driving $\mathbf{b}^\dagger \mathbf{q}^\dagger \mathbf{s} + \text{h.c.}$ with dissipation on \mathbf{b}** | Here we suppose three bosonic modes qubit (\mathbf{q}) and buffer (\mathbf{b}), and storage (\mathbf{s}), under the influence of the Hamiltonian $g_3 (\mathbf{b}^\dagger \mathbf{q}^\dagger \mathbf{s} + \text{h.c.})$ with dissipation on the buffer mode at rate κ . We initialize the system with the storage mode in $|1\rangle$ with the remaining modes in vacuum, and plot the mode populations as a function of time. Dynamics of storage population are identical to qubit population in Fig. 3.2, and buffer mode dynamics are identical in both figures. Crucially, the Hamiltonian and dissipation moves the photon in the storage into both the qubit and transmission line.

protocol:

$$\mathbf{H}/\hbar = g_3(t) (\mathbf{b}^\dagger \mathbf{q}^\dagger \mathbf{s} + \mathbf{s}^\dagger \mathbf{b} \mathbf{q}). \quad (3.6)$$

Restricting ourselves to the first two levels of each mode of the system, we see that this Hamiltonian will drive Rabi oscillations between $|001\rangle \leftrightarrow |110\rangle$ written with the mode indices bqs . Introducing a dissipation on the buffer mode will send the $|110\rangle \rightarrow |010\rangle$. Under the action of the dissipation, we may think of the $\mathbf{s}^\dagger \mathbf{b} \mathbf{q}$ process as suppressed, and understand that this system will drive population from the storage mode into both the qubit mode and transmission line. Following Haroche and Raimond [12], we treat this as an effective three-level system spanned by the Hilbert space of $|1\rangle = |001\rangle$, $|2\rangle = |110\rangle$, and $|3\rangle = |010\rangle$ where we can write the master equation

$$\dot{\rho} = -ig_3(t) [|1\rangle \langle 2| + |2\rangle \langle 1|, \rho] + \kappa D[|3\rangle \langle 2|] \rho.$$

We can write this out in terms of components of ρ

$$\dot{\rho}_{11} = -ig_3(t)(\rho_{21} - \rho_{12}) \quad (3.7)$$

$$\dot{\rho}_{21} - \dot{\rho}_{12} = 2ig_3(t)(\rho_{22} - \rho_{11}) - \frac{\kappa}{2}(\rho_{21} - \rho_{12}) \quad (3.8)$$

$$\dot{\rho}_{22} = ig_3(t)(\rho_{21} - \rho_{12}) - \kappa\rho_{22} \quad (3.9)$$

$$\dot{\rho}_{33} = \kappa\rho_{22}. \quad (3.10)$$

We can write this system in terms of three variables $x = \rho_{11}$, $y = \rho_{22}$, $z = \rho_{21} - \rho_{12}$, as the remaining variable ρ_{33} is constrained by $\text{Tr } \rho = 1$, resulting in the following system of equations

$$\begin{pmatrix} \dot{x} \\ \dot{y} \\ \dot{z} \end{pmatrix} = \begin{pmatrix} 0 & 0 & -ig_3 \\ 0 & -\kappa & ig_3 \\ -2ig_3 & 2ig_3 & -\kappa/2 \end{pmatrix} \begin{pmatrix} x \\ y \\ z \end{pmatrix}. \quad (3.11)$$

Exponentiating this system with an initial condition of $P_q(|1\rangle) = 1$, we obtain the mode populations versus time

$$P_q(|1\rangle) = 1 - P_s(|e\rangle) \quad (3.12)$$

$$P_s(|1\rangle) = \frac{e^{-\kappa t/2}}{\gamma^2} \left[(\kappa^2 - 8g_3^2) \cosh\left(\frac{\gamma t}{2}\right) + \kappa\gamma \sinh\left(\frac{\gamma t}{2}\right) - 8g_3^2 \right] \quad (3.13)$$

$$P_b(|1\rangle) = \frac{16}{\gamma^2} e^{\kappa t/2} g_3^2 \sinh^2\left(\frac{\gamma t}{4}\right), \quad (3.14)$$

and plot in Figure 3.3.

We remark that that $P_s(|1\rangle)$ in Eq. 3.13 is equal to $|q(t)|^2$ in 3.4. This is expected, as 3.1 moves excitations from q into the transmission line in the same way that 3.6 moves excitations from s into the transmission line. Crucially, 3.6 coherently moves excitations from s into *both* the q mode *and* the transmission line. This means that we will observe the qubit undergoing decaying oscillations of the qubit from the $|0\rangle$ state to the $|1\rangle$ state, as plotted in Fig. 3.3.

Interestingly, the classical equations of motion and the master equation reproduce the same dynamics. This may be shown by writing the classical equations of motion in terms of the variables $|q|^2$, $|b|^2$, and q^*b , and then identifying $x = |q|^2$, $y = |b|^2$, and $z = 2iq^*b$. We also note that a master equation analysis is also applicable to the $\mathbf{q}^\dagger\mathbf{b} + \text{h.c.}$ process where we choose the states $|1\rangle = |10\rangle$, $|2\rangle = |01\rangle$, and $|3\rangle = |00\rangle$. The classical equations of motion are therefore sufficient for analyzing both the $\mathbf{q}^\dagger\mathbf{b} + \text{h.c.}$ and $\mathbf{b}^\dagger\mathbf{q}^\dagger\mathbf{s} + \text{h.c.}$ process.

Currently, a controllable Hamiltonian containing only the terms in 3.1 or 3.6 is beyond our reach. Intervening Stark shift terms require frequency compensation, where frequency compensation necessitates additional amplitude compensation. In the next section, we introduce the relevant infrastructure for controlling the previously described processes.

3.2 Implementing Q-switching in our quantum processing module

While in Ch. 2 we realized gates between internal quantum processing module modes using parametric processes, and compensated appropriately for induced Stark shifts, the dynamical behavior of the modes under control was of no interest. The goal was to move the population between modes as quickly and as coherently as possible. The controlled release and capture of microwave photons, on the other hand, does require complete control over the time-resolved process strength $g(t)$, as this sets the temporal mode shape of the flying wavepacket. Additionally, capturing a flying wavepacket requires both knowledge of the temporal mode profile of the wavepacket, as well as similarly modulated $g(t)$ for the receiving side. This means that we aim not to quickly switch to a certain maximal $g(t)$, but to smoothly change $g(t)$ in accordance with a calculated optimal profile. This time-resolved control over $g(t)$ raises a number of technical complications, whose solutions we detailed in this section. In particular, this section details the complications involved in referring $g(t)$ back to a complex voltage $\tilde{V}(t) = V_I(t) + iV_Q(t)$, where $V_I(t)$ ($V_Q(t)$) is the voltage output by the DAC controlling the In-Phase (Quadrature) component of the drive displacement. We assume $\tilde{V}(t)$ to correspond to an idealized DAC with flat frequency response, and any actual linear transfer function associated with a practical DAC may simply be folded into

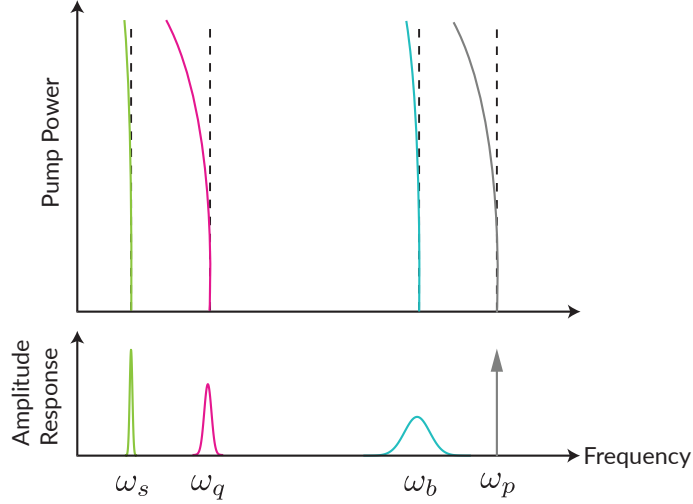


Figure 3.4: **Stark shifting of modes: diagram** | We demonstrate the effect of a variable amplitude drive on the frequency matching condition of a transition of interest. In the lower panel, we show the frequencies of the various modes present in our system (ω_s , ω_q , and ω_b), as well as the bare frequency of a transition of interest ω_p . In the upper panel, we show that the drive will induce an Stark shift on all modes in the system. Due to the shifting frequency of the modes (green line, magenta line, blue line), the frequency matching condition for the drive (grey line) will change as well.

any transfer functions mentioned in the text.

3.2.1 Stark shift compensation

While applied parametric drives develop useful terms in the Hamiltonian, they bring terms along with them that pose some inconveniences. The cosine nonlinearity of the Josephson element, treated in 2.1.1 will generate all combinations of even order interactions between all oscillators coupled to the element. Terms of the form $\chi |\xi|^2 \mathbf{a}^\dagger \mathbf{a}$, for some mode associated with operator \mathbf{a} , and effective drive displacement ξ induce a Stark shift on this mode $\chi |\xi|^2$. When driving a parametric process, the drive must be applied on resonance such that energy is conserved. If the modes involved in the process move in frequency, the drive frequency must also move appropriately. In particular, we restate from sections 2.2.1 and 2.2.2 the resonance conditions for the $\mathbf{b}^\dagger \mathbf{q} + \text{h.c.}$ interaction, realized by two drives at ω_1 and ω_2

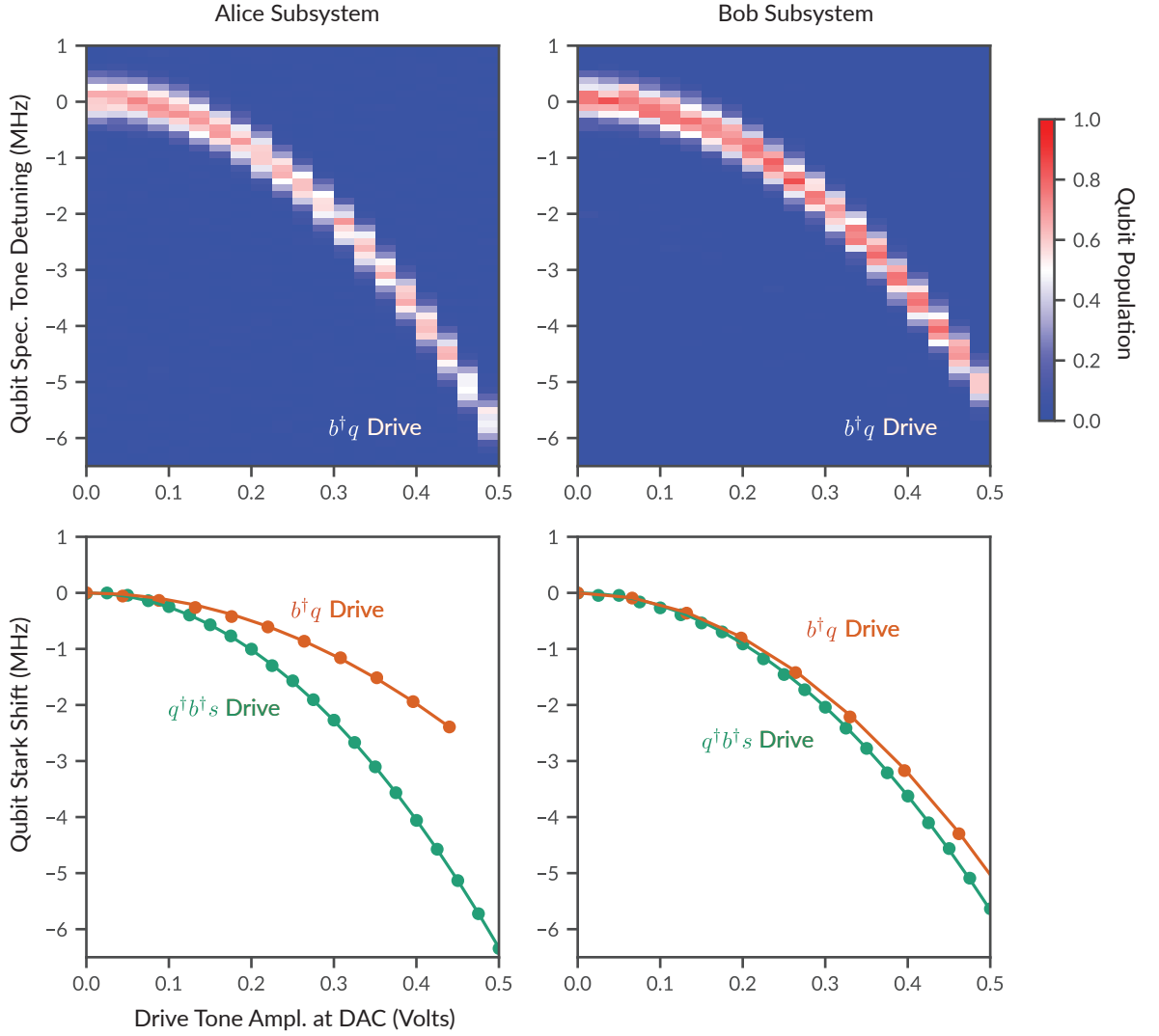


Figure 3.5: **Stark shift compensation: Experimental data** | In the upper panel, we apply on Alice or Bob a $10 \mu\text{s}$ long drive of variable amplitude, at the buffer sideband frequency used to activate the $\mathbf{b}^\dagger\mathbf{q} + \text{h.c.}$ interaction. Simultaneously, we probe the qubit with a microwave tone near its resonance frequency. The quadratic shifting of the frequency with increasing drive amplitude corresponds to the Stark shift. We extract the qubit frequency position and plot in the lower panel as a function of drive amplitude, with an overlaid quadratic fit, all in orange. Added to the lower panel is the result of applying the same protocol and fitting procedure instead with one drive used for the $\mathbf{q}^\dagger\mathbf{b}^\dagger\mathbf{s} + \text{h.c.}$ process, with data and fit plotted in green. Fit coefficients were later used to compensate the Stark shift when chirping control pulses to stay on resonance.

$$\omega_1 = \omega_b + \Delta' + \chi_{bq} |\xi_1|^2 - 2\chi_{qq} |\xi_2|^2 \quad (3.15)$$

$$\omega_2 = \omega_q + \Delta' \quad (3.16)$$

where we have absorbed all Stark shift terms intervening in ω_2 into $\Delta = \Delta' + 2\chi_{qq} |\xi_2|^2 + \chi_{qb} |\xi_1|^2$, and the $\mathbf{q}^\dagger \mathbf{b}^\dagger \mathbf{s} + \text{h.c.}$ interaction, realized by a single drive at ω_3

$$\omega_3 = \omega_q + \omega_b - \omega_s - \chi_{bq} - \chi_{bq} |\xi_3|^2, \quad (3.17)$$

where we assume $\chi_{bb}, \chi_{bs} \ll \chi_{qb} \ll \chi_{qq}$. Compensation requires the susceptibility of each ω_i to drive magnitude $|\xi_i|^2$. We recall that the relationship between drive amplitude ξ_i s and drive strength eis apriori unknown. Our best access to the AC-Stark shift susceptibility is to measure the AC-Stark shift directly as a function of the DAC voltage $\tilde{V}(t)$ controlling the mode displacement.

We perform saturation spectroscopy dressed by the drive. The qubit is prepared in the ground state, and subjected to both the drive tone whose Stark-shift susceptibility we wish to characterize, and a coherent tone at frequency ω intended to excite the qubit when on resonance. These tones are applied simultaneously for a duration $t \gg T_2$ leaving the qubit in a mixed state $P_1 = P_0 = 1/2$ when ω is detuned appropriately for the Stark shift induced by the drive. By fitting the qubit resonance as a function of drive amplitude, we extract the quadratic dependence of the frequency shift on the drive amplitude, as desired [24]. The results of applying this protocol are shown in Fig. 3.5

The drives we apply may leak outside their target module. In particular, ω_1 and ω_3 drives intended for Alice leak to Bob through the communication channel. Fortunately, this is correctable by applying one of the previously described protocols on Bob, while sweeping the amplitude of a drive intended for Alice. What results is two Stark shift susceptibilities per ω_1 and ω_3 drive intended for Alice, but additionally influencing Bob and one Stark shift susceptibility per drive intended for Bob, and finally the Stark shift susceptibility of Alice and Bob to the ω_2 drive, for a total of eight calibrations.

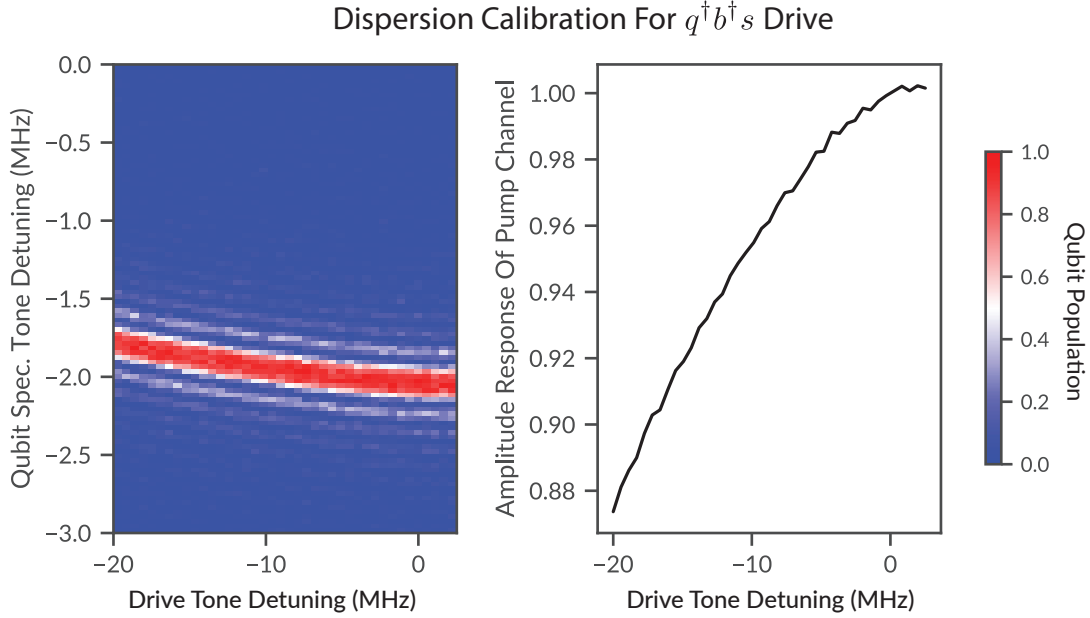


Figure 3.6: **Dispersion compensation: Experimental data** | Qubit dressed spectroscopy (left pane) for the Alice qubit in the presence of the $\mathbf{q}^\dagger \mathbf{b}^\dagger \mathbf{s} + \text{h.c.}$ drive applied at constant amplitude and varying frequency. Drift of the qubit line reveals the effective dispersion relation for the drive channel for the drive, using the qubit as a power meter through the Stark shift. We fit the qubit resonance frequency, and back out the amplitude dispersion of the line, normalized to zero detuning of the drive.

We remark that the stability of these calibrations is dependent upon the power stability of the amplification chain, which may be influenced by changes in room temperature and air currents, as well as supply voltage fluctuations. We found it helpful to automate the measurement of this calibration data, such that the susceptibilities may be conveniently recalibrated as necessary.

3.2.2 Dispersion compensation

An applied drive must traverse the microwave cables and various microwave hardware elements before finally inducing a current in the target Josephson junction. From the perspective of the Digital to Analog converter, the Stark shift susceptibility has not only power dependence, but frequency dependence. In particular, for a Stark shift term of the form $-\chi |\xi|^2$, and transfer function from DAC voltage to drive displacement defined by $\xi[\omega] = S_{\xi V}[\omega] V[\omega]$, we obtain a Stark shift of $-\chi |S_{\xi V}[\omega_p] V_0|^2$ for a drive signal of the form $V(t) = V_0 \cos(\omega_p t)$. If drive tones are to be chirped to stay on resonance, we must

compensate for the dispersive effects of $S_{\xi V}[\omega]$, such that for each frequency chirped to, the appropriate amount of power is applied to realize the desired g .

We may calibrate these dispersive effects using a modified version of either of the two Stark shift measurement protocols explained in the previous section [24]. Rather than sweeping the amplitude of $V(t)$, we instead fix the amplitude V_0 , and sweep the frequency ω_p such that the qubit is Stark shifted by $-\chi |S_{\xi V}[\omega_p] V_0|^2$. While this protocol only provides access to the magnitude of $S_{\xi V}[\omega_p]$, the phase component is mostly inconsequential for our purposes. In practice we extract the unitless quantity $S_{\text{lines}}[\omega] = |S_{\xi V}[\omega] / S_{\xi V}[\omega_0]|$, with ω_0 being the frequency at which the drive is expected to be resonant with no Stark shift, corresponding to zero detuning of the drive. The data from applying this protocol on Alice for the $\mathbf{q}^\dagger \mathbf{b}^\dagger \mathbf{s}$ drive and extracted $S_{\text{lines}}[\omega]$ are shown in 3.6. The remaining drives show similar dispersion relation, with a maximum amplitude deviation over the maximum chirp range of 20%.

3.2.3 Drive induced decoherence

All complicating effects of the drives discussed thus far may be compensated. Unfortunately, there are additional effects that these off-resonant drives cause, for which no compensatory mechanism is known. In particular, strong drives can cause decoherence and relaxation of the qubit, as shown in Fig. 3.7. The mechanism by which this happens is still being understood. Currently, the only known method to deal with this issue is to simply not drive so hard that it becomes an issue. There exists a careful balance in the choice of drive power. For a certain drive power, the drive causes a certain amount of decoherence, but also induces a certain g for the process of interest. Additional g implies that transferring a certain amount of population using this process will be quicker, and thus the gate will be shorter. A shorter gate then has the benefit of requiring the drive to be enabled for a shorter time. Rather than an exhaustive search for the ideal pulse amplitude and time, we cap the amplitude of the control pulses we generate to induce displacements that do not exceed the knee in the plots of Fig. 3.7.

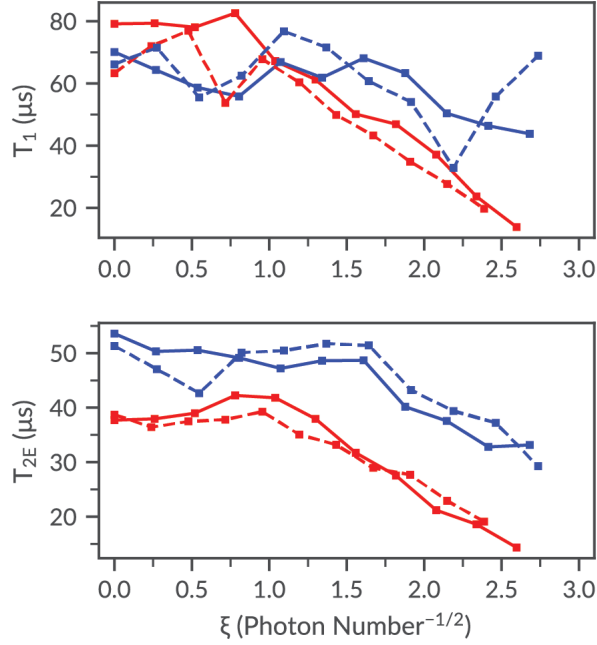


Figure 3.7: **Drive induced decoherence** | Relaxation and dephasing of Alice (red) and Bob (blue) in the presence of the first round drives (solid lines) and second round drives (dashed lines). For a dressed T_1 sequence, the qubit is placed in the $|e\rangle$ state, the drive is enabled for a time t with a displacement ξ , and then the qubit read out. For a dressed T_{2E} sequence, the qubit is placed in $|+X\rangle$, the drive enabled for a time $t/2$ at a strength ξ , disabled, the qubit flipped, the drive re-enabled again for a time $t/2$ at strength ξ , after which the qubit is read out. Decay envelopes are then fit, where the characteristic time of the decay in the presence of the drive is plotted above.

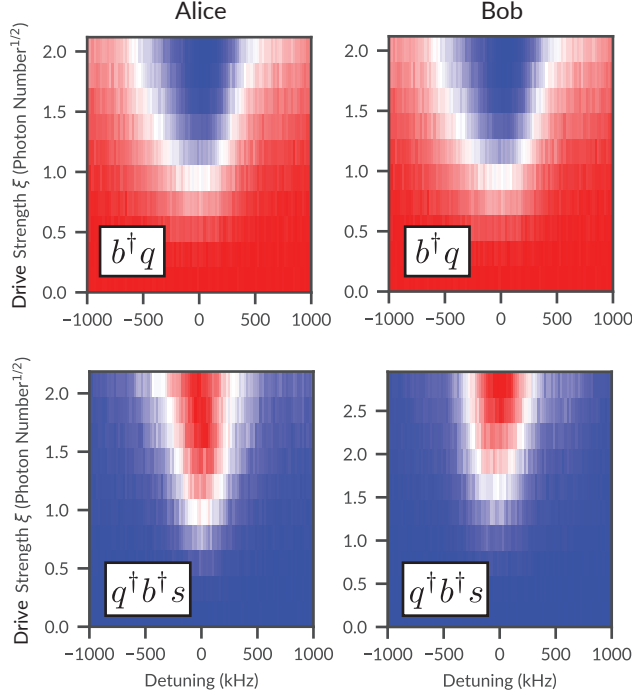


Figure 3.8: **Verification of Stark shift compensation** | Qubit dressed spectroscopy in the presence of each drive used in the experiment. The qubit is started in $|0\rangle$ for the $\mathbf{q}^\dagger \mathbf{b}^\dagger \mathbf{s} + \text{h.c.}$ and $|1\rangle$ for $\mathbf{b}^\dagger \mathbf{q} + \text{h.c.}$ For each drive strength, we apply a $3 \mu\text{s}$ pulse where the resonance condition for the transition is expected to match for that drive strength, plus a small detuning plotted on the x-axis. A peak well centered at 0 detuning demonstrates that the model predicts the resonance matching condition and compensates for induced Stark shift.

3.2.4 Experimental verification of Q-switching and extraction of process susceptibility to drive

In this section, we put all tools previously developed in this chapter together to verify control over the strength of the $\mathbf{b}^\dagger \mathbf{q} + \text{h.c.}$ parametric process and the $\mathbf{q}^\dagger \mathbf{b}^\dagger \mathbf{s} + \text{h.c.}$ processes on both the Alice and Bob quantum processing modules. At this point, we refer to the strength of the drives using the effective mode displacements ξ_i , as defined in Chapter 2. Again we repeat that these mode displacements correspond not to any individual mode displacement, but to an effective displacement which assumes that the drive addresses one mode. To calibrate $\xi_{1,2,3}$, we referred the DAC output amplitude to the Stark shift measured in Section 3.2.1,

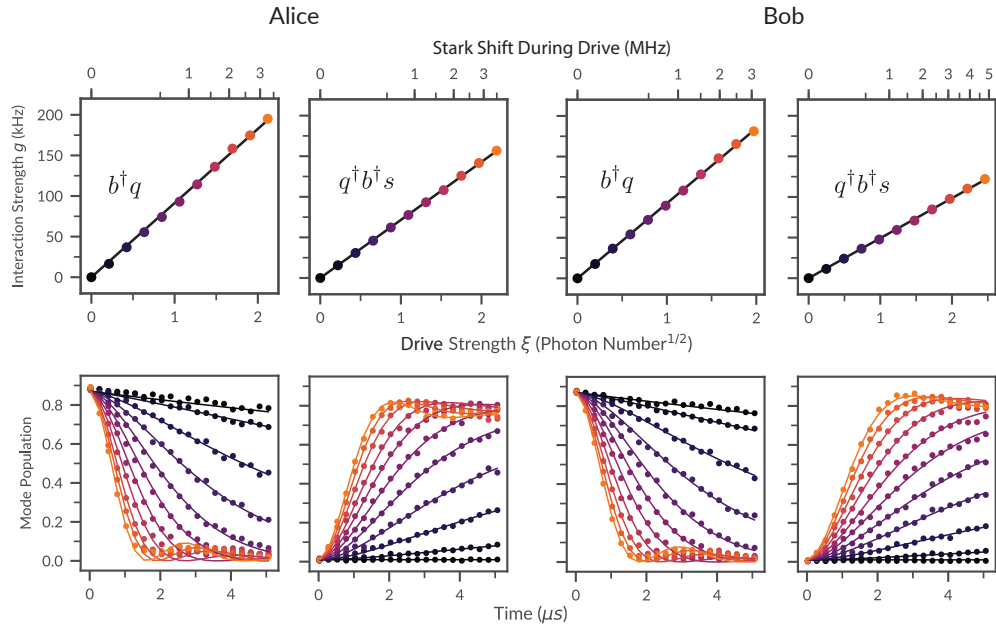


Figure 3.9: **Extraction of g vs. drive amplitude** | Bottom panels Alice and Bob qubit population when driving the associated parametric process for swept drive amplitude (color) and time (x-axis). For the processes $\mathbf{b}^\dagger\mathbf{q} + \text{h.c.}$, the qubit is initialized in the $|1\rangle$ state, whereas for $\mathbf{q}^\dagger\mathbf{b}^\dagger\mathbf{s} + \text{h.c.}$ the storage is initialized in $|1\rangle$. Each envelope is fit to the damped Rabi oscillations derived in Section 3.1.1 to extract the interaction strength for a given drive amplitude. These drive amplitudes are then plotted against the extracted interaction strength in the upper panel. The linear fits calibrate the interaction strength as a function of drive strength, necessary for the generation of envelopes for the controlled release and capture of a flying photon.

using the dispersive shifts as a conversion factor through the relations derived in Chapter 2

$$\Delta_q = -\chi_{bq} |\xi_1|^2 - 2\chi_{qq} |\xi_2|^2 - \chi_{bq} |\xi_3|^2. \quad (3.18)$$

For the $\mathbf{q}^\dagger \mathbf{b}^\dagger \mathbf{s} + \text{h.c.}$ process, we swept the amplitude of the corresponding drive after preparing the qubit in vacuum and storage in the $|1\rangle$ state using the qubit-storage **SWAP** gate, while detuning the drive such that the drive stays on resonance, using the Stark shift calibrations. We compensated the amplitude of the drive using the calibration from Section 3.2.2, such that the effective drive strength was frequency independent. In Fig. 3.8 we incorporated a small detuning around the expected transition frequency. The measured transition stays well centered for all tested drive amplitudes on both Alice and Bob.

We now wish to refer our drive strength to the amplitude of the driven process. To do this, we prepared the qubit in vacuum and storage in the $|1\rangle$ state, and we played a variable length, variable amplitude drive, which was frequency and amplitude compensated in the same manner as the previous experiment. The damped Rabi oscillations of population between qubit, storage, and buffer modes were fit to Eq. 3.12, extracting the interaction strength g as a function of drive amplitude, with data and fits shown in 3.9. We found a susceptibility of 76.4 kHz/ $\sqrt{\text{Photon}}$ for Alice, and 45.9 kHz/ $\sqrt{\text{Photon}}$ for Bob. We also remark that it is possible to calculate the relationship between g and ξ_3 in terms of measured cross-Kerrs. By application of the relationship between cross-Kerrs $\chi_{ab} = 2\sqrt{\chi_{aa}\chi_{bb}}$, we find

$$g_3 = \chi_{bq} \sqrt{\frac{\chi_{qs}}{2\chi_{qq}}} \xi_3, \quad (3.19)$$

giving process susceptibilities of 99 kHz/ $\sqrt{\text{Photon}}$ for Alice, and 53 kHz/ $\sqrt{\text{Photon}}$ for Bob, showing fair agreement with the calibration.

To verify the functionality of the $\mathbf{b}^\dagger \mathbf{q} + \text{h.c.}$ process and calibrate its interaction strength, we applied experiments similar to those used to calibrate the $\mathbf{q}^\dagger \mathbf{b}^\dagger \mathbf{s} + \text{h.c.}$ process, with the following modification: The experiments were started with the qubit in the $|1\rangle$ state and the storage in vacuum, and we also applied the two drives needed to activate the process simultaneously. We fixed the amplitude of the ξ_2 drive on Alice to $0.13\sqrt{\text{Photon}}$ and on Bob

to $0.12 \sqrt{\text{Photon}}$. These displacements were chosen empirically to induce minimal change in coherence times of the Alice and Bob qubits. No dispersion compensation was necessary, as the drive amplitude was fixed. The induced Stark shifts on Alice (4.94 MHz) and Bob (5.06 MHz) were measured at their set amplitudes and considered fixed frequency offsets during the application of drive pulses. Extracting the process susceptibilities as before, but with the fixed ξ_2 drive, we found a process susceptibility of $0.097 \text{ kHz}/\sqrt{\text{Photon}}$ for Alice, and $0.086 \text{ kHz}/\sqrt{\text{Photon}}$ for Bob. As before, we may calculate the process susceptibilities using measured cross-Kerrs using the relationship $g = \chi_{qr} \xi_1 \xi_2^*$, which for the fixed ξ_2 drive, gives a susceptibility for the ξ_1 drive of $0.105 \text{ kHz}/\sqrt{\text{Photon}}$ for Alice, and $0.101 \text{ kHz}/\sqrt{\text{Photon}}$ for Bob, showing good agreement with the calibration.

With the Stark shifts tamed and process amplitudes under our control, we are well prepared to use these processes for the controlled release and capture of single microwave photons. We will discuss theoretical considerations, and demonstrate the experimental realization of this procedure in the next chapter.

Chapter 4

Single Photon Transfer Between Two Nodes of a Quantum Network: Principle and Practical Realization

We have thus far developed the tools to apply gates between the various modes within a quantum processing module, and we have developed the tools to control communication of the module with the outside world. The modular quantum computer detailed in the introduction chapter involves numerous quantum processing modules, all connected by a router. In this dissertation, we take a small step towards such an architecture with two such modules with fixed connectivity between the two modules. In this chapter, we first explain how two quantum processing modules are connected, and the formalisms we use to treat systems with the coupling we use. Next, we characterize the quantum channel we realize in the experiment. Then, we develop the tools for efficiently transferring single microwave photons over this channel using the parametric drives developed earlier, and finally, apply these tools in the experiment.

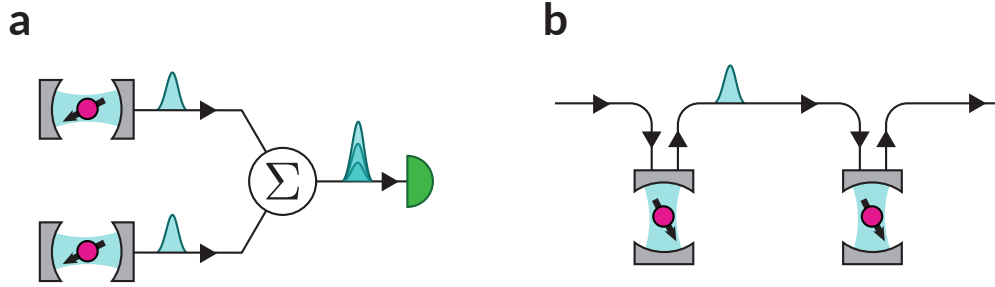


Figure 4.1: **Concurrent and sequential remote entanglement** | Here we show two different types of networks that most remote entanglement schemes fall into. On panel a, we show remote entanglement of the concurrent type, where qubits (pink), are coupled to a network using a buffer cavity (blue). Both systems begin by broadcasting flying photons (blue Gaussians), which arrive at a path information eraser (circle with Σ), which for this particular concurrent remote entangler, sums the fields. A photon-number-sensitive detector (green half-circle) projects the qubits into the entangled state when measuring the arrival of one photon. On panel b, we show a sequential remote entanglement setup. Such setups are broadly characterized as systems where both qubits have a chance to interact with a flying photon which travels from sending system to receiving system. The flying photon may begin and end its travel in the sending system and receiving system, or it may be created and terminated by systems external to the diagram.

4.1 A survey of different methods for quantum network connectivity

In the field of superconducting quantum computation, remote entanglement schemes are generally implemented with two different connectivity strategies: concurrent and sequential. In concurrent remote entanglement, we generate entanglement through the use of coincidence counts of flying qubits from independent sources [48, 49]. We suppose two quantum processing modules Alice and Bob, connected in a network of the type visualized in Fig. 1.1a., with stationary qubits q_A and q_B , who each broadcast flying qubits f_A and f_B , where stationary qubits are entangled with stationary qubits. We suppose the entanglement is, for example

$$|\psi\rangle = \mathcal{N}^{-1} (|q_A = 0, f_A = 0\rangle + |q_A = 1, f_A = 1\rangle) \otimes (|q_B = 0, f_B = 0\rangle + |q_B = 1, f_B = 1\rangle). \quad (4.1)$$

The key feature of concurrent remote entanglement is that these flying states are generated concurrently, and that q_A never interacts with f_B , and q_B never interacts with f_A . The

entanglement is generated through the use of a joint measurement on the $f_A \otimes f_B$ system, which is manifestly blind to local information. We first suppose some element which is able to erase which-origin information, that is, any information encoded on the flying state which betrays local information about the originating qubit. For example, let us imagine a device which sums f_A and f_B , creating a new qubit f such that $|\psi\rangle$ may be written

$$\begin{aligned} \mathcal{N}|\psi\rangle &= (|q_A = 0, q_B = 0\rangle) \otimes |f = 0\rangle \\ &+ (|q_A = 0, q_B = 1\rangle + |q_A = 1, q_B = 0\rangle) \otimes |f = 1\rangle \\ &+ (|q_A = 1, q_B = 1\rangle) \otimes |f = 2\rangle \end{aligned} \tag{4.2}$$

Measuring $f_A + f_B$ with the outcome 1 will project the $q_A \otimes q_B$ system into an odd Bell state. Such concurrent schemes are necessarily non-deterministic, as measurement is required to project out entanglement between the $q_A \otimes q_B$ and the $f_A \otimes f_B$. Concurrent entanglement schemes have been realized in optical systems [50] using flying optical photons, as well as in superconducting qubits using flying photon states [51]. Additionally, such which-origin information erasure has been attempted for flying coherent states in superconducting qubits, though quantum correlations were below the threshold of entanglement [52].

In this dissertation, we consider an entanglement scheme of the sequential type. Such sequential remote entanglers are broadly characterized by systems in which Alice and Bob are both given a chance to interact with a single flying qubit f . Such systems break down into two subcategories, namely sequential entanglement by measurement, and pitch-and-catch remote entanglement. In sequential entanglement by measurement, a flying qubit f , provided by an external source, interacts with q_A to generate entanglement

$$|\psi\rangle = \mathcal{N}^{-1} (|q_A = 0, f = 0\rangle + |q_A = 1, f = 1\rangle). \tag{4.3}$$

The flying qubit f is then interacted with Bob in some way, to create three body entanglement between Alice, Bob, and f . In this case, we suppose that the interaction creates the state $|\psi\rangle$ identical to Eq. 4.2. We remark that in this case, rather than a device external to Alice and Bob erasing the which-qubit information, the information is erased by the in-

teraction of f and q_B . Finally, entanglement is generated by measurement of the state of f , where again, in the $f = 1$ case, the back-action of the measurement entangles q_A and q_B . Schemes of the sequential entanglement by measurement type have been realized in superconducting qubits in the work of Roch et al. [53].

Thus far, we have explored a scheme with two modules, an information eraser, and a detector, and then a scheme with two modules and no information eraser. Taking this one step further, we can remove the need for a detector entirely, while retaining the simple network structure in sequential entanglement by measurement. With the removal of the detector, we additionally realize an entanglement scheme which is deterministic. In the scheme of pitch and catch remote entanglement, initially proposed in the seminal work by Cirac et al. [21], a flying qubit f is sourced by the Alice system entangled with q_A , and then subsequently absorbed by the Bob qubit q_B . The protocol crucially takes place in a completely closed system, where a unitary gate generates entanglement between q_A and f , and another unitary gate exchanges the entanglement between q_A and f to q_A and q_B . Pitch-and-catch remote entanglement schemes have been realized using superconducting qubits in the work of Campagne-Ibarcq et al. [24], Axline et al. [23], Kurpiers et al. [22]. In this dissertation, we build upon these schemes to realize a photon-loss-robust pitch and catch remote entanglement scheme. Let us now treat in detail the theory and design of this sequential-type network.

4.2 Two modules and a one-way channel: Cascaded quantum systems

While pitch-and-catch remote entanglement takes place in a closed system, the network it is built on is not. We may want to take a quick step back and explore the various options for connecting two modules at a distance. With a scheme chosen, we then explore the theory of how to couple our modules to such a network in the language of input-output theory, and then in the language of cascaded quantum systems. Finally, we explore how our choice of network facilitates rapid joint qubit readout, which is necessary for characterizing the entanglement we generate.

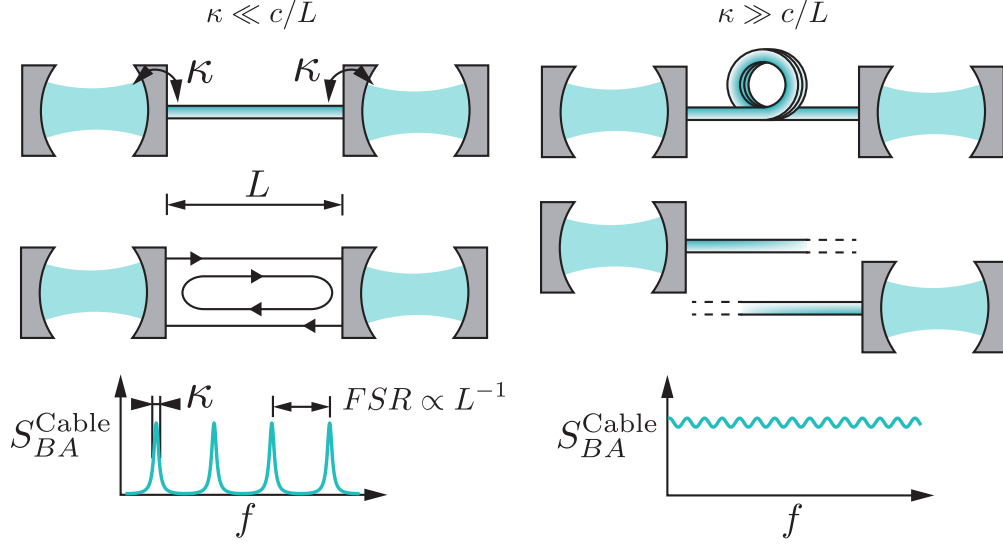


Figure 4.2: **Direct connection between two quantum processing modules** | Here we demonstrate the two limiting conditions of a two-module system connected by a segment of microwave coax. On the left panel, two Fabry-Perot cavities are connected with a cable, such that the coupling between the cables and the cavity is small relative to the free spectral range of the cable. This results in a comb of discrete modes living in the cable. In the opposite limit, where the free spectral range of the cable is small relative to the coupling, the modes of the cable merge into a continuum.

4.2.1 Schemes for the connection of two quantum processing modules

At first blush, the obvious scheme for connecting two quantum processing modules is a piece of microwave coax. At any appreciable distance between modules, some cable (or other microwave conduit) will be required, so why involve additional microwave circuit elements? Such schemes have been implemented in the framework of circuit QED [54, 55, 56], and generally break down into one of two limits. One limit, where $\kappa \ll c/L$, where L is the length of the connecting cable, and κ is the coupling between the buffer mode and the cable, and the opposite limit where $\kappa \gg c/L$. In the former limit, the piece of coax connecting the two cavities forms a $\lambda/2$ microwave resonator, hosting a number of discrete modes. These modes may temporarily host microwave photons for the transfer of quantum information from one module to the other. Such a scheme is limited to short lengths of cable, making its implementation in a large scale quantum computer challenging, or the regime of weak couplings, where the transfer will be slow. Additionally, such a scheme compromises modularity somewhat, as the cable modes hybridize with modes in both modules.

The alternative regime, where $\kappa \gg c/L$, allows the discrete peaks of the cable modes to merge together and blur out into a continuum. Intuitively, this may be understood as the regime where a photon leaking out of a sending mode will never overlap with its own reflections while being released. In this sense, over the timescale of the release, the cable appears to be matched. The work of Zhong et al. [56] enters this regime with a one meter long cable and an effective κ of $2\pi \cdot 50$ MHz, realized through a dedicated on-chip tunable couplers. The measured parametric couplings in the previous chapter reach a maximum of $2\pi \cdot 200$ kHz, necessitating an unreasonably long kilometer scale cable.

A system where we need not worry about cable resonances requires that, during the process of sending a photon, reflections of the sent photon do not impinge upon the sending cavity. Rather than using a long cable, we attempt to break the connection between the output field of Bob and the input field of Alice, leaving only the output field of Alice connected to the input field of Bob.

4.2.2 Theory of cascaded microwave quantum systems

Let us now explore how we will connect two of our quantum processing modules together to form a network. Connecting the output field of the Alice buffer module to the Bob buffer module input field requires that we separate the input fields from the output fields of our module, breaking reciprocity. We do this using a microwave circulator. The lossless three-port circulator, with ports A , B , and C , has the scattering matrix defined by

$$\begin{pmatrix} A_{\text{out}} \\ B_{\text{out}} \\ C_{\text{out}} \end{pmatrix} = \begin{pmatrix} 0 & 0 & 1 \\ 1 & 0 & 0 \\ 0 & 1 & 0 \end{pmatrix} \begin{pmatrix} A_{\text{in}} \\ B_{\text{in}} \\ C_{\text{in}} \end{pmatrix}. \quad (4.4)$$

We connect the buffer modes b_A and b_B to a pair of microwave circulators such that $b_{\text{out}}^A = b_{\text{in}}^A$, according to the signal flow graph in Fig. 4.3. For the purposes of this section, we suppose that b_{in}^A is in vacuum, such that we may consider only the unidirectional connection from Alice to Bob. By definition, Bob can not influence Alice, but the output field of Alice drives Bob. A system of this form is known as a cascaded quantum system, and has been

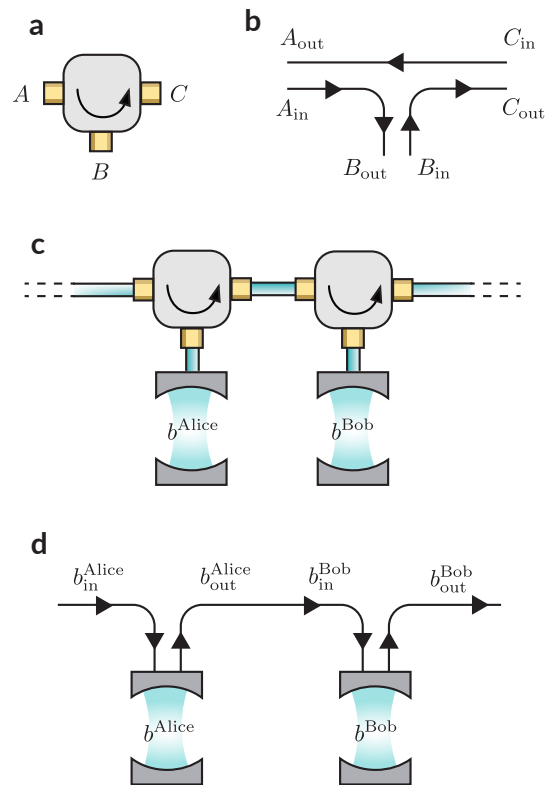


Figure 4.3: **Cascading microwave cavities using a circulator** | Panels a and b depict the ports of a circulator as well as the signal flow diagram. Panel c shows a unidirectional connection between cavities Alice and Bob realized using microwave circulators. The signal flow diagram for this configuration is shown in panel d.

treated a number of different ways throughout the history of quantum optics. Here we follow Gardiner and Zoller [33], but for more complex systems, we recommend the use of the modern SLH formalism [57].

For the case that the channel is lossless, we may write the quantum input-output relations for the Alice and Bob as

$$\mathbf{b}_{\text{out}}^A = \mathbf{b}_{\text{in}}^A + \sqrt{\kappa_A} \mathbf{b}_A \quad (4.5)$$

$$\mathbf{b}_{\text{in}}^B = \mathbf{b}_{\text{out}}^A \quad (4.6)$$

$$\begin{aligned} \mathbf{b}_{\text{out}}^B &= \mathbf{b}_{\text{in}}^B + \sqrt{\kappa_B} \mathbf{b}_B \\ &= \sqrt{\kappa_A} \mathbf{b}_A + \sqrt{\kappa_B} \mathbf{b}_B. \end{aligned} \quad (4.7)$$

We now combine this with the quantum Langevin equation, here written for an arbitrary operator \mathbf{a} acted on by a Hamiltonian H_{sys} , where the system mode \mathbf{c} is coupled to a transmission line at rate γ with transmission line modes $\mathbf{d}(t)$, giving

$$\dot{\mathbf{a}} = -\frac{i}{\hbar} [\mathbf{a}, \mathbf{H}_{sys}] - [\mathbf{a}, \mathbf{c}^\dagger] \left[\frac{\gamma}{2} \mathbf{c} + \sqrt{\gamma} \mathbf{d}_{\text{in}}(t) \right] + \left[\frac{\gamma}{2} \mathbf{c}^\dagger + \sqrt{\gamma} \mathbf{d}_{\text{in}}^\dagger(t) \right] [\mathbf{a}, \mathbf{c}], \quad (4.8)$$

Leading to the following quantum Langevin equation for an arbitrary operator \mathbf{a}

$$\begin{aligned} \dot{\mathbf{a}} &= -\frac{i}{\hbar} [\mathbf{a}, \mathbf{H}_{sys}] \\ &+ \left[-[\mathbf{a}, \mathbf{b}_A^\dagger] \left\{ \frac{\kappa_A}{2} \mathbf{b}_A \right\} + \text{h.c.} \setminus \mathbf{a} \right] \\ &+ \left[-[\mathbf{a}, \mathbf{b}_B^\dagger] \left\{ \frac{\kappa_B}{2} \mathbf{b}_B + \sqrt{\kappa_A \kappa_B} \mathbf{b}_A \right\} + \text{h.c.} \setminus \mathbf{a} \right], \end{aligned} \quad (4.9)$$

where the notation $\text{h.c.} \setminus \mathbf{a}$ implies the standard Hermitian conjugate of remaining terms with the modification the operator \mathbf{a} is not conjugated. Rearranging terms, we write this in the form

$$\begin{aligned} \dot{\mathbf{a}} &= -\frac{i}{\hbar} \left[\mathbf{a}, \mathbf{H}_{sys} + \frac{i\hbar\sqrt{\kappa_A\kappa_B}}{2} (\mathbf{b}_A^\dagger \mathbf{b}_B - \mathbf{b}_A^\dagger \mathbf{b}_B) \right] \\ &- \left[\mathbf{a}, \sqrt{\kappa_A} \mathbf{b}_A^\dagger + \sqrt{\kappa_B} \mathbf{b}_B^\dagger \right] \left\{ \frac{\sqrt{\kappa_A} \mathbf{b}_A + \sqrt{\kappa_B} \mathbf{b}_B}{2} \right\} + \text{h.c.} \setminus \mathbf{a} \end{aligned} \quad (4.10)$$

We now remark that this is precisely in the form of a Langevin equation where a non-Hermitian component $\frac{i\hbar\sqrt{\kappa_A\kappa_B}}{2} (\mathbf{b}_A^\dagger \mathbf{b}_B - \mathbf{b}_A^\dagger \mathbf{b}_B)$ is added to the Hamiltonian, as well as a combined dissipation channel, with operator $\sqrt{\kappa_A}\mathbf{b}_A + \sqrt{\kappa_B}\mathbf{b}_B$. This takes us directly to the system's Master equation

$$\dot{\rho} = -\frac{i}{\hbar} \left[\mathbf{H} + \frac{i\sqrt{\kappa_A\kappa_B}}{2} (\mathbf{b}_B^\dagger \mathbf{b}_A - \mathbf{b}_A^\dagger \mathbf{b}_B), \rho \right] + \mathcal{D} [\sqrt{\kappa_A}\mathbf{b}_A + \sqrt{\kappa_B}\mathbf{b}_B] \rho \quad (4.11)$$

Let us now treat the case where the channel is lossy. We suppose the channel has a quantum efficiency of η . Again, following Gardiner and Zoller [33], we suppose some portion of b_{out}^A will be lost in transmission, modeled by inserting a beam splitter in the channel b_{out}^A , coupled to the ancillary transmission line mode c , so that we have

$$\mathbf{b}_{\text{in}}^B = \sqrt{\eta}\mathbf{b}_{\text{out}}^A + \sqrt{1-\eta}\mathbf{c}_{\text{in}} \quad (4.12)$$

$$\mathbf{b}_{\text{out}}^B = \sqrt{1-\eta}\mathbf{c}_{\text{in}} + \sqrt{\eta}\mathbf{b}_{\text{in}}^A + [\sqrt{\eta\kappa_A}\mathbf{b}_A + \sqrt{\kappa_B}\mathbf{b}_B]. \quad (4.13)$$

$$\mathbf{c}_{\text{in}} = \sqrt{1-\eta}\mathbf{b}_{\text{out}}^A \quad (4.14)$$

Through means similar to the previous derivation, one may arrive at the master equation

$$\begin{aligned} \dot{\rho} = & -\frac{i}{\hbar} \left[\mathbf{H}_{\text{sys}} + \frac{i\sqrt{\eta\kappa_A\kappa_B}}{2} (\mathbf{b}_B^\dagger \mathbf{b}_A - \mathbf{b}_A^\dagger \mathbf{b}_B), \rho \right] \\ & + \mathcal{D} [\sqrt{\eta\kappa_A}\mathbf{b}_A + \sqrt{\kappa_B}\mathbf{b}_B] \rho + \mathcal{D} [\sqrt{(1-\eta)\kappa_A}\mathbf{b}_A] \rho \end{aligned} \quad (4.15)$$

4.3 Simulating the full cascaded system

Using the cascaded master equation 4.15, we write the full master equation for our system

$$\begin{aligned} \dot{\rho} = & -\frac{i}{\hbar} \left[\mathbf{H}_{\text{sys}} + \mathbf{H}_{\text{drive}} + \frac{i\sqrt{\eta\kappa_A\kappa_B}}{2} (\mathbf{b}_B^\dagger \mathbf{b}_A - \mathbf{b}_A^\dagger \mathbf{b}_B), \rho \right] \\ & + \mathcal{D}[\sqrt{\eta\kappa_A} \mathbf{b}_A + \sqrt{\kappa_B} \mathbf{b}_B] \rho + \mathcal{D}[\sqrt{(1-\eta)\kappa_A} \mathbf{b}_A] \rho \\ & + \sum_{i=A,B} \frac{\Gamma_\phi^i}{2} \mathcal{D}[\mathbf{q}_i^\dagger \mathbf{q}_i] \rho + \Gamma_1 \mathcal{D}[\mathbf{q}_i] \rho + \Gamma_{1,\text{Cav}} \mathcal{D}[\mathbf{q}_i] \rho \end{aligned} \quad (4.16)$$

$$\mathbf{H}_{\text{sys}}/\hbar = \sum_{i=A,B} \delta_b^i \mathbf{b}_i^\dagger \mathbf{b}_i - \chi_{bq} \mathbf{b}_i^\dagger \mathbf{b}_i \mathbf{q}_i^\dagger \mathbf{q}_i \quad (4.17)$$

$$\mathbf{H}_{\text{drive}}/\hbar = \sum_{i=A,B} \left(g_2^i(t) \mathbf{b}_i^\dagger \mathbf{q}_i + \text{h.c.} \right) + \left(g_3^i(t) \mathbf{b}_i^\dagger \mathbf{q}_i^\dagger \mathbf{s}_i + \text{h.c.} \right), \quad (4.18)$$

where we introduced dephasing terms for each qubit at the rate $\Gamma_\phi^i = 1/T_2^i - 1/(2T_1^i)$, decay terms for each qubit $\Gamma_1^i = 1/T_1^i$, and decay terms for each storage mode $\Gamma_{1,\text{Cav}}^i$, where i indexes each module A for Alice and B for Bob. We also introduce terms for the parametric drives in $\mathbf{H}_{\text{drive}}$ at the rate $g_2^i(t)$ for the $\mathbf{b}_i^\dagger \mathbf{q}_i + \text{h.c.}$ process and $g_3^i(t)$ for the $\mathbf{b}_i^\dagger \mathbf{q}_i^\dagger \mathbf{s}_i + \text{h.c.}$ process, where again i indexes each module. Finally, we introduce detuning and cross-Kerr terms in \mathbf{H}_{sys} to capture frequency and dispersive shift mismatches throughout the protocol.

We integrate the master equation numerically using the qutip software package [58, 59] and its master equation solver `mesolve`. Simulation of time-varying control signals is done as follows: we suppose all time-varying parameters $g_i^j(t)$ are band limited to a bandwidth B . Over a time $\tau \ll 1/B$, all time-varying parameters are approximately stationary. We propagate a state $\rho(t)$ to $\rho(t + \tau)$ by holding all time-varying parameters to their value at the beginning of the interval, in a piecewise-constant approximation, and calling `mesolve` to propagate the state forward over this interval. Repeated invocations of `mesolve` N times propagating the state to a final time $T = t + N\tau$. In practice, we choose $\tau = 50$ ns, where a doubling this parameter has demonstrated minimal effect on the final simulated state $\rho(T)$.

The choice of dephasing and decay term strength is crucial for accurate simulation. Using the coherence times from Tbl. 2.1 is too conservative, as the pumps will induce additional dephasing. Instead, we cross-reference $g(t)$ to the measured dephasing time induced by the

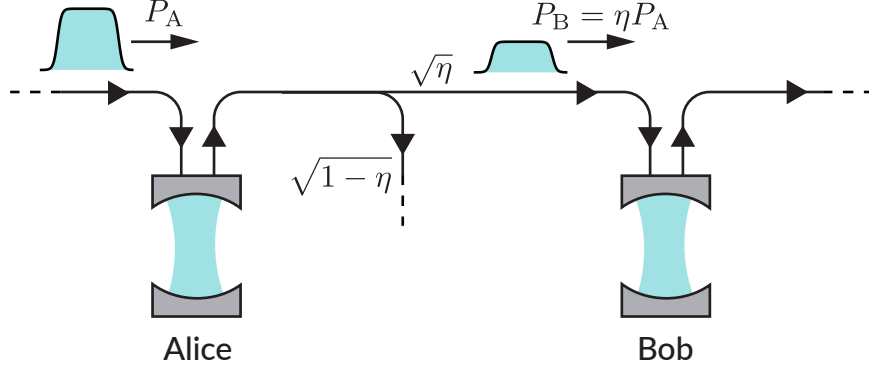


Figure 4.4: **Measuring quantum efficiency of a cascaded quantum system** | Two cavities Alice and Bob connected by a unidirectional channel, interposed by a splitter (input port not pictured) used to model loss in the channel. A pulse which rings up to a power of P_A bounces off the Alice system, encounters the channel loss, and then impinges on Bob with a reduced power $P_B = \eta P_A$. Using Alice and Bob to measure P_A and P_B extracts the channel's quantum efficiency η .

pump at maximum amplitude, taken from the data in Fig. 3.7. Accurate representation of decay and decoherence processes is less important for bare population measurement as is done in this chapter, but important for estimating entangled state fidelity.

4.3.1 Benchmarking our quantum channel

The critical figure of merit for our quantum channel is its quantum efficiency, or, the probability of a photon to traverse the channel without being absorbed. Entanglement between modules will be mediated by photons emitted and absorbed near the buffer mode frequencies, and therefore we aim to measure the quantum efficiency at these frequencies. To do this, we apply a tone near the buffer mode frequencies, which bounces off the Alice buffer mode, traverses the communication channel, and then bounces off Bob, as shown in Fig 4.4. The power due to this tone that Alice sees will be P_A , and for Bob P_B . The ratio $\eta = P_B/P_A$ is the quantum efficiency of the line at the frequency of the applied tone.

We may extract these powers P_A and P_B using a Ramsey interference experiment. First, we recall Eq. 2.19

$$\Delta_m = \chi_{bq} \text{Re} [\beta_g(t) \beta_e^*(t)], \quad (4.19)$$

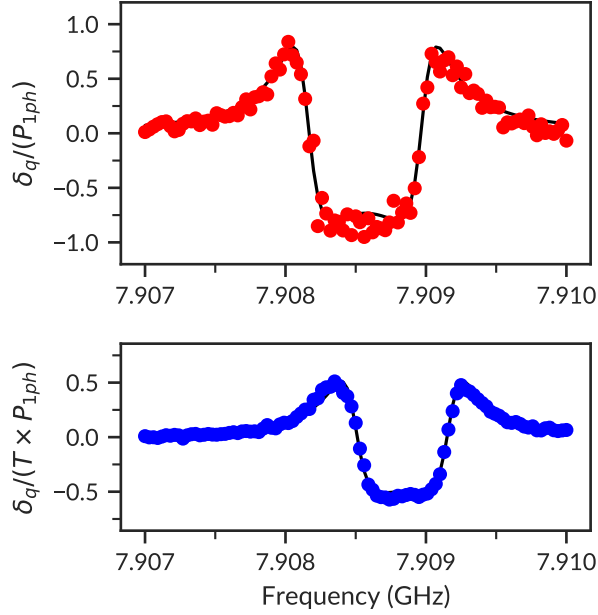


Figure 4.5: **Cavity Stark shift due to drive on buffer modes** | Plot of the normalized value of the Stark shift for Alice and Bob when varying the frequency f of a tone bouncing off each buffer cavity. The normalizing power P_{1ph} for Alice and ηP_{1ph} Bob are extracted simultaneously, yielding the quantum efficiency of the channel near the buffer mode frequencies. The quantum efficiency is found to be 0.64. The fit also extracts buffer mode frequencies, dispersive shifts, and transmission line couplings, shown in Table 2.1.

which gives the Stark shift induced when one of the buffer modes is driven near resonance. Here we suppose that the cavities are driven with square pulses, for time $T \gg \kappa, \chi$, amplitude ϵ , with detuning from buffer mode $|g\rangle$ frequency Δ , giving

$$\beta_g = \frac{\sqrt{\kappa}\epsilon}{i\Delta - \frac{\kappa}{2}} \quad (4.20)$$

$$\beta_e = \frac{\sqrt{\kappa}\epsilon}{i(\Delta - \chi_{bq}) - \frac{\kappa}{2}}, \quad (4.21)$$

which when combined with $B(t)$ gives

$$B = \frac{4|\epsilon|^2 \kappa \chi_{bq} (\kappa^2 + 4\Delta(\Delta - \chi_{bq}))}{(4\Delta^2 + \kappa^2) (\kappa^2 + 4(\Delta - \chi_{bq})^2)}. \quad (4.22)$$

We extract the detuning induced by a variable amplitude, variable length, and variable

frequency pulse near the buffer mode using a Ramsey interference experiment. The qubit is prepared on the equator, the pulse enabled for a time T , and the phase of the qubit read out by a π pulse, followed by readout, extracting the frequency shift. We fit the quadratic dependence of the induced Stark shift on the pulse amplitude, and plot the fit coefficient versus pulse frequency in Fig. 4.5. To this data, we fit the expression for $\Delta_m(\omega)$, extracting qubit-buffer Stark shift χ_{bq} , buffer transmission line coupling κ , buffer resonant frequency ω_b . Importantly, we also extract a relationship between the drive amplitude at the level of the DAC, $\epsilon = AV_d$, capturing the attenuation of the lines to the input port of the cavity. Here we assume that the dispersion of the lines is minimal over the bandwidth of the frequency sweep. The quantum efficiency is extracted as $\eta = P_B/P_A = \epsilon_A^2/\epsilon_B^2 = A_A^2/A_B^2$, where subscripts denote the powers, drive amplitudes, and DAC to drive amplitude conversion coefficient for the Alice and Bob systems, extracting a quantum efficiency of 0.64, comparable to other cascaded quantum systems experiments in circuit QED [53, 24].

4.4 Synthesis of optimal pitch and catch drive waveform

We now wish to embark on using the parametric processes under control to release and capture microwave photons. Here we present an algorithm for transferring microwave photons over the channel using the $\mathbf{q}^\dagger\mathbf{b} + \text{h.c.}$ process, but we note that the following algorithm applies equally to the control of the $\mathbf{b}^\dagger\mathbf{q}^\dagger\mathbf{s} + \text{h.c.}$ process, by mapping the states $|q=0\rangle \rightarrow |s=0, q=1\rangle$ and $|q=1\rangle \rightarrow |s=1, q=0\rangle$. Additionally, we find that restricted version of this calculation is analytically soluble, and documented in Appendix B. We begin by writing the equations of motion for the qubit and buffer mode system. Following Campagne-Ibarcq et al. [24], we write the Hamiltonian for the qubit and buffer mode system under the influence of the $\mathbf{q}^\dagger\mathbf{b} + \text{h.c.}$ process

$$\mathbf{H}/\hbar = \delta\mathbf{b}^\dagger\mathbf{b} + g(t)\mathbf{q}^\dagger\mathbf{b} + \text{h.c.}, \quad (4.23)$$

where we have placed ourselves in a rotating frame detuned δ from the buffer mode. This detuning will be necessary for releasing and capturing photons at a frequency slightly detuned from the buffer mode frequency. This capability is required, as the buffer mode frequen-

cies of Alice and Bob do not match exactly. In particular, the rotating frame we are in corresponds to the rotating frame of the captured or released photon. Additionally, in this section, we write $g(t)$ without the subscript 2 or 3 corresponding to the process of interest, as all results here for the synthesis of $g(t)$ applies to both drives.

Following Cirac et al. [21], if some control sequence leads to efficient pitch and catch of a “full” photon in a given wavepacket when Alice is initially in $|g\rangle$, the same sequence applied when Alice is initially in $\sqrt{\epsilon}|g\rangle + \sqrt{1-\epsilon}|e\rangle$ will lead to the transfer of a photon in the same wavepacket with amplitude $\sqrt{\epsilon}$, coherently superposed with the system remaining idle in $|e\rangle$ with amplitude $|1-\epsilon\rangle$. When $\epsilon \ll 1$, from Bob’s point of view, this means catching a small coherent state. Thus, we can compute the catch sequence considering that the field to be caught is coherent, so that we may write the scalar Langevin equations. Given that \mathbf{b} is coupled to the transmission line at a rate κ , we write the scalar Langevin equation equations for \mathbf{b} and \mathbf{q}

$$\dot{b} = -i\delta b - ig^*(t)q - \frac{\kappa}{2}b - \sqrt{\kappa}b_{\text{in}} \quad (4.24)$$

$$\dot{q} = -ig(t)b \quad (4.25)$$

$$\sqrt{\kappa}b = b_{\text{out}} - b_{\text{in}}. \quad (4.26)$$

Suppose we wish to capture a particular wavepacket impinging upon the Bob cavity, $b_{\text{in}}(t)$, normalized as $\int_0^T |b_{\text{in}}|^2 = n_{\text{phot}} \ll 1$. Following Korotkov [60], a perfect catch implies no field is reflected off Bob’s cavity, such that $b_{\text{out}} = 0$, giving that $b(t) = -b_{\text{in}}(t)/\sqrt{\kappa}$, yielding the following equations

$$\dot{b}_{\text{in}} + i\delta b_{\text{in}} - \frac{\kappa}{2}b_{\text{in}} = ig^*(t)q \quad (4.27)$$

$$ig(t)b_{\text{in}} = \sqrt{\kappa}\dot{q}. \quad (4.28)$$

At each discrete time-step t , knowing $q(t)$, one then computes $g(t)$ in order to satisfy Eq. 4.27. We then propagate q to $t + dt$ with Eq 4.28 and iterate up to the final time T . Note however that this equation diverges if we choose $q = 0$ as the initial state: a symmetry

allows one to choose arbitrarily the phase of g as long as q is initially displaced with the same phase. We regularize this formal divergence by giving a small real value $q_0 \ll \sqrt{n_{\text{phot}}}$ to the field at $t = 0$.

The case of pitching a photon with Alice can be treated similarly. We find Alice’s Langevin equation from Bob’s by re-labeling the states $|g\rangle \rightarrow |e\rangle$ and the field operator as $q \rightarrow q^\dagger$. One can again consider pitching a coherent state with a shape b_{out} and containing a small number of photons n_{phot} . In practice, we will choose the same shape for Alice’s pitch and Bob’s catch so that $b_{\text{out}}^A(t) = b_{\text{out}}^B(t + \tau)$. Here, $t \ll T$ is the (negligible) propagation delay between Alice and Bob. We then compute $g(t)$ by imposing $b = b_{\text{out}}/\sqrt{\kappa}$ at all time t .

The choice of the initial state with respect to n_{phot} is here crucial. If we choose $q^\dagger(0)^2 = n_{\text{phot}}$, the qubit will end up in $|e\rangle$ and the pitch is full. If alternatively we set $q^\dagger(0)^2 = n_{\text{phot}}/2$ we get a “half-pitch” and generate entanglement between the two qubits. To avoid diverging control pulses when the qubit nears $|e\rangle$ at the end of the full pitch, we reduce the number of photons in the pulse in the same manner as when catching a wavepacket with a qubit initially in $|g\rangle$.

4.4.1 Compensating for Stark shift and dispersion

Having generated the optimal $g(t)$ for the pitch or catch process, we now want to generate microwave control signals that implement this $g(t)$ for the process of interest. The microwave control signals are generated in a phase-coherent manner using the microwave circuitry detailed in Appendix A. The control signals originate at DACs which control the in-phase and quadrature channels of an IQ mixer. The IQ mixer is fed a local oscillator tone corresponding to where the pump is expected to be resonant, with a small known frequency detuning to facilitate single-sideband modulation. We will suppose that these DACs emit signals corresponding to the real and imaginary components of a complex voltage $\tilde{V}(t)$, with the real part of $\tilde{V}(t)$ controlling the I channel of the IQ mixer, and the imaginary part controlling the Q channel of the IQ mixer. For the purposes of this section, we will ignore the finite detuning used in experiment, and suppose that a constant $\tilde{V}(t) = V_0$ corresponds to a tone resonant with the drive’s corresponding process with no induced Stark shift. Here,

we address this Stark shift by chirping the control signal.

We begin first by using the process susceptibility calibrations from 3.2.4, through which we refer $g(t)$ back to control voltages on the DACs. Next, we add frequency modulation to the signal to ensure that the pump stays resonant for all t . For a particular $\tilde{V}(t)$ and a Stark shift calibration $\tilde{\chi}$ with units of Frequency/Volt², measured in Ch. 3.2.1, we generate a Stark-shift compensated control signal

$$\tilde{V}'(t) = \tilde{V}(t) \exp\left(-2\pi i \int_0^t dt' \tilde{\chi} |\tilde{V}(t')|^2\right). \quad (4.29)$$

In chirping the pulse in frequency, the pulse the module sees will be reshaped by the dispersion of the lines and intervening microwave components. Using the line dispersion calibration from Chapter 3.2.2 $S_{\text{lines}}[\omega]$, we compensate for this effect through inverse filtering. The small variance of $S_{\text{lines}}[\omega]$ from unity over the spectral range of the pulse ensures that this process is numerically stable. Operating on the frequency domain representation of the chirped pulse $\tilde{V}'[\omega]$, the compensated pulse $\tilde{V}''[\omega]$ is calculated $\tilde{V}''[\omega] = S_{\text{lines}}^{-1}[\omega] \tilde{V}'[\omega]$.

In practice, the measured dispersion data $S_{\text{lines}}[\omega]$ was fit to a third-order polynomial. Calculated $g(t)$ was up-sampled to the sampling rate of our DACs, 500 megasamples per second. From this, we calculated $\tilde{V}'(t)$, converted $\tilde{V}'(t)$ to its frequency domain representation by fast Fourier transformation, inverse filter using the polynomial representation of $S_{\text{lines}}[\omega]$, and finally return to the time domain with an inverse fast Fourier transformation.

4.4.2 Pulse truncation

At this point, we specialize to wavepackets of the form $\alpha \operatorname{sech}(\beta t)$, as such wavepackets admit analytical $g(t)$ when no detuning is required. We expect that the small detuning necessary should have minimal influence upon insights gleaned from examining analytical solutions. It follows from expressions in Appendix B that the bulk of the transfer occurs during a small portion during the middle of the overall transfer. Inspired by this, we truncate the control pulse to play from $\tilde{V}(-T/2)$ out to $\tilde{V}(T/2)$. The effect of this is to reduce the quantum efficiency of the transfer. Indeed since our protocol is robust to photon loss, an imperfect transfer due to imperfect transfer pulses will result in a correctable error and reduced success

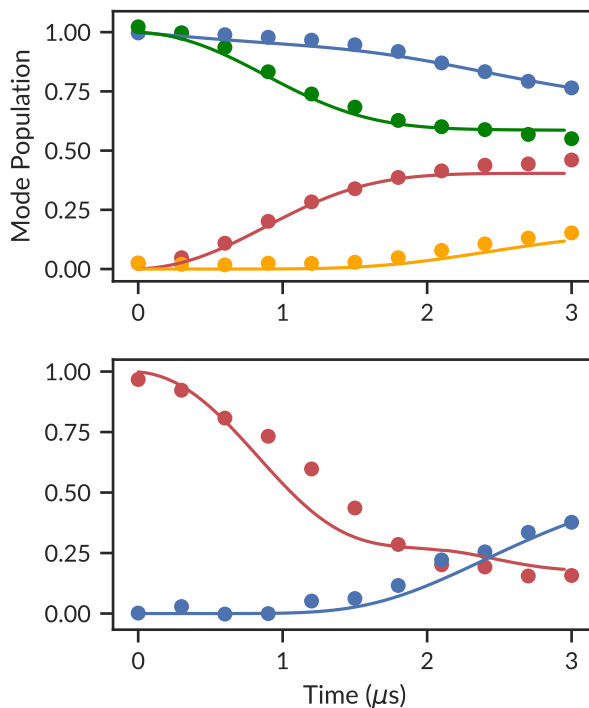


Figure 4.6: **Mode populations during photon transfer** | We plot mode populations of Alice qubit (red), Bob qubit (blue), Alice storage (green), and Bob storage (yellow) during the first (upper) round of the protocol, corrected for readout contrast. We verify (lower) the second round of the protocol through the controlled release and capture of one microwave photon using the calibrated parametric drives and generated control envelopes. Dots denote experimental measurements taken through the early termination of the protocol after time t , followed by readout of qubit and storage mode populations. Lines are predictions using a full master equation simulation, showing good agreement with experimental data.

probability. We find, through simulation of the full time-bin entanglement protocol described in the next chapter, that transfer pulses with $\beta = (3 \mu s)^{-1}$ and $T = 3 \mu s$ optimize the fidelity of the generated entangled state. Such pulses are expected to be 80% efficient relative to their un-truncated version, extracted through master equations simulation.

4.5 Experimental results and analysis

We now turn to verifying the controlled release and capture of a flying photon using the previously described parametric processes. We test combinations of processes necessary for the time-bin entanglement process described in the next chapter: a full-pitch on Alice using the $\mathbf{q}^\dagger \mathbf{b} + \text{h.c.}$ process and full-catch on Bob using $\mathbf{q}^\dagger \mathbf{b} + \text{h.c.}$, and then a half-pitch

on Alice using $\mathbf{b}^\dagger \mathbf{q}^\dagger \mathbf{s} + \text{h.c.}$ and a full-catch on Bob using $\mathbf{b}^\dagger \mathbf{q}^\dagger \mathbf{s} + \text{h.c.}$. Each process was verified by preparing Alice and Bob subsystems for appropriate states for the transfer process, namely $|q_A = 1, s_A = 0\rangle \otimes |q_B = 0, s_B = 0\rangle$ for the testing of the $\mathbf{q}^\dagger \mathbf{b} + \text{h.c.}$ processes, and $|q_A = 0, s_A = 1\rangle \otimes |q_B = 1, s_B = 0\rangle$ for the $\mathbf{b}^\dagger \mathbf{q}^\dagger \mathbf{s} + \text{h.c.}$ processes. Next, we synthesized control pulses using techniques from the previous section. For the $\mathbf{q}^\dagger \mathbf{b} + \text{h.c.}$ process, we synthesized control envelopes implementing the full transfer of an excitation; a full pitch on Alice and a full-catch on Bob. This means that we expect a final state $|q_A = 0, s_A = 0\rangle \otimes |q_B = 1, s_B = 0\rangle$. For the $\mathbf{b}^\dagger \mathbf{q}^\dagger \mathbf{s} + \text{h.c.}$ process, we synthesized control envelopes that implemented an entangling operation, such that the final state of the system is expected to be

$$\frac{1}{\sqrt{2}} (|q_A = 0, s_A = 1\rangle \otimes |q_B = 1, s_B = 0\rangle + |q_A = 1, s_A = 0\rangle \otimes |q_B = 0, s_B = 1\rangle). \quad (4.30)$$

Fig. 4.6 show the data corresponding to the mode populations of Alice and Bob during the application of these pulses. To extract the time-dependent behavior, the transfer process is terminated early, and the mode populations read out. Such a process only approximately extracts the mode population, as the early termination of a pulse results in transient oscillations, an effect most significant when the control signal is at maximum amplitude. We expect generated pulses to be 80% efficient due to truncation. This inefficiency affects the final state during the pitch process and again during the catch process. For the $\mathbf{q}^\dagger \mathbf{b} + \text{h.c.}$ process, we therefore expect the final q_B population to be $(80\%)^2 \cdot \eta = 38\%$. For the $\mathbf{b}^\dagger \mathbf{q}^\dagger \mathbf{s} + \text{h.c.}$ process, we transfer only half a photon, and therefore expect the final s_B population to be half this. The data in Fig. 4.6 agree well with these predictions. We correct for readout contrast, calibrated through the individual preparation of each mode in each state followed by readout. Additionally, Fig. 4.6 is overlaid with master equation simulation data, where we use the same $g(t)$ waveform used for the synthesis of pulses as was used in experiment, with the data showing good agreement with simulation. No free fitting parameters used for the curves in this plot.

Chapter 5

Time-Bin Entanglement

In this chapter, we explain the principle of our time-bin entanglement protocol for generating entanglement between two quantum processing modules in a photon loss robust manner. We apply techniques for the controlled release and capture of microwave photons from the previous chapter over two rounds, in such a way that one photon is sent, delocalized between the two rounds. The Bob qubit functions as a round-insensitive photon detector, ensuring the photon has made its journey successfully. Parametric processes applied to the Bob module encode the round in which the photon was received into the Bob storage mode, creating entanglement between Alice and Bob storage cavities. We additionally explain how to characterize the entanglement generated between the two storage cavities. Finally, we explain the results of applying our time-bin entanglement protocol and verify that by detecting photon loss errors, we can enhance the fidelity of remote entanglement.

5.1 Introduction to our time-bin entanglement protocol

Quantum error detection requires that the consequences of errors be separable from the intended message from the sender, by the message recipient. Time-bin entanglement achieves this by sending one photon always, and detecting if it has been absorbed in the channel, where the quantum information is encoded in whether the photon arrives at its destination early or late [5, 6, 7]. In the field of quantum optics, generation of a time-bin qubit has been accomplished through the use of an unbalanced Mach-Zener interferometer [5, 6], where an

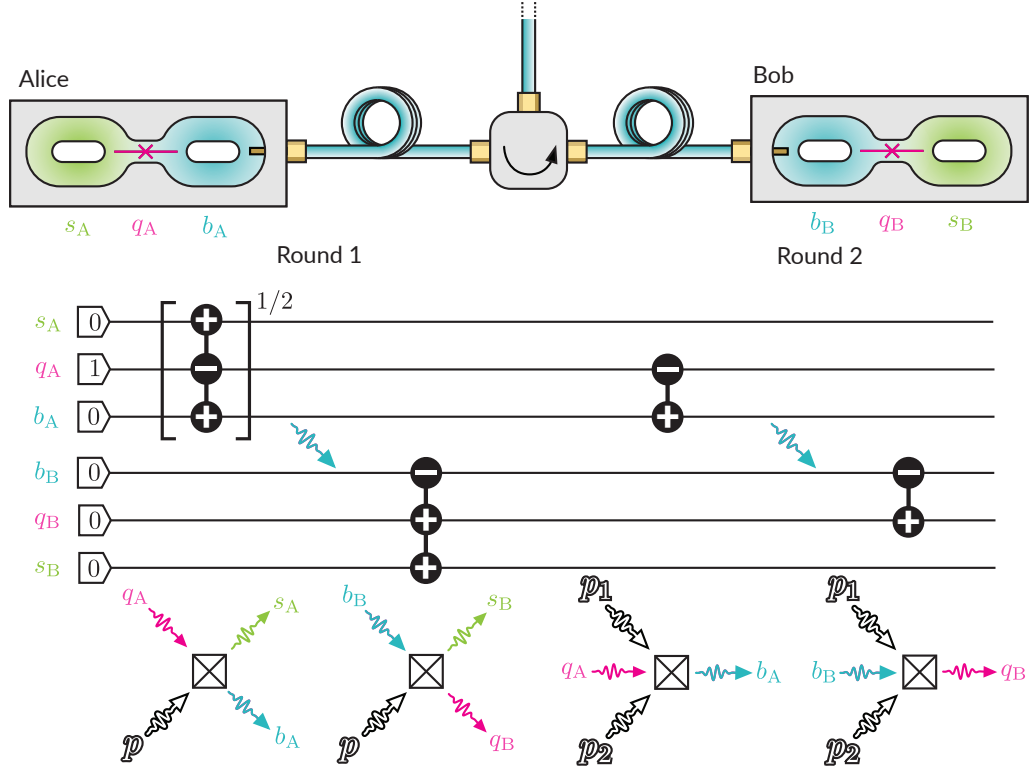


Figure 5.1: **High level schematic of protocol** | Upper Panel: Simplified schematic of the circuit QED setup implementing photon-loss robust remote entanglement. The circuit features two modules, each including a high-Q storage cavity s buffer mode b , and a transmon qubit bridging these two modes q . The modules are connected through superconducting microwave coax, intersected by a microwave circulator. Central Panel: Quantum circuit implementing photon-loss robust remote entanglement. Circles joined by vertical bars denote the intended coherent addition (plus sign) and removal (minus sign) of photons in the associated modes. The first two gates perform the controlled release and capture of a microwave photon entangled with all six degrees of freedom of the system. The remaining photon left in the Alice qubit if a photon had not been pitched on the first round is then pitched on the second, ensuring one photon is always sent. The second round catch finally ensures that the Bob transmon is left excited if and only if the one pitched photon is received successfully, independent of which round, heralding the success of the protocol Lower Panel: The parametric processes in the transmon qubits activated to implement the gate above. Double line arrows denote applied parametric drives.

input wavepacket is split and passed through long and short paths, and the two paths joined to provide a traveling superposition of early wavepacket and late wavepacket. Associating the two quasi-orthogonal modes corresponding to the early wavepacket and late wavepacket to \mathbf{t}_e and \mathbf{t}_l , and writing joint states of these modes $|\mathbf{t}_e \mathbf{t}_l\rangle$, we may write a time-bin state as

$$|\psi\rangle = \frac{1}{\sqrt{2}} (|\text{Early}\rangle + |\text{Late}\rangle) = \frac{1}{\sqrt{2}} (|\mathbf{10}\rangle + |\mathbf{01}\rangle). \quad (5.1)$$

The process of spontaneous parametric downconversion then creates entangled pairs of this state, yielding two entangled time-bin qubits, whose entanglement may be verified through coincidence counts. In the field of circuit QED, couplings and parametric process amplitudes set the timescales of the wavepackets our systems may process. For good temporal separation, a delay line of length $c/g_{\max} = c/(200 \text{ kHz}) = 1.5 \text{ km}$ is not practical. Instead, the generation of time-binned states may be accomplished in two rounds.

We now describe a simplified version of the protocol we run to generate entanglement between the Alice storage mode and a flying time-bin qubit. The discussion that follows may be thought of a vertical segmentation of the circuit of Fig. 5.1, where we first focus on Alice as a time-bin encoder, and separately Bob as a time-bin decoder. We begin with one photon in the Alice qubit mode. In the first round of the protocol, a half-pitch operation removes half an excitation from the Alice qubit mode, and moves it to the storage mode and the buffer mode, where the excitation in the buffer mode leaks out into the channel, as in Ch. 4.4. Using the notation $|s_{AQ_A}\rangle |\mathbf{t}_e \mathbf{t}_l\rangle$, with \mathbf{t}_e and \mathbf{t}_l again denoting early and late wavepacket temporal modes of the transmission line, we create a state

$$|\psi_{1\text{st}}\rangle = \frac{1}{\sqrt{2}} (|01\rangle |\mathbf{00}\rangle + |10\rangle |\mathbf{10}\rangle). \quad (5.2)$$

We notice that in the sector where a photon was not ejected, the qubit remains excited. In this protocol, the qubit takes the role of the delay line, retaining the photon to be sent on the second round. Correspondingly, in the second round, a full-pitch gate transfers this remaining photon to the buffer mode, which then occupies the \mathbf{t}_l mode corresponding to

modes of the late ejected wavepacket, resulting in the following state

$$|\psi_{2\text{nd}}\rangle = \frac{1}{\sqrt{2}} (|00\rangle |\mathbf{01}\rangle + |10\rangle |\mathbf{10}\rangle). \quad (5.3)$$

The protocol concludes with the Alice qubit in the ground state, uninvolved with the entanglement between the Alice storage mode and time-bin flying qubit.

The decoding of a time-bin state requires two degrees of freedom, one corresponding to a qubit we intend to transfer entanglement to, and an ancillary mode we use for detecting photon loss. Crucially, the qubit to which we transfer the entanglement must be sensitive to the *state* of the time-bin qubit. An early arriving photon must map to one state in this qubit, and a late arriving photon must map to another. The ancillary mode, by contrast, must be sensitive to the *population* of the time-bin qubit, and *insensitive* to its state. If the ancilla was sensitive to the state of the time-bin qubit, the ancilla would be entangled with the time-bin qubit, resulting in decoherence of the generated entanglement upon measurement of the ancilla.

We now describe a simplified version of the protocol we run to capture and decode a flying time-binned qubit. Here, the entanglement transferred by the time-bin qubit will be exchanged into the storage mode, with the Bob qubit playing the role of the ancilla. First, we transfer the early-arriving photon into the storage mode of Bob. Using the notation $|\mathbf{t}_e \mathbf{t}_l\rangle |s_{BQB}\rangle$, and considering two branches corresponding to an early arriving photon and a late arriving photon, we begin the the protocol

$$|\psi_{\text{initial}}^{\text{early}}\rangle = |\mathbf{10}\rangle |00\rangle; |\psi_{\text{initial}}^{\text{late}}\rangle = |\mathbf{01}\rangle |00\rangle \quad (5.4)$$

and transfer an early arriving photon into both the Bob storage mode and Bob qubit mode

$$|\psi_{\text{initial}}^{\text{early}}\rangle = |\mathbf{00}\rangle |11\rangle; |\psi_{\text{initial}}^{\text{late}}\rangle = |\mathbf{01}\rangle |00\rangle. \quad (5.5)$$

The protocol is completed by transferring the late arriving photon into the Bob qubit mode *only*

$$|\psi_{\text{initial}}^{\text{early}}\rangle = |\mathbf{00}\rangle |11\rangle; |\psi_{\text{initial}}^{\text{late}}\rangle = |\mathbf{00}\rangle |01\rangle. \quad (5.6)$$

The final qubit state is completely insensitive to which round the photon arrived in, only *that* it arrived in either of the two rounds. It therefore satisfies the stated role of the ancilla mode. The storage mode, by contrast, is only excited by an early arriving photon, making it sensitive to the state of the time-bin qubit.

With the essential idea of our protocol detailed, let us now explain how the protocol is implemented.

5.2 Implementation of time-bin entanglement

We now discuss how time-bin entanglement is implemented in experiment. For ease of implementation and to maximize the fidelity of the realized entangled state, we make modifications to the previously described protocol. We also explain some finer implementation details that must be considered when applying the protocol on circuit QED hardware.

The protocol described in the previous section is flexible in its implementation. One may construct variants in which squeezing instead of conversion processes are used for generation of flying photons. One may also mix processes coupling three modes and two modes in one round. The following factors put constraints on acceptable parametric drives.

Symmetry For simplicity of implementation, we wish to choose identical parametric drives on Alice and Bob. Conveniently, all modes of Alice and Bob are matched to within 350 MHz, meaning that similar filtering approaches may be utilized. The microwave circuitry required to generate the needed pumps is complex, and a great many hours were spent finding the proper way to filter out mixer spurs. Choosing identical parametric drives on Alice and Bob meant that lessons learned designing the microwave circuitry for Alice applied equally to the microwave circuitry for Bob. Indeed many of the same amplifiers and filters were identical for Alice and Bob. The parts that were not reused were of identical part family, and generally of a neighboring part number to account for frequency discrepancies.

Drive Frequency The frequencies at which the drives are applied is restricted by module architecture and microwave components intervening between the module and the drive generation circuitry. The dilution refrigerator our experiment resided in was wired with SMA microwave cables. SMA connectors are standardly designed to perform well up to 18 GHz, with specialized components extending the band to 26.5 GHz [61]. A lower frequency drive is also advantageous due to microwave cables suffering higher losses at higher frequencies. The frequency of our drives is, in practice, bounded below, if a drive is to be delivered through the module’s waveguide port, which has a practical low-frequency cut-off of 8.2 GHz due to the waveguide’s standard WR90 dimensions.

Bob Qubit Final State Differing choices of parametric pumps imply differently coupled positive and negative frequencies, leading to differing conjugation of operators representing the pump process. The result is the same algorithm, with exchanges of $|0\rangle$ and $|1\rangle$. It is of paramount importance that the ancilla qubit is minimally subjected to a process which could result in an incorrect post-selection. To this end, we choose a combination of pumps which result in the Bob qubit $|1\rangle$ state representing success of the protocol, and the Bob qubit $|0\rangle$ representing failure. In this way, a T_1 event will lead to a false positive, rather than a false negative.

In addition to these factors, we also seek a set of processes that incorporate a spin-echo refocusing pulse between first and second rounds. An echo pulse is of particular interest due to the significant disparity between the Alice qubit’s T_{2E} time (43 μ s) and T_{2R} time (5.7 μ s). Focusing on the family of processes coupling three internal modes, we find that the $\mathbf{b}^\dagger \mathbf{q}^\dagger \mathbf{s} + \text{h.c}$ is activated by a pump positioned at $\omega_3 = \omega_q + \omega_b - \omega_s - \chi_{bq}$, occurring for Alice at 8545.69 MHz, and at 8667.07 MHz for Bob, positioned conveniently for the modules’ waveguide port. Such drives are conveniently paired with drives stimulating a $\mathbf{q}^\dagger \mathbf{r} + \text{h.c}$. process to realize time-bin entanglement with a spin-echo. Implementation of the $\mathbf{q}^\dagger \mathbf{r} + \text{h.c}$. process involves a number of additional technical complications not directly relevant to the current discussion, and so we cover its implementation in Appendix A.

We now work through the intermediate states of this modified protocol. We will use the notation $|q_A s_A\rangle |q_B s_B\rangle$, and neglect modes of the transmission line and the state of the

buffer mode, considering only moments where these modes are in vacuum. We begin with all modes in vacuum. In practice, this is implemented using feedback cooling. Qubit feedback cooling locally measures a module's qubit, applies a π pulse if the qubit is found to be in the excited state, and then remeasures to confirm that the qubit is indeed in the ground state. Storage mode feedback cooling starts with a previously cooled qubit, and then applies a **SWAP** gate between qubit and storage modes to move any existing population into the qubit, followed by qubit cooling. This process is repeated until the qubit is measured to be in the ground state after the **SWAP** gate. Next, the Alice storage is prepared in the $|1\rangle$ state by exciting the Alice qubit with a π pulse and applying a **SWAP** gate to move this excitation to the storage. The Bob qubit is prepared in the $|1\rangle$ state by π pulse, and all remaining modes are left in vacuum. This results in the initial state

$$|\psi_{\text{initial}}\rangle = |01\rangle |10\rangle. \quad (5.7)$$

Next, we apply a half pitch operation on Alice using the $\mathbf{b}^\dagger \mathbf{q}^\dagger \mathbf{s} + \text{h.c}$ process for Alice and a full catch operation on Bob using the corresponding $\mathbf{b}^\dagger \mathbf{q}^\dagger \mathbf{s} + \text{h.c}$ for Bob, resulting in the following state.

$$|\psi_{\text{1st}}\rangle = \frac{1}{\sqrt{2}} (|01\rangle |10\rangle + |10\rangle |01\rangle). \quad (5.8)$$

Applying π pulses on both Alice and Bob qubits implements the spin-echo, resulting in the state

$$|\psi_{\text{echoed}}\rangle = \frac{1}{\sqrt{2}} \left(\underbrace{|11\rangle |00\rangle}_{\text{Late photon arrival}} + \underbrace{|00\rangle |11\rangle}_{\text{Early photon arrival}} \right), \quad (5.9)$$

where we have labeled branches of the wavefunction corresponding to early and late photon arrival. We now apply drive stimulating the $\mathbf{q}^\dagger \mathbf{r} + \text{h.c.}$ process on Alice and a drive stimulating the $\mathbf{q}^\dagger \mathbf{r} + \text{h.c.}$ process on Bob, to transfer the photon in the Alice qubit to Bob, completing the protocol. With the design of our quantum processing module, all drives are storage population selective, as $\chi_{qs} \mathbf{q}^\dagger \mathbf{q} \mathbf{s}^\dagger \mathbf{s}$ cross-Kerr terms shift the qubit frequency as a

function of storage population. The “late photon arrival” branch of $|\psi_{\text{echoed}}\rangle$ on which the $\mathbf{q}^\dagger\mathbf{r} + \text{h.c.}$ term acts features a single excitation in the Alice storage and no excitations in the Bob storage. Additionally, we require that the $\mathbf{q}^\dagger\mathbf{r} + \text{h.c.}$ process *not* act upon the “Early photon arrival” branch, or else it will release the excitation corresponding to a first-round successful transfer out into the lines. We therefore tune the $\mathbf{q}^\dagger\mathbf{r} + \text{h.c.}$ drive on Alice to be $s_A = 1$ selective, and the $\mathbf{q}^\dagger\mathbf{r} + \text{h.c.}$ on Bob to be $s_B = 0$ selective. Applying these processes for a full pitch on Alice and a full catch on Bob results in the following state

$$|\psi_{2\text{nd}}\rangle = \frac{1}{\sqrt{2}} (|01\rangle |10\rangle + |00\rangle |11\rangle), \quad (5.10)$$

which may be factored

$$|\psi_{2\text{nd}}\rangle = \frac{1}{\sqrt{2}} (|s_A = 1\rangle |s_B = 0\rangle + |s_A = 0\rangle |s_B = 1\rangle) \otimes |q_A = 0, q_B = 1\rangle, \quad (5.11)$$

an odd Bell state between storage modes. Let us now treat the case of photon loss. Suppose between $|\psi_{\text{initial}}\rangle$ and $|\psi_{\text{echoed}}\rangle$, the sent photon is known to be lost. In this case,

$$|\psi_{1\text{st}}^{\text{lost},1}\rangle = |10\rangle |10\rangle \xrightarrow{\text{echo}} |\psi_{\text{echo}}^{\text{lost},1}\rangle = |00\rangle |00\rangle, \quad (5.12)$$

and the following $\mathbf{q}^\dagger\mathbf{r} + \text{h.c.}$ will fail to transfer any population to the Bob qubit, leaving it in its ground state. Now, we suppose a second round loss. Starting from the “Late photon arrival” branch of $|\psi_{\text{echoed}}\rangle$, as we’re presupposing a second-round transfer,

$$|\psi_{\text{echoed}}^{\text{lost},2}\rangle = |11\rangle |00\rangle \xrightarrow{\text{failed second round}} |\psi_{2\text{nd}}^{\text{lost},2}\rangle = |01\rangle |00\rangle, \quad (5.13)$$

again demonstrating that the protocol concludes with Bob in the ground state, as desired.

Having explained the protocol we apply in experiment, we now turn our focus towards characterizing the entanglement generated by this protocol.

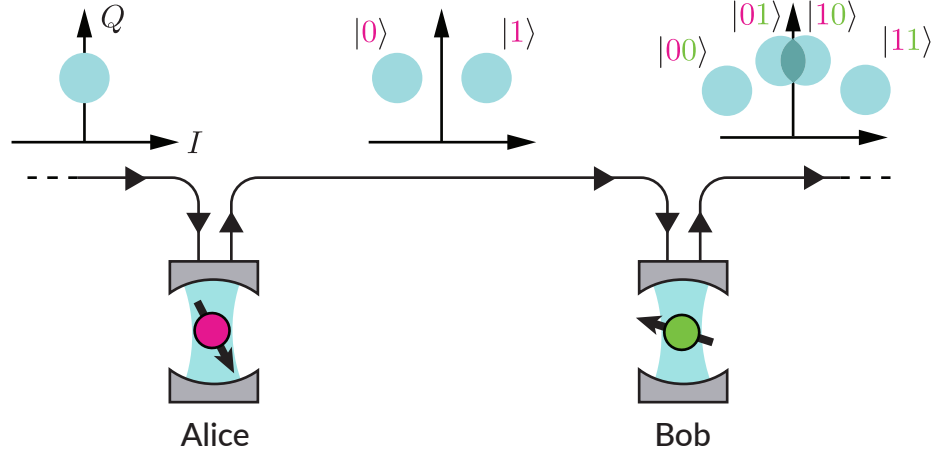


Figure 5.2: **Joint readout for a cascaded circuit QED system** | Two cavities with embedded dispersively coupled qubits are connected by a unidirectional channel. A microwave pulse is delivered to the Alice input port, where we show the phase-space representation of the integrated pulse plotted in the upper right corner. The two axes representing the in-phase (I) and quadrature (Q) components. The pulse then impinges on the Alice cavity, and acquires a qubit state dependent phase shift, shown in the central phase space plot. The pulse then continues along the channel to eventually impinge on Bob, where the pulse finally acquires an additional state dependent phase shift, resulting in four independent measurement outcome distributions corresponding to the joint qubit states $|00\rangle$, $|01\rangle$, $|10\rangle$, and $|11\rangle$.

5.3 Experimental verification of time-bin entanglement

5.3.1 Joint qubit readout and tomography

A necessary ingredient for characterizing the entanglement generated between Alice and Bob quantum processing modules is a way to extract the joint state of the two-qubit system in which the entanglement resides. While the final entanglement generated is between storage modes, we use the qubit-storage **SWAP** gate to transfer entanglement into the qubits, and then jointly read out the Alice and Bob qubits. To jointly read out Alice and Bob qubits, we apply a pulse to the Alice buffer input port. The flying pulse acquires a phase shift corresponding to the Alice qubit state, travels along the channel, and then acquires an additional phase shift corresponding to the Bob qubit state. The amplified and downconverted signal contains information about the state of the two-qubit system, given by the four measurement outcome distributions for each of the four two-qubit states $|00\rangle$, $|01\rangle$, $|10\rangle$, and $|11\rangle$, as shown in Fig. 5.2.

Extracting the joint two-qubit state from a single measurement by discriminating between each outcome distribution is possible, but has a number of caveats. For one, such a measurement will be skewed towards less-excited outcome distributions as T_1 during measurement will result in decay. Additionally, discriminating between all four outcome distributions can be somewhat technically challenging. Most importantly, such a measurement risks introducing additional correlations between each system; for instance, an error in extracting $|01\rangle$ population, such that it is corrupted by $|10\rangle$ population. Such a readout would not extract qubit populations in an independent manner.

We instead differentiate only between measurement outcomes corresponding to $|00\rangle$ and all other outcomes, acquiring one bit of information per readout. Such a measurement is sufficient for extracting all two-qubit information. We start by extracting the probability of measuring each $|00\rangle$, $|01\rangle$, $|10\rangle$, and $|11\rangle$. Our measurement accesses the probability of measuring $|00\rangle$ for a particular state ρ , or $\rho_{00} = \text{tr}(|00\rangle\langle 00| \rho)$. By applying single-qubit pre-rotations to ρ , $\mathbf{U} = \mathbf{U}_A \otimes \mathbf{U}_B$, resulting in a new state $\rho' = \mathbf{U}\rho\mathbf{U}^\dagger$, whose $|00\rangle$ component we write

$$\rho'_{00} = \text{tr}(|00\rangle\langle 00| \rho') = \text{tr}(\mathbf{U}^\dagger |00\rangle\langle 00| \mathbf{U} \rho). \quad (5.14)$$

By picking appropriate gates for \mathbf{U}_A and \mathbf{U}_B we extract probabilities

$$\rho_{00} = \text{tr}[|00\rangle\langle 00| \rho] = \text{tr}[(I \otimes I) |00\rangle\langle 00| (I \otimes I) \rho] \quad (5.15)$$

$$\rho_{01} = \text{tr}[|01\rangle\langle 01| \rho] = \text{tr}[(I \otimes X) |00\rangle\langle 00| (I \otimes I) \rho] \quad (5.16)$$

$$\rho_{10} = \text{tr}[|10\rangle\langle 10| \rho] = \text{tr}[(X \otimes I) |00\rangle\langle 00| (X \otimes I) \rho] \quad (5.17)$$

$$\rho_{11} = \text{tr}[|11\rangle\langle 11| \rho] = \text{tr}[(X \otimes X) |00\rangle\langle 00| (X \otimes X) \rho]. \quad (5.18)$$

Decomposing IZ , ZI , and ZZ into components we can write their expectation values in

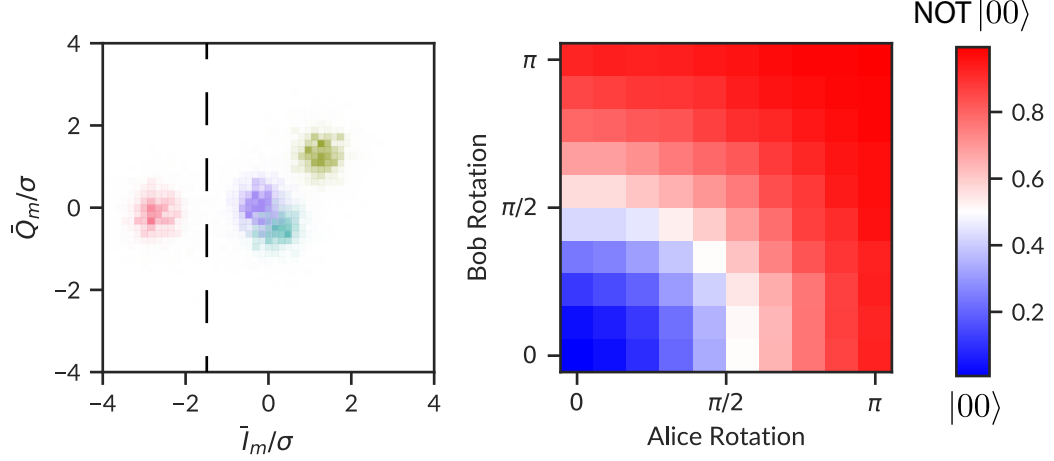


Figure 5.3: **Joint readout verification** | In the left panel, we histogram the measurement outcomes I_m/σ and Q_m/σ , corresponding to different preparations of the Alice and Bob qubits resultant from applying our joint measurement. On the left panel, we prepare Alice and Bob qubits at angles θ_A and θ_B respectively, apply our joint measurement, apply a threshold to the measured data (left panel: vertical black dotted line), and plot the dependence of measurement on preparation angle. We note that the histogram here is the result not of driving Alice in reflection as discussed in the main text, but from driving Alice in transmission, whose output field then bounces off Bob in reflection. This only has the consequence of moving the outcome distributions in phase space.

terms of measured quantities

$$\begin{aligned} \langle IZ \rangle &= \text{tr} [(|00\rangle\langle 00| - |01\rangle\langle 01| + |10\rangle\langle 10| - |11\rangle\langle 11|) \rho] \\ &= \rho_{00} - \rho_{01} + \rho_{10} - \rho_{11} \end{aligned} \quad (5.19)$$

$$\langle ZI \rangle = \rho_{00} - \rho_{10} + \rho_{01} - \rho_{11} \quad (5.20)$$

$$\langle ZZ \rangle = \rho_{00} + \rho_{11} - \rho_{10} - \rho_{01}. \quad (5.21)$$

Further pre-rotations on ρ provide access to remaining two-qubit Pauli components $\langle IX \rangle$, $\langle IY \rangle$, $\langle XI \rangle$, $\langle YI \rangle$, $\langle ZX \rangle$, ...

Having shown that this readout is sufficient for two-qubit tomography, we now characterize its implementation in our experiment. We use a $1.5 \mu\text{s}$ pulse, chosen to be comparable to $1/\kappa$ for each buffer mode. We begin by cooling both qubits by feedback, apply variable rotations $R_x^{\text{Alice}}(\theta_A)$ and $R_x^{\text{Bob}}(\theta_B)$, apply our joint readout, and plot the averaged measurement outcome as a function of the rotation angles in Fig. 5.3.

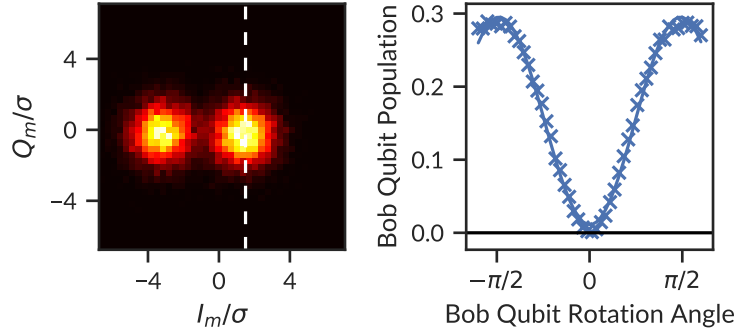


Figure 5.4: **Postselection readout** | In the left panel, we histogram the measurement outcomes I_m/σ and Q_m/σ of our postselection readout applied to the Bob qubit subsystem being prepared in the $2^{-1/2}(|g\rangle + |e\rangle)$ state. A vertical dotted line corresponds to the threshold dividing measurement outcomes which may correspond to Bob qubit state $|g\rangle$, and measurement outcomes corresponding to states we trust to correspond to $|e\rangle$. On the left panel, we measure Rabi oscillations of the Bob qubit with the postselection readout, extracting the readout contrast. When no π pulse is applied (corresponding to Bob Qubit rotation angle of 0), we find 16 out of the 17,000 repetitions signaling the excited state. This corresponds to a postselection failure probability of one part in a thousand. The Rabi contrast extracts that using this readout for post-selection will result in a hit of 30% to our protocol’s success probability in comparison to one which perfectly distinguishes $|e\rangle$ and $|g\rangle$.

To model and ultimately correct for readout error, we suppose that the actual qubit states are corrupted by a readout infidelity transfer matrix T mapping actual qubit populations to probabilities of measurement outcomes P_{00} and P_{100} , where $P_{00} = 1 - P_{100}$

$$\begin{pmatrix} P_{00} \\ P_{100} \end{pmatrix} = T \text{diag}(\rho) = \begin{pmatrix} 0.996 & 0.06 & 0.04 & 0.002 \\ 0.004 & 0.94 & 0.96 & 0.998 \end{pmatrix} \begin{pmatrix} \rho_{00} \\ \rho_{01} \\ \rho_{10} \\ \rho_{11} \end{pmatrix} \quad (5.22)$$

5.3.2 Postselection errors

To make this protocol work well, a high quality post-selecting measurement is crucial. Any infidelity due to poor postselection will be drastically magnified by the inverse of the success probability. A post-selection readout acting only on the Bob system is implemented by driving through the Bob waveguide input port, and allowing the dispersively-shifted field to leak out the Bob output port. This readout will completely bypass the Alice subsystem due

to the connectivity of the modules.

To avoid false positives, we choose an aggressive threshold for estimating the Bob qubit state. By placing the threshold on top of the outcome distribution for the Bob $|e\rangle$ state, we obtain two measurement outcomes: the first corresponding to Bob being in either $|g\rangle$ or $|e\rangle$, and the second corresponding to states for which we are certain that Bob is in the $|e\rangle$ state. Such aggressive thresholding sacrifices readout contrast and thus success probability of the protocol, as states which may in fact correspond to $|e\rangle$ (successful transfer), but our skeptical readout discards, are discarded.

To extract the readout contrast and false-positive probability, we measured Rabi oscillations of the Bob qubit with this postselection readout, with the data shown in Fig. 5.4.

5.3.3 Two-qubit tomography

While calculating the overall two-qubit state by inversion of Born's rule $\langle \mathbf{O} \rangle = \text{tr}(\rho \mathbf{O})$, is a simple, appealing way to construct a density matrix from measured data, it can result in density matrices which are unphysical. Noise on measured Pauli components may result in the reconstruction of a density matrix which is not positive-definite. We turn to the process of maximum likelihood estimation to reconstruct a physical density matrix from N measurements performed on identically prepared copies of a given system. We follow the explanation of Banaszek et al. [62]. Quantum mechanically, each measurement is described by a positive operator-valued measure (POVM). The outcome of the i th measurement corresponds to the realization of a specific element of the POVM used in the corresponding run. We shall denote this element by \mathcal{F}_i . The likelihood functional $\mathcal{L}(\rho)$ describes the probability of obtaining the set of outcomes for a given density matrix ρ . For measurements performed on repeated preparations of the system, it is given by the product

$$\mathcal{L}(\rho) = \prod_{i=1}^N \text{tr}(\rho \mathcal{F}_i). \quad (5.23)$$

After the experiment is performed, the operators \mathcal{F}_i are determined by the outcomes of the measurements. The unknown element of the above expression, which we want to infer from

our data, is the density matrix describing the measured ensemble. The general estimation strategy of the maximum likelihood technique is to maximize the likelihood functional over the set of the density matrices. We introduce a parameterization of the set of density matrices which provides an efficient algorithm for maximization of the likelihood function. We represent the density matrix in the form

$$\boldsymbol{\rho} = \mathbf{T}^\dagger \mathbf{T}, \quad (5.24)$$

which automatically guarantees that $\boldsymbol{\rho}$ is positive and Hermitian. The remaining condition of unit trace $\text{tr}\boldsymbol{\rho} = 1$ will be taken into account using the method of Lagrange multipliers. In order to achieve the minimal parameterization, we assume that \mathbf{T} is a complex lower triangular matrix, with real elements on the diagonal, resulting in a total of 16 free parameters. In numerical calculations, it is convenient to replace the likelihood functional by its natural logarithm, which of course does not change the location of the maximum. Thus, the function subjected to numerical maximization is given by

$$L(\mathbf{T}) = \sum_{i=1}^N \ln \text{tr}(\mathbf{T}^\dagger \mathbf{T} \mathcal{F}_i) - N \text{tr}(\mathbf{T}^\dagger \mathbf{T}), \quad (5.25)$$

where the second term ensures that $\boldsymbol{\rho}$ satisfies $\text{tr}\boldsymbol{\rho} = 1$. To constrain $\boldsymbol{\rho}$, we wish for $\mathcal{F}_i = |\mu_i\rangle \langle \mu_i|$ where μ_i is an orthonormal basis in the Hilbert space of the two qubits. Continuing from the previous section, in lab we measure

$$\rho'_{00} = \text{tr}(\mathbf{U}^\dagger |00\rangle \langle 00| \mathbf{U} \boldsymbol{\rho}), \quad (5.26)$$

where $\mathbf{U} = \mathbf{U}_A \otimes \mathbf{U}_B$ corresponds local two-qubit rotations on Alice and Bob. In this case, we can write a projection operators for the measurement protocol

$$\mathcal{F}_{i,j} = \mathbf{U}_{i,j}^\dagger |00\rangle \langle 00| \mathbf{U}_{i,j} = \left(\mathbf{U}_A^i \otimes \mathbf{U}_B^j\right)^\dagger |00\rangle \langle 00| \mathbf{U}_A^i \otimes \mathbf{U}_B^j, \quad (5.27)$$

where we choose the set of $\mathbf{U}_{i,j}$ to be all two qubit Clifford gates, leading to trivial construction of $\mathcal{F}_i = |\mu_i\rangle \langle \mu_i|$ as desired.

Maximum likelihood estimation is additionally very useful for correcting for readout error. Intuitively, the process of maximum likelihood estimation fits a physical density matrix to a set of measurements. If we parameterize our density matrix to be one uncorrupted by error, we may fit this density matrix, after application of our error model, to our measured data. This corresponds to the altered projection operator

$$\mathcal{F}_{i,j} = \mathbf{U}_{i,j}^\dagger \begin{pmatrix} T_{11} & 0 & 0 & 0 \\ 0 & T_{12} & 0 & 0 \\ 0 & 0 & T_{13} & 0 \\ 0 & 0 & 0 & T_{14} \end{pmatrix} \mathbf{U}_{i,j}, \quad (5.28)$$

where T_{mn} are elements of the readout infidelity transfer matrix. We use these projection operators to recover the qubit states at the end of our entanglement protocol.

An additional useful tool maximum likelihood estimation provides is sampling error estimation. We quote the result from Banaszek et al. [62] establishing that, for the parameters of \mathbf{T} in the vector form as \mathbf{t} , the covariance matrix for the parameters \mathbf{t} is given by

$$V = G^{-1} - \frac{G^{-1}\mathbf{u}\mathbf{u}^T G^{-1}}{\mathbf{u}^T G^{-1}\mathbf{u}}, \quad (5.29)$$

with the matrix $G = -\partial^2 L / \partial \mathbf{t} \partial \mathbf{t}'$ and the gradient $\mathbf{u} = \partial \text{tr}(\mathbf{T}^\dagger \mathbf{T}) / \partial \mathbf{t}$. We use this covariance matrix, propagated to the reported Pauli components, to report error on the measured density matrix.

We find a ρ that maximizes the likelihood function numerically using the `tensorflow` library. The training of artificial neural networks involves finding the minimum of a nonlinear functional much the same as maximum likelihood estimation does, and the automatic differentiation capabilities of the `tensorflow` library neatly provides gradient and Hessian information for use in the calculation of V .

5.3.4 Gate verification

As a sanity test, we apply all possible local two-qubit Clifford gates to Alice and Bob qubits, prepared in their ground states by feedback cooling, and perform two-qubit tomography. The

Alice Gate	Bob Gate	F_{Target}	Alice Gate	Bob Gate	F_{Target}
I	I	0.97	$R_Y(\pi/2)$	I	0.99
I	$R_X(\pi)$	0.99	$R_Y(\pi/2)$	$R_X(\pi)$	0.99
I	$R_X(\pi/2)$	0.99	$R_Y(\pi/2)$	$R_X(\pi/2)$	0.99
I	$R_Y(\pi/2)$	0.99	$R_Y(\pi/2)$	$R_Y(\pi/2)$	0.99
I	$R_X(-\pi/2)$	0.99	$R_Y(\pi/2)$	$R_X(-\pi/2)$	0.99
I	$R_Y(-\pi/2)$	0.99	$R_Y(\pi/2)$	$R_Y(-\pi/2)$	0.99
$R_X(\pi)$	I	0.98	$R_X(-\pi/2)$	I	0.99
$R_X(\pi)$	$R_X(\pi)$	0.99	$R_X(-\pi/2)$	$R_X(\pi)$	0.98
$R_X(\pi)$	$R_X(\pi/2)$	0.99	$R_X(-\pi/2)$	$R_X(\pi/2)$	0.99
$R_X(\pi)$	$R_Y(\pi/2)$	0.98	$R_X(-\pi/2)$	$R_Y(\pi/2)$	0.99
$R_X(\pi)$	$R_X(-\pi/2)$	0.99	$R_X(-\pi/2)$	$R_X(-\pi/2)$	0.99
$R_X(\pi)$	$R_Y(-\pi/2)$	0.99	$R_X(-\pi/2)$	$R_Y(-\pi/2)$	0.99
$R_X(\pi/2)$	I	0.99	$R_Y(-\pi/2)$	I	0.98
$R_X(\pi/2)$	$R_X(\pi)$	0.99	$R_Y(-\pi/2)$	$R_X(\pi)$	0.99
$R_X(\pi/2)$	$R_X(\pi/2)$	0.99	$R_Y(-\pi/2)$	$R_X(\pi/2)$	0.99
$R_X(\pi/2)$	$R_Y(\pi/2)$	0.99	$R_Y(-\pi/2)$	$R_Y(\pi/2)$	0.99
$R_X(\pi/2)$	$R_X(-\pi/2)$	0.99	$R_Y(-\pi/2)$	$R_X(-\pi/2)$	0.98
$R_X(\pi/2)$	$R_Y(-\pi/2)$	0.99	$R_Y(-\pi/2)$	$R_Y(-\pi/2)$	0.98

Table 5.1: **Fidelity of Two-Qubit Clifford Gates** | After preparing each qubit in the ground state through feedback cooling, we apply each two-qubit Clifford gate and test the fidelity to the expected state. States are estimated from acquired data by maximum likelihood estimation.

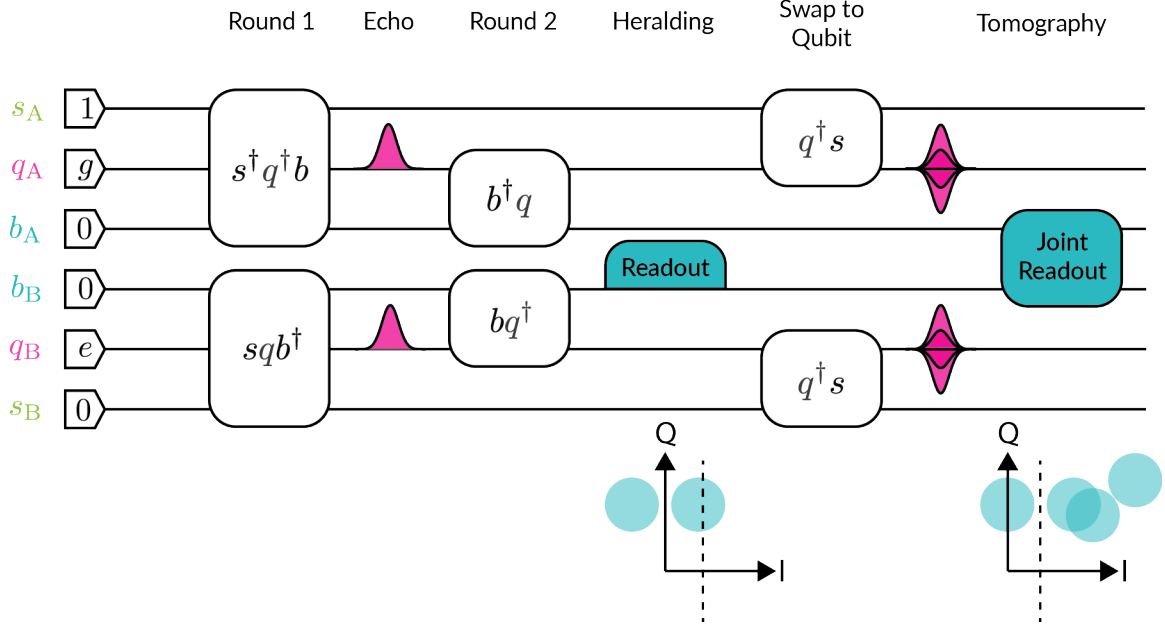


Figure 5.5: **Entanglement verification protocol** | We show the detailed experimental pulse sequence for the verification of photon loss robust remote entanglement through our time-bin protocol. Alice and Bob qubit and storage modes are first prepared in the ground state through feedback cooling. We then apply drives activating the $s^\dagger q^\dagger b + \text{h.c.}$ processes on Alice and Bob. Photon number unselective π pulses are then applied to Alice and Bob qubits to implement an echo, making the protocol insensitive to low frequency fluctuations in the qubit ω_{ge} transition energy. Next, drives activate the $q^\dagger b + \text{h.c.}$ ensure one photon in total is sent. We next read out only on the Bob qubit mode to herald the successful entanglement of the Alice storage and Bob storage modes. Finally, drives activate the $q^\dagger s + \text{h.c.}$ SWAPing the entanglement from storage modes to qubit modes, where we apply two-qubit tomography to characterize the generated entanglement.

data corresponding to two-qubit rotation is fed through our maximum likelihood estimation procedure, and the resultant density matrix is compared to the density matrix expected for ideal rotations and state preparation. Fidelity generally better than 98% assures that both our qubit rotations and state estimation procedure are well calibrated.

5.3.5 Entanglement verification protocol: Experimental results

Now that we trust our qubit tomography, we may now run the full time-bin entanglement protocol on our system. The detailed series of gates we apply in experiment is shown in Fig. 5.5. The experiment is repeated over 137,000 times, with 36 rotations per instance of the experiment for a total of 4.9 million measurement outcomes. We compare reconstructed density matrices to data simulated using the master equation outlined in Ch.

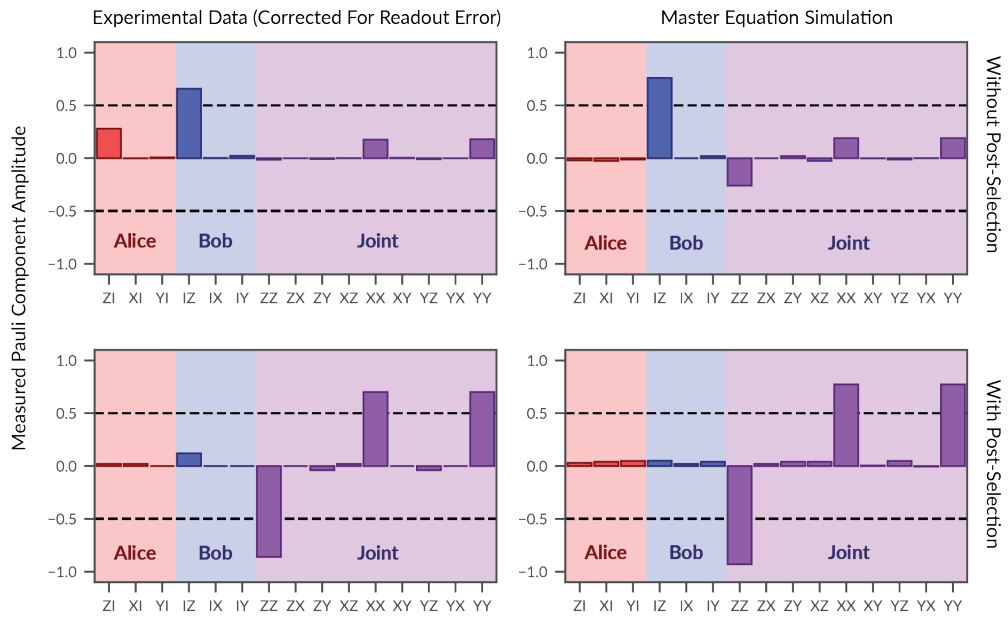


Figure 5.6: **State tomography of heralded and unheralded protocol** | Full state tomography of Alice and Bob qubits after the experimental protocol (left), as well as the results of a master equation simulation (right). Density matrix reconstruction yields a sampling error of 1% on each Pauli component. Upper panels correspond to the measured and simulated state without post-selecting on photon loss, and demonstrate poor coherence. Lower panels correspond to post-selecting for no photon loss, and yield demonstrably higher coherence. The depicted state has a concurrence of $68\% \pm 2\%$.

4.3, with parameters identical to those used in the simulation of the capture and release processes in isolation in Ch. 4.5. We find an ultimate success probability (before adjusting for post-selection readout contrast) of 27%, which compares favorably to the simulated success probability of 23%. To characterize the amount of generated entanglement, we use the measure of concurrence [63], an entanglement monotone. For states generated by the experiment in the absence of post-selection on Bob being in the entangled state, we find no concurrence whatsoever. While the channel has a quantum efficiency supporting entanglement through single-round protocols [21, 22, 23, 24], we trade success probability for enhanced entangled state fidelity through aggressive pulse truncation, resulting in poor correlations without postselection.

When post-selection is enabled, however, we find an entangled state concurrence between Alice and Bob qubits of $68\% \pm 2\%$. Master equation simulations attribute 17% of this to decoherence and decay during the time-bin entanglement protocol. We attribute an additional 5% of this to the T_{2R} times of the qubits, causing dephasing during the qubit-storage **SWAP** process. We attribute 1.7% of the error budget to decay processes during the qubit-storage **SWAP** process, and finally we attribute the 0.1% postselection error to 0.2% of the total error budget. Ultimately our model accounts for a total of 24% of the lost concurrence, leaving a remaining 8% unexplained. Potential experiments to find the origin of this 8% are: unselectivity of π pulses, interactions between simultaneously applied parametric pumps, and transient effects from the pulse edges.

Chapter 6

Perspectives of This Work Towards Future Entanglement Experiments

In conclusion, we entangled two distant circuit QED systems in a manner robust to photon loss using time-binning. We explored the design and characterization of a quantum processing module capable of running this type of entanglement experiment. This exploration involved controlling the parametric processes required for the release and capture of microwave photons from and to these modules. We then implemented a pitch-and-catch protocol that utilized these processes to remotely entangle the modules, devoting the redundant time-bin information to reject entanglement attempts in which the pitched photon was lost, and finally characterized the generated entangled state. We found that the entangled state was predominantly limited by the coherence times of the qubits, and not the losses of the lines.

In this chapter, we explore some potential directions for future entanglement experiments. Our exploration targets two potential directions. We first propose incremental improvements to the experiment performed in this dissertation in the interest of improving the entangled state fidelity. Next, we propose more complex experiments with an eye towards scalability.

6.1 Incremental improvements of the experiment

The principle contributor to entangled state infidelity in this experiment was qubit decoherence induced by the drives, prompting us to ask how to increase the ratio of the coherence times during the gates to the speed of the gates. Transmon decoherence under the presence of a strong drive is still an active area of research. The work of Sank et al. [64] and Venkatraman, Xiao et al. (in preparation), points to non-RWA terms in the Hamiltonian, dynamical instabilities of the of qubit-cavity system. These instabilities are dependent upon controllable design parameters of the system. We might use the techniques developed in these analyses to optimize the frequency layout and dispersive couplings of future quantum processing module designs.

Alternatively, we may select a qubit which will better maintain coherence in the presence of strong drives. The inductively shunted transmon, also proposed in the works by Verney et al. [65] and Venkatraman, Xiao et. al., has been demonstrated to remain more stable than similar transmons in the presence of strong pumps, potentially providing larger interaction strengths with less induced decoherence.

We additionally suggest that experiments which obviate the circulator may be of interest. The ferrite-based circulators used in our experiment are large, lossy, and incompatible with superconducting circuitry due to their large magnetic fields. Schemes using delay lines [55] may be useful if gate times are improved to be compatible with this architecture (Ch. 4.2.1.) Such schemes additionally have the benefit of having no preferred direction of travel for flying qubits, providing bidirectional information transfer, and potentially simplifying the design of the router in a modular architecture.

6.2 Scaling time-bin entanglement

With a working photon-loss robust remote-entanglement scheme demonstrated between two nodes, a next logical step is to demonstrate the scheme between n quantum processing modules in a scheme similar to that pictured in Fig. 1.1. With a handful of experiments demonstrating building blocks useful for a quantum router [66, 67, 68], we believe a practical router between multiple quantum processing modules is a realistic near-term prospect. The

demonstration of robust remote entanglement through such a router would be a the next important milestone towards the implementation of a modular quantum computer.

We also point towards work tackling the scalability of individual quantum processing modules. The MMIQC architecture introduced in Brecht et al. [69] integrates qubits, long lived cavities, amplifiers, and wiring on micromachined silicon wafers. All facilities provided by our quantum processing module may be integrated on a small subsection of a wafer, at a fraction of the size of our module. Shrinking the volume of quantum processing modules is of considerable interest for a modular quantum computer involving the thousands of modules required for the thousands of logical qubits needed to gain a significant computational advantage over classical computers. While the prospect of scaling the number of qubits by three orders of magnitude is a seemingly monumental task, we imagine the inventors of the point-contact transistor would have been awestruck by the integration of billions of transistors on a single chip to form a modern central processing unit. We believe similar engineering efforts applied to quantum processing modules could yield similar payoffs.

Appendix A

Wiring of the Experimental Setup

This chapter describes the wiring of the experimental setup

A.1 First-round drives

We create the three mode drive tones by mixing the all associated RF sources together through the use of a pair of mixers, as shown in Fig. A.2. To be on resonance, we require that the pump frequency satisfy

$$\omega_3 = \omega_q + \omega_b - \omega_s.$$

To generate this tone in a phase-coherent manner, we first begin by mixing the ω_b and ω_s . As these two tones are relatively close in frequency (638 MHz for Alice and 759 MHz for Bob), generating this difference frequency is accomplished using a mixer and low pass filter. This tone is then mixed with ω_b , and then filtered using microwave cavity band-pass filters to generate ω_3 . Amplitude and phase modulation of ω_3 to form control tones is accomplished using an *IQ* mixer with dedicated DAC channels.

A.2 Second-round drives

Activation of the $\mathbf{q}^\dagger \mathbf{b} + \text{h.c.}$ processes for the coherent transfer of a photon from the Alice module to Bob requires a total of three tones, either two qubit sideband tones and a shared

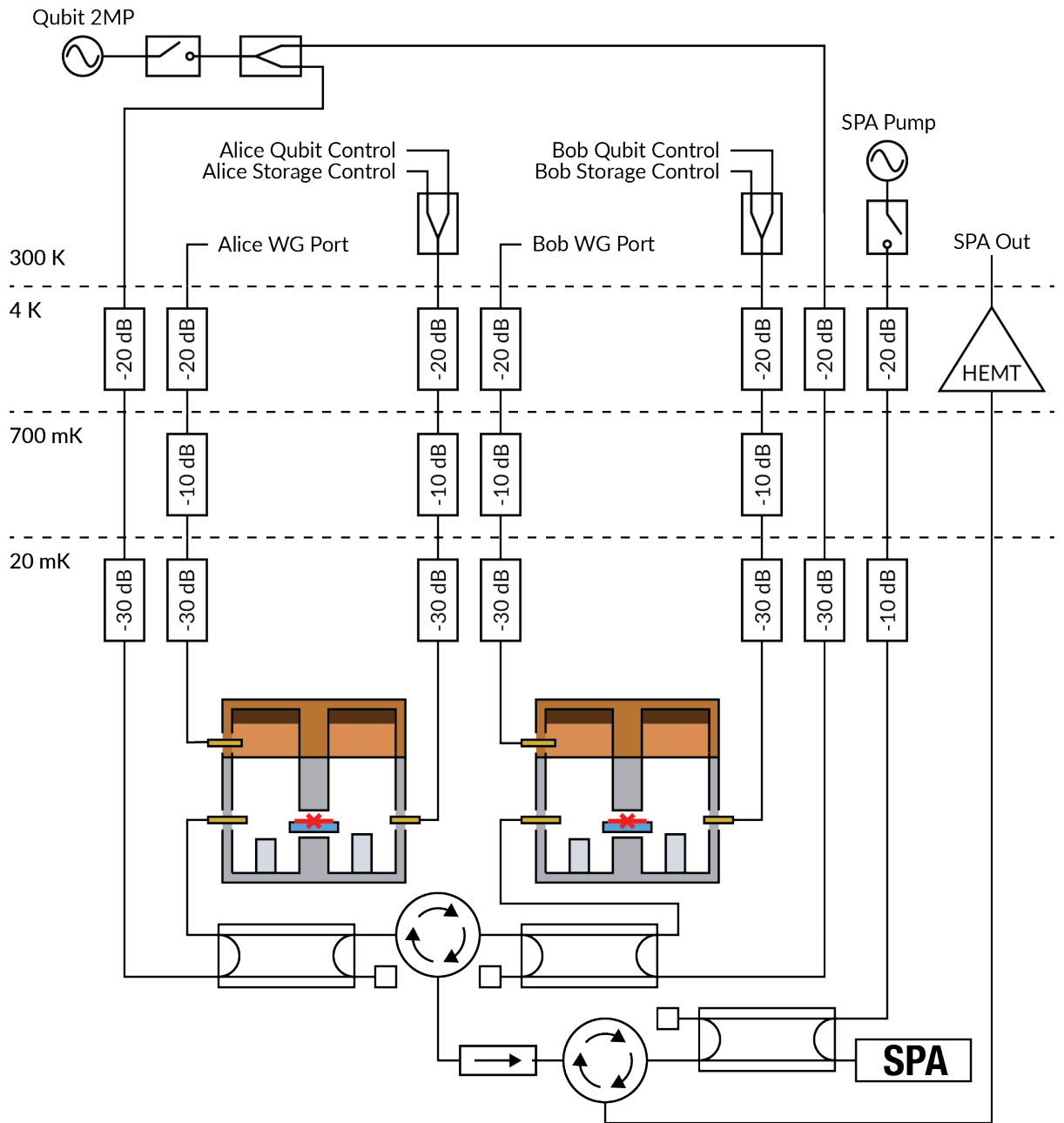


Figure A.1: **Dilution refrigerator wiring** | System block diagram for the cold portion of the experiment. Alice and Bob compute modules, and associated circulators, isolators, and directional couplers were cooled on the base stage (< 50 mK) of a dilution refrigerator. Input lines carrying signals to the system were attenuated and filtered using commercial low-pass filters and homemade lossy Eccosorb filters.

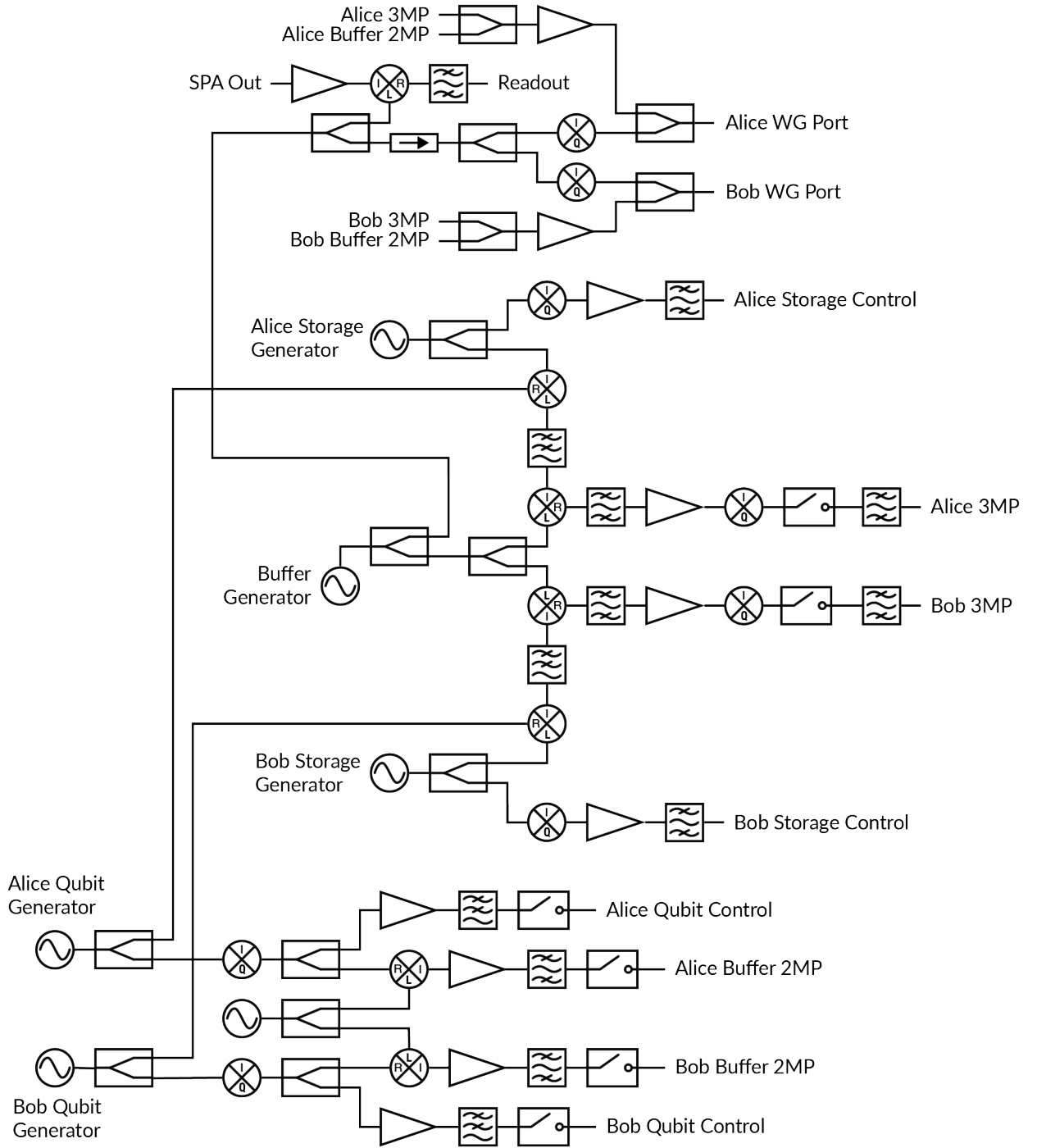


Figure A.2: **System block diagram for pump generation** | Microwave signal generators provide tones for readout, storage mode control, and qubit control. These same microwave signal generators are mixed in such a way to generate the necessary tones to activate necessary parametric processes. We introduce an additional shim generator to upconvert signals from the qubit control chain to be used as cavity sideband drive tones for the $\mathbf{q}^\dagger\mathbf{b}$ process.

cavity sideband tone, or two cavity sideband tones and a shared qubit sideband tone. Due to the lack of a weakly coupled port on our quantum processing module, the only way to deliver pumps in a way that minimizes leakage is to deliver them through the waveguide port, which has the requirement that drives delivered through the port be above 8.5 GHz. Instead, we deliver the qubit sideband tones through the strongly coupled port, and suppose that the tone *will* leak. This is not at all an issue if there is only one qubit sideband tone, shared between Alice and Bob. By injecting the drive through multiple ports and adjusting frequency, amplitude, and phase (adjustment components not pictured in Fig.), multipath interference provides a mechanism for balancing the drive strength between both modules.

The cavity sideband pulses are generated through upconversion of the qubit pulses themselves, as shown in Fig. A.2. This dual upconversion process provides a way to economize on DAC channels, as qubit control pulses and drive tones will never be played simultaneously. Playing strong pumps near the readout mode is a tricky affair. If one is to tune the pump close to the buffer cavity, it becomes difficult to filter the noise from high power amplifiers to ensure that the amplifier noise does not populate the buffer cavity. This dual upconversion assists in the production of pumps with large detunings from their addressed mode, as the DAC on our FPGA is limited to a maximum sideband detuning of 150 MHz. Here, a shim generator at ω_{shim} is used as the local oscillator signal to upconvert Alice and Bob qubit control tones at ω_q . A band-pass filter selects the lower sideband from control tones at ω_q and ω_{shim} , resulting in drive tones at

$$\omega_1^A = \omega_{\text{shim}} - \omega_q^A; \omega_1^B = \omega_{\text{shim}} - \omega_q^B.$$

Successful transfer requires that $(\omega_1^A - \omega_2^A) - (\omega_1^B - \omega_2^B) = \omega_q^A - \omega_q^B$, or that the energy provided by the combination of the two pumps on Alice and Bob corresponds to the frequency difference between Alice and Bob. Given that we've picked $\omega_2^A = \omega_2^B$, we find that both ω_2 and ω_{shim} cancel. To ensure the photon is ejected at the buffer mode frequency, we must choose the ω_{shim} frequency such that

$$\omega_2 - \omega_1 = \omega_2 - \omega_{\text{shim}} + \omega_q = \omega_q - \omega_b \implies \omega_{\text{shim}} - \omega_2 = \omega_b.$$

In practice, we choose $\omega_2 = 2\pi \cdot 6.5 \text{ GHz}$.

Appendix B

Exact Pitch-Catch Solution for the Envelope

We start with the equations of motion coupling the buffer and qubit mode to a transmission line Eq. 4.24-4.26

$$\begin{aligned}\dot{b} &= -i\delta b - ig^*(t)q - \frac{\kappa}{2}b - \sqrt{\kappa}b_{\text{in}} \\ \dot{q} &= -ig(t)b \\ \sqrt{\kappa}b &= b_{\text{out}} - b_{\text{in}}.\end{aligned}$$

We will analytically solve for a full release of a flying photon on resonance with the buffer mode. Equivalent capture dynamics may be solved for by time reversal by arguments in Ch. 4.4. Setting $\delta = 0$ and $b_{\text{in}} = 0$, and setting $g(t) \rightarrow -ig(t)$ we obtain the following equations

$$\begin{aligned}\dot{b} &= g(t)q - \frac{\kappa}{2}b \\ \dot{q} &= -g(t)b.\end{aligned}$$

We suppose that we want to release a traveling pulse with the envelope $b_{\text{out}} = \frac{a}{\sqrt{\kappa}} \text{sech}(\beta t)$. Through input-output relations, $b = \alpha \text{sech}(\beta t)$. Plugging in, we get

$$\begin{aligned}\dot{q}(t) &= -\alpha g(t) \text{sech}(\beta t) \\ -\alpha\beta \text{sech}(\beta t) \tanh(\beta t) &= g(t) q(t) - \frac{\kappa\alpha}{2} \text{sech}(\beta t).\end{aligned}$$

Rearranging the second line to solve for $q(t)$ we get

$$q(t) = -\frac{\alpha \text{sech}(\beta t)}{2g(t)} (2\beta \tanh(\beta t) - \kappa).$$

We differentiate this to get

$$\dot{q}(t) = \frac{\alpha \text{sech}(\beta t)}{2g^2(t)} [\beta g(t) (2\beta - 4\beta \text{sech}^2(\beta t) - \kappa \tanh(\beta t)) + \dot{g}(t) (2\beta \tanh(\beta t) - \kappa)].$$

Combining this with the first equation of motion,

$$2g^3(t) + \alpha\beta g(t) (2\beta - 4\beta \text{sech}^2(\beta t) - \kappa \tanh(\beta t)) + \alpha\dot{g}(t) (2\beta \tanh(\beta t) - \kappa) = 0$$

This equation is of the form

$$g'(t) + A(t)g(t) + B(t)g^3(t) = 0.$$

This is a Bernoulli equation with $n = 3$, so substituting $u = g^{-2}$ will linearize it to

$$\dot{u}(t) - 2B(t) - 2A(t)u(t) = 0,$$

which can be solved with integrating factors. Putting this all together, we obtain the solution

$$g(t) = \pm \frac{\sqrt{\beta} (2\beta \sinh(\beta t) - \kappa \cosh(\beta t))}{\cosh(\beta t) \sqrt{\beta c_1 \cosh(\beta t)^2 - 4\beta - 2\kappa \sinh(2\beta t)}}.$$

with the undetermined coefficient c_1 . Note that the amplitude of the flying pulse α appears nowhere in this expression. To obtain the population as a function of time, plug in to our second equation to obtain

$$q(t) = -\frac{\alpha \operatorname{sech}(\beta t)}{\sqrt{8\beta}} \sqrt{\beta(c_1 + c_1 \cosh(2t\beta) - 8) - 4\kappa \sinh(2\beta t)}.$$

Now we can fix our unknown coefficient. Taking limits of $q(t)$, we obtain

$$\lim_{t \rightarrow \pm\infty} q(t) = -\frac{\alpha}{2} \sqrt{c_1 \mp \frac{4\kappa}{\beta}}.$$

Setting $c_1 = 4\kappa_{\text{Out}}/\beta + \epsilon$, with $|\epsilon| \ll 4\kappa_{\text{Out}}/\beta$, added to regularize a divergence, we get

$$\sqrt{n_{\text{initial}}} = \lim_{t \rightarrow -\infty} q(t) = -\frac{\alpha}{2} \sqrt{\frac{8\kappa}{\beta} + \epsilon} \approx -\frac{\alpha}{2} \sqrt{\frac{8\kappa}{\beta}}$$

$$\sqrt{n_{\text{final}}} = \lim_{t \rightarrow \infty} q(t) = -\frac{\alpha}{2} \sqrt{\epsilon},$$

or,

$$\alpha = -\sqrt{\frac{\beta n_{\text{initial}}}{2\kappa}}$$

$$\epsilon = \frac{8\kappa}{\beta} \sqrt{\frac{n_{\text{final}}}{n_{\text{initial}}}}$$

$$c_1 = \frac{4\kappa}{\beta} \left(1 + 2\sqrt{\frac{n_{\text{final}}}{n_{\text{initial}}}} \right).$$

If we want to pitch as completely as possible, we want to minimize the final population of the q mode, ideally forcing it to zero. However, looking at the first equation of motion, we notice that the rate at which photons leave the a mode is proportional to both the modulated coupling and the b mode population. As the tail of the flying pulse leaves the cavity, the b mode population will drop, by our choice, exponentially. This requires that the control pulse never reach zero, to allow the b mode population to reach zero at $t \rightarrow \infty$. In the original

work by Cirac et al. [21], the control pulse is left on indefinitely, corresponding to $\eta = 0$ and a constant g , and thus exponential decay. The exponential tail of the wavepacket and natural exponential decay of the cavity should make this a logarithmic divergence in time. We can regularize this divergence by choosing $a(+\infty)$ nonzero but small as a compromise. As a sanity check, we can integrate the flying field $\sqrt{\kappa}q(t)$ to check its energy content

$$\int \left| \sqrt{\frac{\beta n_{\text{initial}}}{2}} \operatorname{sech}(\beta t) \right|^2 dt = n_{\text{Initial}},$$

as desired. Our final control pulse, source mode field, and flying field are given by

$$g(t) = \frac{\sqrt{\beta} (2\beta \sinh(\beta t) - \kappa \cosh(\beta t))}{\cosh(\beta t) \sqrt{4\kappa_{\text{Out}} \left(1 + 2\sqrt{\frac{n_{\text{final}}}{n_{\text{initial}}}}\right) \cosh^2(\beta t) - 4\beta - 2\kappa \sinh(2\beta t)}}.$$

$$q(t) = \frac{1}{2} \sqrt{\frac{n_{\text{Initial}}}{\kappa}} \operatorname{sech}(\beta t) \sqrt{2\kappa \left(1 + 2\sqrt{\frac{n_{\text{final}}}{n_{\text{initial}}}}\right) \cosh^2(\beta t) - \kappa \sinh(2\beta t) - 2\beta}$$

$$b_{\text{out}} = \sqrt{\kappa} b(t) = -\sqrt{\frac{\beta n_{\text{initial}}}{2}} \operatorname{sech}(\beta t)$$

Noticing that t is always contained in a trig function, we suspect there's a way to transform time where these equations simplify somewhat. Substitute $t \rightarrow \beta^{-1} \operatorname{arctanh}(x)$. We then obtain

$$g(x) = \frac{\sqrt{\beta} (2x\beta - \kappa)}{2\sqrt{\frac{\kappa(x-1-2\delta)}{x^2-1}} - \beta}$$

Where $\sqrt{\frac{n_{\text{Final}}}{n_{\text{Initial}}}} = \delta$. Immediately we see that there's a zero in this function at $x = \kappa/2\beta$. Since $-1 < x < 1$, we need that $\kappa/2\beta \geq 1$ so $g(x)$ is strictly positive, or

$$\kappa \geq 2\beta$$

Bibliography

- [1] LM741 Operational Amplifier. Technical report, October 2015. 1
- [2] Liang Jiang, Jacob M. Taylor, Anders S. Sørensen, and Mikhail D. Lukin. Distributed quantum computation based on small quantum registers. *Physical Review A*, 76(6):062323, December 2007. ISSN 1050-2947, 1094-1622. doi: 10.1103/PhysRevA.76.062323. 2
- [3] C. Monroe, R. Raussendorf, A. Ruthven, K. R. Brown, P. Maunz, L.-M. Duan, and J. Kim. Large-scale modular quantum-computer architecture with atomic memory and photonic interconnects. *Physical Review A*, 89(2):022317, February 2014. ISSN 1050-2947, 1094-1622. doi: 10.1103/PhysRevA.89.022317. 2
- [4] Peter W. Shor. Scheme for reducing decoherence in quantum computer memory. *Physical Review A*, 52(4):R2493–R2496, October 1995. ISSN 1050-2947, 1094-1622. doi: 10.1103/PhysRevA.52.R2493. 2
- [5] J. Brendel, N. Gisin, W. Tittel, and H. Zbinden. Pulsed Energy-Time Entangled Twin-Photon Source for Quantum Communication. *Physical Review Letters*, 82(12):2594–2597, March 1999. ISSN 0031-9007, 1079-7114. doi: 10.1103/PhysRevLett.82.2594. 3, 6, 70
- [6] I. Marcikic, H. de Riedmatten, W. Tittel, H. Zbinden, M. Legré, and N. Gisin. Distribution of Time-Bin Entangled Qubits over 50 km of Optical Fiber. *Physical Review Letters*, 93(18):180502, October 2004. ISSN 0031-9007, 1079-7114. doi: 10.1103/PhysRevLett.93.180502. 3, 6, 70

- [7] B. Brecht, Dileep V. Reddy, C. Silberhorn, and M. G. Raymer. Photon Temporal Modes: A Complete Framework for Quantum Information Science. *Physical Review X*, 5(4):041017, October 2015. ISSN 2160-3308. doi: 10.1103/PhysRevX.5.041017. 3, 6, 70
- [8] Nissim Ofek, Andrei Petrenko, Reinier Heeres, Philip Reinhold, Zaki Leghtas, Brian Vlastakis, Yehan Liu, Luigi Frunzio, S. M. Girvin, L. Jiang, Mazyar Mirrahimi, M. H. Devoret, and R. J. Schoelkopf. Extending the lifetime of a quantum bit with error correction in superconducting circuits. *Nature*, 536(7617):441–445, August 2016. ISSN 0028-0836, 1476-4687. doi: 10.1038/nature18949. 3
- [9] Uri Vool. *Engineering Synthetic Quantum Operations*. PhD thesis, 2017. 4
- [10] A. A. Houck, J. A. Schreier, B. R. Johnson, J. M. Chow, Jens Koch, J. M. Gambetta, D. I. Schuster, L. Frunzio, M. H. Devoret, S. M. Girvin, and R. J. Schoelkopf. Controlling the Spontaneous Emission of a Superconducting Transmon Qubit. *Physical Review Letters*, 101(8):080502, August 2008. ISSN 0031-9007, 1079-7114. doi: 10.1103/PhysRevLett.101.080502. 3, 13
- [11] R. Miller, T E Northup, K M Birnbaum, A Boca, A D Boozer, and H J Kimble. Trapped atoms in cavity QED: Coupling quantized light and matter. *Journal of Physics B: Atomic, Molecular and Optical Physics*, 38(9):S551–S565, May 2005. ISSN 0953-4075, 1361-6455. doi: 10.1088/0953-4075/38/9/007. 3
- [12] S. Haroche and J.-M. Raimond. *Exploring the Quantum: Atoms, Cavities and Photons*. Oxford Graduate Texts. Oxford University Press, Oxford ; New York, 2006. ISBN 978-0-19-850914-1. OCLC: ocm68770236. 3, 39
- [13] Alexandre Blais, Ren-Shou Huang, Andreas Wallraff, S. M. Girvin, and R. J. Schoelkopf. Cavity quantum electrodynamics for superconducting electrical circuits: An architecture for quantum computation. *Physical Review A*, 69(6):062320, June 2004. ISSN 1050-2947, 1094-1622. doi: 10.1103/PhysRevA.69.062320. 4, 12, 13
- [14] Jens Koch, Terri M. Yu, Jay Gambetta, A. A. Houck, D. I. Schuster, J. Majer, Alexan-

- dre Blais, M. H. Devoret, S. M. Girvin, and R. J. Schoelkopf. Charge-insensitive qubit design derived from the Cooper pair box. *Physical Review A*, 76(4):042319, October 2007. ISSN 1050-2947, 1094-1622. doi: 10.1103/PhysRevA.76.042319. 4, 11
- [15] J. Q. You, Xuedong Hu, S. Ashhab, and Franco Nori. Low-decoherence flux qubit. *Physical Review B*, 75(14):140515, April 2007. ISSN 1098-0121, 1550-235X. doi: 10.1103/PhysRevB.75.140515. 4
- [16] V. E. Manucharyan, J. Koch, L. I. Glazman, and M. H. Devoret. Fluxonium: Single Cooper-Pair Circuit Free of Charge Offsets. *Science*, 326(5949):113–116, October 2009. ISSN 0036-8075, 1095-9203. doi: 10.1126/science.1175552. 4
- [17] R. Vijay, D. H. Slichter, and I. Siddiqi. Observation of Quantum Jumps in a Superconducting Artificial Atom. *Physical Review Letters*, 106(11):110502, March 2011. ISSN 0031-9007, 1079-7114. doi: 10.1103/PhysRevLett.106.110502. 4
- [18] William F. Kindel, M. D. Schroer, and K. W. Lehnert. Generation and efficient measurement of single photons from fixed-frequency superconducting qubits. *Physical Review A*, 93(3):033817, March 2016. ISSN 2469-9926, 2469-9934. doi: 10.1103/PhysRevA.93.033817. 4
- [19] Z. Leghtas, S. Touzard, I. M. Pop, A. Kou, B. Vlastakis, A. Petrenko, K. M. Sliwa, A. Narla, S. Shankar, M. J. Hatridge, M. Reagor, L. Frunzio, R. J. Schoelkopf, M. Mirrahimi, and M. H. Devoret. Confining the state of light to a quantum manifold by engineered two-photon loss. *Science*, 347(6224):853–857, February 2015. ISSN 0036-8075, 1095-9203. doi: 10.1126/science.aaa2085. 4, 18
- [20] Raphaël Lescanne, Samuel Deléglise, Emanuele Albertinale, Ulysse Réglade, Thibault Capelle, Edouard Ivanov, Thibaut Jacqmin, Zaki Leghtas, and Emmanuel Flurin. Detecting itinerant microwave photons with engineered non-linear dissipation. *arXiv:1902.05102 [cond-mat, physics:quant-ph]*, February 2019. 4, 20
- [21] J. I. Cirac, P. Zoller, H. J. Kimble, and H. Mabuchi. Quantum State Transfer and Entanglement Distribution among Distant Nodes in a Quantum Network. *Physical*

- Review Letters*, 78(16):3221–3224, April 1997. ISSN 0031-9007, 1079-7114. doi: 10.1103/PhysRevLett.78.3221. 5, 55, 65, 88, 100
- [22] P. Kurpiers, P. Magnard, T. Walter, B. Royer, M. Pechal, J. Heinsoo, Y. Salathé, A. Akin, S. Storz, J.-C. Besse, S. Gasparinetti, A. Blais, and A. Wallraff. Deterministic quantum state transfer and remote entanglement using microwave photons. *Nature*, 558(7709):264–267, June 2018. ISSN 0028-0836, 1476-4687. doi: 10.1038/s41586-018-0195-y. 5, 55, 88
- [23] Christopher J. Axline, Luke D. Burkhardt, Wolfgang Pfaff, Mengzhen Zhang, Kevin Chou, Philippe Campagne-Ibarcq, Philip Reinhold, Luigi Frunzio, S. M. Girvin, Liang Jiang, M. H. Devoret, and R. J. Schoelkopf. On-demand quantum state transfer and entanglement between remote microwave cavity memories. *Nature Physics*, 14(7):705–710, July 2018. ISSN 1745-2473, 1745-2481. doi: 10.1038/s41567-018-0115-y. 5, 55, 88
- [24] P. Campagne-Ibarcq, E. Zalys-Geller, A. Narla, S. Shankar, P. Reinhold, L. Burkhardt, C. Axline, W. Pfaff, L. Frunzio, R. J. Schoelkopf, and M. H. Devoret. Deterministic Remote Entanglement of Superconducting Circuits through Microwave Two-Photon Transitions. *Physical Review Letters*, 120(20):200501, May 2018. ISSN 0031-9007, 1079-7114. doi: 10.1103/PhysRevLett.120.200501. 5, 17, 19, 44, 46, 55, 64, 88
- [25] Gregor Weihs, Tobias Huber, and Ana Predojević. Time-bin Entanglement from Quantum Dots. *arXiv:1609.02754 [cond-mat, physics:physics, physics:quant-ph]*, September 2016. 5, 6
- [26] Michael Tinkham. *Introduction to Superconductivity*. Dover Books on Physics. Dover Publ, Mineola, NY, 2. ed edition, 2004. ISBN 978-0-486-43503-9. OCLC: 728146785. 9
- [27] M. H. Devoret, A. Wallraff, and J. M. Martinis. Superconducting Qubits: A Short Review. *arXiv:cond-mat/0411174*, November 2004. 9, 12

- [28] B.D. Josephson. Possible new effects in superconductive tunnelling. *Physics Letters*, 1(7):251–253, July 1962. ISSN 00319163. doi: 10.1016/0031-9163(62)91369-0. 9
- [29] Antonio Barone and Gianfranco Paternò. *Physics and Applications of the Josephson Effect*. Wiley, New York, 1982. ISBN 978-0-471-01469-0. 10
- [30] Theodore Van Duzer and Charles W. Turner. *Principles of Superconductive Devices and Circuits*. Arnold, London, 1981. ISBN 978-0-7131-3432-2. OCLC: 16541086. 10
- [31] Michel H. Devoret, Benjamin Huard, Robert Schoelkopf, and L. F. Cugliandolo, editors. *Quantum Machines: Measurement and Control of Engineered Quantum Systems*. Oxford University Press, Oxford, United Kingdom, first edition edition, 2014. ISBN 978-0-19-968118-1. OCLC: ocn876285697. 10, 11
- [32] Ramamurti Shankar. *Principles of Quantum Mechanics*. Plenum Press, New York, 2nd ed edition, 1994. ISBN 978-0-306-44790-7. 12
- [33] C. W. Gardiner and P. Zoller. *Quantum Noise: A Handbook of Markovian and Non-Markovian Quantum Stochastic Methods with Applications to Quantum Optics*. Springer Series in Synergetics. Springer, Berlin ; New York, 3rd ed edition, 2004. ISBN 978-3-540-22301-6. 13, 59, 60
- [34] Jay Gambetta, Alexandre Blais, M. Boissonneault, A. A. Houck, D. I. Schuster, and S. M. Girvin. Quantum trajectory approach to circuit QED: Quantum jumps and the Zeno effect. *Physical Review A*, 77(1):012112, January 2008. ISSN 1050-2947, 1094-1622. doi: 10.1103/PhysRevA.77.012112. 14
- [35] Alexander N. Korotkov. Quantum Bayesian approach to circuit QED measurement with moderate bandwidth. *Physical Review A*, 94(4):042326, October 2016. ISSN 2469-9926, 2469-9934. doi: 10.1103/PhysRevA.94.042326. 15
- [36] M. Hatridge, S. Shankar, M. Mirrahimi, F. Schackert, K. Geerlings, T. Brecht, K. M. Sliwa, B. Abdo, L. Frunzio, S. M. Girvin, R. J. Schoelkopf, and M. H. Devoret. Quantum Back-Action of an Individual Variable-Strength Measurement. *Science*, 339

- (6116):178–181, January 2013. ISSN 0036-8075, 1095-9203. doi: 10.1126/science.1226897. 15
- [37] K. W. Murch, S. J. Weber, C. Macklin, and I. Siddiqi. Observing single quantum trajectories of a superconducting quantum bit. *Nature*, 502(7470):211–214, October 2013. ISSN 0028-0836, 1476-4687. doi: 10.1038/nature12539. 15
- [38] Matthew Reagor, Wolfgang Pfaff, Christopher Axline, Reinier W. Heeres, Nissim Ofek, Katrina Sliwa, Eric Holland, Chen Wang, Jacob Blumoff, Kevin Chou, Michael J. Hatridge, Luigi Frunzio, Michel H. Devoret, Liang Jiang, and Robert J. Schoelkopf. Quantum memory with millisecond coherence in circuit QED. *Physical Review B*, 94(1):014506, July 2016. ISSN 2469-9950, 2469-9969. doi: 10.1103/PhysRevB.94.014506. 15, 25
- [39] William F. Kindel, M. D. Schroer, and K. W. Lehnert. Generation and efficient measurement of single photons from fixed-frequency superconducting qubits. *Physical Review A*, 93(3):033817, March 2016. ISSN 2469-9926, 2469-9934. doi: 10.1103/PhysRevA.93.033817. 16
- [40] Simon E. Nigg, Hanhee Paik, Brian Vlastakis, Gerhard Kirchmair, S. Shankar, Luigi Frunzio, M. H. Devoret, R. J. Schoelkopf, and S. M. Girvin. Black-Box Superconducting Circuit Quantization. *Physical Review Letters*, 108(24):240502, June 2012. ISSN 0031-9007, 1079-7114. doi: 10.1103/PhysRevLett.108.240502. 17, 27
- [41] H. Padamsee. Design Topics for Superconducting RF Cavities and Ancillaries. *arXiv:1501.07129 [physics]*. doi: 10.5170/CERN-2014-005.141. 23
- [42] Christopher Axline. *Building Blocks for Modular Circuit QED Quantum Computing*. PhD thesis, 2018. 25
- [43] Teresa Brecht. *Micromachined Quantum Circuits*. PhD thesis, 2017. 25
- [44] Z. Wang, S. Shankar, Z.K. Mineev, P. Campagne-Ibarcq, A. Narla, and M.H. Devoret. Cavity Attenuators for Superconducting Qubits. *Physical Review Applied*, 11

(1):014031, January 2019. ISSN 2331-7019. doi: 10.1103/PhysRevApplied.11.014031.

26

- [45] Florent Lecocq, Ioan M Pop, Zhihui Peng, Iulian Matei, Thierry Crozes, Thierry Fournier, Cécile Naud, Wiebke Guichard, and Olivier Buisson. Junction fabrication by shadow evaporation without a suspended bridge. *Nanotechnology*, 22(31):315302, August 2011. ISSN 0957-4484, 1361-6528. doi: 10.1088/0957-4484/22/31/315302. 27
- [46] Matthew Reed. *Entanglement and Quantum Error Correction with Superconducting Qubits*. PhD thesis, 2013. 29
- [47] Kevin Chou. *Teleported Operations between Logical Qubits in Circuit Quantum Electrodynamics*. PhD thesis, 2018. 31
- [48] Bernard Yurke and David Stoler. Bell’s-inequality experiments using independent-particle sources. *Physical Review A*, 46(5):2229–2234, September 1992. ISSN 1050-2947, 1094-1622. doi: 10.1103/PhysRevA.46.2229. 53
- [49] Sean D. Barrett and Pieter Kok. Efficient high-fidelity quantum computation using matter qubits and linear optics. *Physical Review A*, 71(6):060310, June 2005. ISSN 1050-2947, 1094-1622. doi: 10.1103/PhysRevA.71.060310. 53
- [50] B. Hensen, H. Bernien, A. E. Dréau, A. Reiserer, N. Kalb, M. S. Blok, J. Ruitenber, R. F. L. Vermeulen, R. N. Schouten, C. Abellán, W. Amaya, V. Pruneri, M. W. Mitchell, M. Markham, D. J. Twitchen, D. Elkouss, S. Wehner, T. H. Taminiau, and R. Hanson. Loophole-free Bell inequality violation using electron spins separated by 1.3 kilometres. *Nature*, 526(7575):682–686, October 2015. ISSN 0028-0836, 1476-4687. doi: 10.1038/nature15759. 54
- [51] A. Narla, S. Shankar, M. Hatridge, Z. Leghtas, K. M. Sliwa, E. Zalys-Geller, S. O. Mundhada, W. Pfaff, L. Frunzio, R. J. Schoelkopf, and M. H. Devoret. Robust Concurrent Remote Entanglement Between Two Superconducting Qubits. *Physical Review X*, 6(3):031036, September 2016. ISSN 2160-3308. doi: 10.1103/PhysRevX.6.031036.

54

- [52] E. Zalys-Geller, A. Narla, S. Shankar, M. Hatridge, M. P. Silveri, K. Sliwa, Z. Leghtas, and M. H. Devoret. Generation of discord through a remote joint continuous variable measurement. *arXiv:1803.01275 [quant-ph]*, May 2018. 54
- [53] N. Roch, M. E. Schwartz, F. Motzoi, C. Macklin, R. Vijay, A. W. Eddins, A. N. Korotkov, K. B. Whaley, M. Sarovar, and I. Siddiqi. Observation of Measurement-Induced Entanglement and Quantum Trajectories of Remote Superconducting Qubits. *Physical Review Letters*, 112(17):170501, April 2014. ISSN 0031-9007, 1079-7114. doi: 10.1103/PhysRevLett.112.170501. 55, 64
- [54] Luke Burkhart. XXXX. 2020. 56
- [55] N. Leung, Y. Lu, S. Chakram, R. K. Naik, N. Earnest, R. Ma, K. Jacobs, A. N. Cleland, and D. I. Schuster. Deterministic bidirectional communication and remote entanglement generation between superconducting qubits. *npj Quantum Information*, 5(1):18, December 2019. ISSN 2056-6387. doi: 10.1038/s41534-019-0128-0. 56, 90
- [56] Y. P. Zhong, H.-S. Chang, K. J. Satzinger, M.-H. Chou, A. Bienfait, C. R. Conner, É. Dumur, J. Grebel, G. A. Peairs, R. G. Povey, D. I. Schuster, and A. N. Cleland. Violating Bell’s inequality with remotely connected superconducting qubits. *Nature Physics*, 15(8):741–744, August 2019. ISSN 1745-2473, 1745-2481. doi: 10.1038/s41567-019-0507-7. 56, 57
- [57] Joshua Combes, Joseph Kerckhoff, and Mohan Sarovar. The SLH framework for modeling quantum input-output networks. *Advances in Physics: X*, 2(3):784–888, May 2017. ISSN 2374-6149. doi: 10.1080/23746149.2017.1343097. 59
- [58] J.R. Johansson, P.D. Nation, and Franco Nori. QuTiP: An open-source Python framework for the dynamics of open quantum systems. *Computer Physics Communications*, 183(8):1760–1772, August 2012. ISSN 00104655. doi: 10.1016/j.cpc.2012.02.021. 61
- [59] J.R. Johansson, P.D. Nation, and Franco Nori. QuTiP 2: A Python framework for the dynamics of open quantum systems. *Computer Physics Communications*, 184(4): 1234–1240, April 2013. ISSN 00104655. doi: 10.1016/j.cpc.2012.11.019. 61

- [60] Alexander N. Korotkov. Flying microwave qubits with nearly perfect transfer efficiency. *Physical Review B*, 84(1):014510, July 2011. ISSN 1098-0121, 1550-235X. doi: 10.1103/PhysRevB.84.014510. 65
- [61] David M. Pozar. *Microwave Engineering*. Wiley, Hoboken, NJ, 4th ed edition, 2012. ISBN 978-0-470-63155-3. OCLC: ocn714728044. 75
- [62] K. Banaszek, G. M. D’Ariano, M. G. A. Paris, and M. F. Sacchi. Maximum-likelihood estimation of the density matrix. *Physical Review A*, 61(1):010304, December 1999. ISSN 1050-2947, 1094-1622. doi: 10.1103/PhysRevA.61.010304. 82, 84
- [63] Ryszard Horodecki, Paweł Horodecki, Michał Horodecki, and Karol Horodecki. Quantum entanglement. *Reviews of Modern Physics*, 81(2):865–942, June 2009. ISSN 0034-6861, 1539-0756. doi: 10.1103/RevModPhys.81.865. 88
- [64] Daniel Sank, Zijun Chen, Mostafa Khezri, J. Kelly, R. Barends, B. Campbell, Y. Chen, B. Chiaro, A. Dunsworth, A. Fowler, E. Jeffrey, E. Lucero, A. Megrant, J. Mutus, M. Neeley, C. Neill, P. J. J. O’Malley, C. Quintana, P. Roushan, A. Vainsencher, T. White, J. Wenner, Alexander N. Korotkov, and John M. Martinis. Measurement-Induced State Transitions in a Superconducting Qubit: Beyond the Rotating Wave Approximation. *Physical Review Letters*, 117(19):190503, November 2016. ISSN 0031-9007, 1079-7114. doi: 10.1103/PhysRevLett.117.190503. 90
- [65] Lucas Verney, Raphaël Lescanne, Michel H. Devoret, Zaki Leghtas, and Mazyar Mirrahimi. Structural instability of driven Josephson circuits prevented by an inductive shunt. *Physical Review Applied*, 11(2):024003, February 2019. ISSN 2331-7019. doi: 10.1103/PhysRevApplied.11.024003. 90
- [66] Benjamin J. Chapman, Bradley A. Moores, Eric I. Rosenthal, Joseph Kerckhoff, and K. W. Lehnert. General purpose multiplexing device for cryogenic microwave systems. *Applied Physics Letters*, 108(22):222602, May 2016. ISSN 0003-6951, 1077-3118. doi: 10.1063/1.4952772. 90
- [67] Joseph Kerckhoff, Kevin Lalumière, Benjamin J. Chapman, Alexandre Blais, and

- K. W. Lehnert. On-Chip Superconducting Microwave Circulator from Synthetic Rotation. *Physical Review Applied*, 4(3):034002, September 2015. ISSN 2331-7019. doi: 10.1103/PhysRevApplied.4.034002. 90
- [68] K. M. Sliwa, M. Hatridge, A. Narla, S. Shankar, L. Frunzio, R. J. Schoelkopf, and M. H. Devoret. Reconfigurable Josephson Circulator/Directional Amplifier. *Physical Review X*, 5(4):041020, November 2015. ISSN 2160-3308. doi: 10.1103/PhysRevX.5.041020. 90
- [69] Teresa Brecht, Wolfgang Pfaff, Chen Wang, Yiwen Chu, Luigi Frunzio, Michel H Devoret, and Robert J Schoelkopf. Multilayer microwave integrated quantum circuits for scalable quantum computing. *npj Quantum Information*, 2(1):16002, November 2016. ISSN 2056-6387. doi: 10.1038/npjqi.2016.2. 91
- [70] N. Roch, E. Flurin, F. Nguyen, P. Morfin, P. Campagne-Ibarcq, M. H. Devoret, and B. Huard. Widely Tunable, Nondegenerate Three-Wave Mixing Microwave Device Operating near the Quantum Limit. *Physical Review Letters*, 108(14):147701, April 2012. ISSN 0031-9007, 1079-7114. doi: 10.1103/PhysRevLett.108.147701.
- [71] Gabriel Molina-Terriza, Juan P. Torres, and Lluís Torner. Twisted photons. *Nature Physics*, 3(5):305–310, May 2007. ISSN 1745-2473, 1745-2481. doi: 10.1038/nphys607.
- [72] Srikanth J. Srinivasan, Neereja M. Sundaresan, Darius Sadri, Yanbing Liu, Jay M. Gambetta, Terri Yu, S. M. Girvin, and Andrew A. Houck. Time-reversal symmetrization of spontaneous emission for quantum state transfer. *Physical Review A*, 89(3):033857, March 2014. ISSN 1050-2947, 1094-1622. doi: 10.1103/PhysRevA.89.033857.
- [73] Matti Silveri, Evan Zalys-Geller, Michael Hatridge, Zaki Leghtas, Michel H. Devoret, and S. M. Girvin. Theory of remote entanglement via quantum-limited phase-preserving amplification. *Physical Review A*, 93(6):062310, June 2016. ISSN 2469-9926, 2469-9934. doi: 10.1103/PhysRevA.93.062310.
- [74] H. J. Kimble. The Quantum Internet. *Nature*, 453(7198):1023–1030, June 2008. ISSN 0028-0836, 1476-4687. doi: 10.1038/nature07127.

- [75] J. A. Schreier, A. A. Houck, Jens Koch, D. I. Schuster, B. R. Johnson, J. M. Chow, J. M. Gambetta, J. Majer, L. Frunzio, M. H. Devoret, S. M. Girvin, and R. J. Schoelkopf. Suppressing charge noise decoherence in superconducting charge qubits. *Physical Review B*, 77(18):180502, May 2008. ISSN 1098-0121, 1550-235X. doi: 10.1103/PhysRevB.77.180502.
- [76] Chad Rigetti, Jay M. Gambetta, Stefano Poletto, B. L. T. Plourde, Jerry M. Chow, A. D. Córcoles, John A. Smolin, Seth T. Merkel, J. R. Rozen, George A. Keefe, Mary B. Rothwell, Mark B. Ketchen, and M. Steffen. Superconducting qubit in a waveguide cavity with a coherence time approaching 0.1 ms. *Physical Review B*, 86(10):100506, September 2012. ISSN 1098-0121, 1550-235X. doi: 10.1103/PhysRevB.86.100506.
- [77] Lynden K. Shalm, Evan Meyer-Scott, Bradley G. Christensen, Peter Bierhorst, Michael A. Wayne, Martin J. Stevens, Thomas Gerrits, Scott Glancy, Deny R. Hamel, Michael S. Allman, Kevin J. Coakley, Shellee D. Dyer, Carson Hodge, Adriana E. Lita, Varun B. Verma, Camilla Lambrocco, Edward Tortorici, Alan L. Migdall, Yanbao Zhang, Daniel R. Kumor, William H. Farr, Francesco Marsili, Matthew D. Shaw, Jeffrey A. Stern, Carlos Abellán, Waldimar Amaya, Valerio Pruneri, Thomas Jennewein, Morgan W. Mitchell, Paul G. Kwiat, Joshua C. Bienfang, Richard P. Mirin, Emanuel Knill, and Sae Woo Nam. Strong Loophole-Free Test of Local Realism. *Physical Review Letters*, 115(25):250402, December 2015. ISSN 0031-9007, 1079-7114. doi: 10.1103/PhysRevLett.115.250402.
- [78] A. Wallraff, D. I. Schuster, A. Blais, L. Frunzio, R.-S. Huang, J. Majer, S. Kumar, S. M. Girvin, and R. J. Schoelkopf. Strong coupling of a single photon to a superconducting qubit using circuit quantum electrodynamics. *Nature*, 431(7005):162–167, September 2004. ISSN 0028-0836, 1476-4687. doi: 10.1038/nature02851.
- [79] Mathieu Pierre, Ida-Maria Svensson, Sankar Raman Sathyamoorthy, Göran Johansson, and Per Delsing. Storage and on-demand release of microwaves using superconducting resonators with tunable coupling. *Applied Physics Letters*, 104(23):232604, June 2014. ISSN 0003-6951, 1077-3118. doi: 10.1063/1.4882646.

- [80] Anthony Hey. *Feynman and Computation: Exploring the Limits of Computers*. CRC Press, 1 edition, March 2018. ISBN 978-0-429-50045-9. doi: 10.1201/9780429500459.
- [81] F. Motzoi, J. M. Gambetta, P. Rebentrost, and F. K. Wilhelm. Simple Pulses for Elimination of Leakage in Weakly Nonlinear Qubits. *Physical Review Letters*, 103(11):110501, September 2009. ISSN 0031-9007, 1079-7114. doi: 10.1103/PhysRevLett.103.110501.
- [82] Marissa Giustina, Marijn A. M. Versteegh, Sören Wengerowsky, Johannes Handsteiner, Armin Hochrainer, Kevin Phelan, Fabian Steinlechner, Johannes Kofler, Jan-Åke Larsson, Carlos Abellán, Waldimar Amaya, Valerio Pruneri, Morgan W. Mitchell, Jörn Beyer, Thomas Gerrits, Adriana E. Lita, Lynden K. Shalm, Sae Woo Nam, Thomas Scheidl, Rupert Ursin, Bernhard Wittmann, and Anton Zeilinger. Significant-Loophole-Free Test of Bell’s Theorem with Entangled Photons. *Physical Review Letters*, 115(25):250401, December 2015. ISSN 0031-9007, 1079-7114. doi: 10.1103/PhysRevLett.115.250401.
- [83] A. Wallraff, D. I. Schuster, A. Blais, J. M. Gambetta, J. Schreier, L. Frunzio, M. H. Devoret, S. M. Girvin, and R. J. Schoelkopf. Sideband Transitions and Two-Tone Spectroscopy of a Superconducting Qubit Strongly Coupled to an On-Chip Cavity. *Physical Review Letters*, 99(5):050501, July 2007. ISSN 0031-9007, 1079-7114. doi: 10.1103/PhysRevLett.99.050501.
- [84] G. de Lange, D. Ristè, M. J. Tiggelman, C. Eichler, L. Tornberg, G. Johansson, A. Wallraff, R. N. Schouten, and L. DiCarlo. Reversing Quantum Trajectories with Analog Feedback. *Physical Review Letters*, 112(8):080501, February 2014. ISSN 0031-9007, 1079-7114. doi: 10.1103/PhysRevLett.112.080501.
- [85] Nadav Katz, Matthew Neeley, M. Ansmann, Radoslaw C. Bialczak, M. Hofheinz, Erik Lucero, A. O’Connell, H. Wang, A. N. Cleland, John M. Martinis, and Alexander N. Korotkov. Reversal of the Weak Measurement of a Quantum State in a Superconducting Phase Qubit. *Physical Review Letters*, 101(20):200401, November 2008. ISSN 0031-9007, 1079-7114. doi: 10.1103/PhysRevLett.101.200401.

- [86] Nicholas A. Peters, Julio T. Barreiro, Michael E. Goggin, Tzu-Chieh Wei, and Paul G. Kwiat. Remote State Preparation: Arbitrary Remote Control of Photon Polarization. *Physical Review Letters*, 94(15):150502, April 2005. ISSN 0031-9007, 1079-7114. doi: 10.1103/PhysRevLett.94.150502.
- [87] Jay Gambetta, Alexandre Blais, D. I. Schuster, A. Wallraff, L. Frunzio, J. Majer, M. H. Devoret, S. M. Girvin, and R. J. Schoelkopf. Qubit-photon interactions in a cavity: Measurement-induced dephasing and number splitting. *Physical Review A*, 74(4):042318, October 2006. ISSN 1050-2947, 1094-1622. doi: 10.1103/PhysRevA.74.042318.
- [88] Yu Chen, C. Neill, P. Roushan, N. Leung, M. Fang, R. Barends, J. Kelly, B. Campbell, Z. Chen, B. Chiaro, A. Dunsworth, E. Jeffrey, A. Megrant, J. Y. Mutus, P. J. J. O'Malley, C. M. Quintana, D. Sank, A. Vainsencher, J. Wenner, T. C. White, Michael R. Geller, A. N. Cleland, and John M. Martinis. Qubit Architecture with High Coherence and Fast Tunable Coupling. *Physical Review Letters*, 113(22):220502, November 2014. ISSN 0031-9007, 1079-7114. doi: 10.1103/PhysRevLett.113.220502.
- [89] H. M. Wiseman and G. J. Milburn. *Quantum Measurement and Control*. Cambridge University Press, Cambridge, UK ; New York, 2010. ISBN 978-0-521-80442-4. OCLC: ocn434744599.
- [90] Harold Ollivier and Wojciech H. Zurek. Quantum Discord: A Measure of the Quantumness of Correlations. *Physical Review Letters*, 88(1):017901, December 2001. ISSN 0031-9007, 1079-7114. doi: 10.1103/PhysRevLett.88.017901.
- [91] P. Kurpiers, M. Pechal, B. Royer, P. Magnard, T. Walter, J. Heinsoo, Y. Salathé, A. Akin, S. Storz, J.-C. Besse, S. Gasparinetti, A. Blais, and A. Wallraff. Quantum Communication with Time-Bin Encoded Microwave Photons. *Physical Review Applied*, 12(4):044067, October 2019. ISSN 2331-7019. doi: 10.1103/PhysRevApplied.12.044067.
- [92] Peiyue Wang, Lupei Qin, and Xin-Qi Li. Quantum Bayesian rule for weak measure-

- ments of qubits in superconducting circuit QED. *New Journal of Physics*, 16(12):123047, December 2014. ISSN 1367-2630. doi: 10.1088/1367-2630/16/12/123047.
- [93] Alexander N. Korotkov. Quantum Bayesian approach to circuit QED measurement with moderate bandwidth. *Physical Review A*, 94(4):042326, October 2016. ISSN 2469-9926, 2469-9934. doi: 10.1103/PhysRevA.94.042326.
- [94] Christine Guerlin, Julien Bernu, Samuel Deléglise, Clément Sayrin, Sébastien Gleyzes, Stefan Kuhr, Michel Brune, Jean-Michel Raimond, and Serge Haroche. Progressive field-state collapse and quantum non-demolition photon counting. *Nature*, 448(7156):889–893, August 2007. ISSN 0028-0836, 1476-4687. doi: 10.1038/nature06057.
- [95] D. Tan, S. J. Weber, I. Siddiqi, K. Mølmer, and K. W. Murch. Prediction and Retrodiction for a Continuously Monitored Superconducting Qubit. *Physical Review Letters*, 114(9):090403, March 2015. ISSN 0031-9007, 1079-7114. doi: 10.1103/PhysRevLett.114.090403.
- [96] N. Bergeal, F. Schackert, M. Metcalfe, R. Vijay, V. E. Manucharyan, L. Frunzio, D. E. Prober, R. J. Schoelkopf, S. M. Girvin, and M. H. Devoret. Phase-preserving amplification near the quantum limit with a Josephson ring modulator. *Nature*, 465(7294):64–68, May 2010. ISSN 0028-0836, 1476-4687. doi: 10.1038/nature09035.
- [97] J. P. Groen, D. Ristè, L. Tornberg, J. Cramer, P. C. de Groot, T. Picot, G. Johansson, and L. DiCarlo. Partial-Measurement Backaction and Nonclassical Weak Values in a Superconducting Circuit. *Physical Review Letters*, 111(9):090506, August 2013. ISSN 0031-9007, 1079-7114. doi: 10.1103/PhysRevLett.111.090506.
- [98] Alison M. Yao and Miles J. Padgett. Orbital angular momentum: Origins, behavior and applications. *Advances in Optics and Photonics*, 3(2):161, June 2011. ISSN 1943-8206. doi: 10.1364/AOP.3.000161.
- [99] N. E. Frattini, V. V. Sivak, A. Lingenfelter, S. Shankar, and M. H. Devoret. Optimizing the Nonlinearity and Dissipation of a SNAIL Parametric Amplifier for Dynamic Range.

Physical Review Applied, 10(5):054020, November 2018. ISSN 2331-7019. doi: 10.1103/PhysRevApplied.10.054020.

- [100] M. Brune, E. Hagley, J. Dreyer, X. Maître, A. Maali, C. Wunderlich, J. M. Raimond, and S. Haroche. Observing the Progressive Decoherence of the “Meter” in a Quantum Measurement. *Physical Review Letters*, 77(24):4887–4890, December 1996. ISSN 0031-9007, 1079-7114. doi: 10.1103/PhysRevLett.77.4887.
- [101] P. Campagne-Ibarcq, P. Six, L. Bretheau, A. Sarlette, M. Mirrahimi, P. Rouchon, and B. Huard. Observing Quantum State Diffusion by Heterodyne Detection of Fluorescence. *Physical Review X*, 6(1):011002, January 2016. ISSN 2160-3308. doi: 10.1103/PhysRevX.6.011002.
- [102] Hanhee Paik, D. I. Schuster, Lev S. Bishop, G. Kirchmair, G. Catelani, A. P. Sears, B. R. Johnson, M. J. Reagor, L. Frunzio, L. I. Glazman, S. M. Girvin, M. H. Devoret, and R. J. Schoelkopf. Observation of High Coherence in Josephson Junction Qubits Measured in a Three-Dimensional Circuit QED Architecture. *Physical Review Letters*, 107(24):240501, December 2011. ISSN 0031-9007, 1079-7114. doi: 10.1103/PhysRevLett.107.240501.
- [103] F. Lecocq, L. Ranzani, G. A. Peterson, K. Cicak, R. W. Simmonds, J. D. Teufel, and J. Aumentado. Nonreciprocal Microwave Signal Processing with a Field-Programmable Josephson Amplifier. *Physical Review Applied*, 7(2):024028, February 2017. ISSN 2331-7019. doi: 10.1103/PhysRevApplied.7.024028.
- [104] M. Pechal, L. Huthmacher, C. Eichler, S. Zeytinoglu, A. A. Abdumalikov, S. Berger, A. Wallraff, and S. Philipp. Microwave-Controlled Generation of Shaped Single Photons in Circuit Quantum Electrodynamics. *Physical Review X*, 4(4):041010, October 2014. ISSN 2160-3308. doi: 10.1103/PhysRevX.4.041010.
- [105] Frank Pobell. *Matter and Methods at Low Temperatures*. Springer, Berlin ; New York, 3rd, rev. and expanded ed edition, 2007. ISBN 978-3-540-46356-6.
- [106] S. J. Weber, A. Chantasri, J. Dressel, A. N. Jordan, K. W. Murch, and I. Siddiqi.

- Mapping the optimal route between two quantum states. *Nature*, 511(7511):570–573, July 2014. ISSN 0028-0836, 1476-4687. doi: 10.1038/nature13559.
- [107] C. Monroe, R. Raussendorf, A. Ruthven, K. R. Brown, P. Maunz, L.-M. Duan, and J. Kim. Large-scale modular quantum-computer architecture with atomic memory and photonic interconnects. *Physical Review A*, 89(2):022317, February 2014. ISSN 1050-2947, 1094-1622. doi: 10.1103/PhysRevA.89.022317.
- [108] D. Ristè, J. G. van Leeuwen, H.-S. Ku, K. W. Lehnert, and L. DiCarlo. Initialization by Measurement of a Superconducting Quantum Bit Circuit. *Physical Review Letters*, 109(5):050507, August 2012. ISSN 0031-9007, 1079-7114. doi: 10.1103/PhysRevLett.109.050507.
- [109] H. Bernien, B. Hensen, W. Pfaff, G. Koolstra, M. S. Blok, L. Robledo, T. H. Taminiau, M. Markham, D. J. Twitchen, L. Childress, and R. Hanson. Heralded entanglement between solid-state qubits separated by three metres. *Nature*, 497(7447):86–90, May 2013. ISSN 0028-0836, 1476-4687. doi: 10.1038/nature12016.
- [110] A. A. Houck, D. I. Schuster, J. M. Gambetta, J. A. Schreier, B. R. Johnson, J. M. Chow, L. Frunzio, J. Majer, M. H. Devoret, S. M. Girvin, and R. J. Schoelkopf. Generating single microwave photons in a circuit. *Nature*, 449(7160):328–331, September 2007. ISSN 0028-0836, 1476-4687. doi: 10.1038/nature06126.
- [111] E. Flurin, N. Roch, F. Mallet, M. H. Devoret, and B. Huard. Generating Entangled Microwave Radiation Over Two Transmission Lines. *Physical Review Letters*, 109(18):183901, October 2012. ISSN 0031-9007, 1079-7114. doi: 10.1103/PhysRevLett.109.183901.
- [112] Joseph M. Lukens and Pavel Lougovski. Frequency-encoded photonic qubits for scalable quantum information processing. *Optica*, 4(1):8, January 2017. ISSN 2334-2536. doi: 10.1364/OPTICA.4.000008.
- [113] Mazyar Mirrahimi, Zaki Leghtas, Victor V Albert, Steven Touzard, Robert J Schoelkopf, Liang Jiang, and Michel H Devoret. Dynamically protected cat-qubits:

- A new paradigm for universal quantum computation. *New Journal of Physics*, 16(4): 045014, April 2014. ISSN 1367-2630. doi: 10.1088/1367-2630/16/4/045014.
- [114] D. Ristè, M. Dukalski, C. A. Watson, G. de Lange, M. J. Tiggelman, Ya. M. Blanter, K. W. Lehnert, R. N. Schouten, and L. DiCarlo. Deterministic entanglement of superconducting qubits by parity measurement and feedback. *Nature*, 502(7471):350–354, October 2013. ISSN 0028-0836, 1476-4687. doi: 10.1038/nature12513.
- [115] Klaus Mattle, Harald Weinfurter, Paul G. Kwiat, and Anton Zeilinger. Dense Coding in Experimental Quantum Communication. *Physical Review Letters*, 76(25):4656–4659, June 1996. ISSN 0031-9007, 1079-7114. doi: 10.1103/PhysRevLett.76.4656.
- [116] L.-M. Duan and C. Monroe. *Colloquium* : Quantum networks with trapped ions. *Reviews of Modern Physics*, 82(2):1209–1224, April 2010. ISSN 0034-6861, 1539-0756. doi: 10.1103/RevModPhys.82.1209.
- [117] J. Wenner, Yi Yin, Yu Chen, R. Barends, B. Chiaro, E. Jeffrey, J. Kelly, A. Megrant, J. Y. Mutus, C. Neill, P. J. J. O’Malley, P. Roushan, D. Sank, A. Vainsencher, T. C. White, Alexander N. Korotkov, A. N. Cleland, and John M. Martinis. Catching Time-Reversed Microwave Coherent State Photons with 99.4% Absorption Efficiency. *Physical Review Letters*, 112(21):210501, May 2014. ISSN 0031-9007, 1079-7114. doi: 10.1103/PhysRevLett.112.210501.
- [118] N. Bergeal, R. Vijay, V. E. Manucharyan, I. Siddiqi, R. J. Schoelkopf, S. M. Girvin, and M. H. Devoret. Analog information processing at the quantum limit with a Josephson ring modulator. *Nature Physics*, 6(4):296–302, April 2010. ISSN 1745-2473, 1745-2481. doi: 10.1038/nphys1516.
- [119] D. I. Schuster, A. Wallraff, A. Blais, L. Frunzio, R.-S. Huang, J. Majer, S. M. Girvin, and R. J. Schoelkopf. Ac Stark Shift and Dephasing of a Superconducting Qubit Strongly Coupled to a Cavity Field. *Physical Review Letters*, 94(12):123602, March 2005. ISSN 0031-9007, 1079-7114. doi: 10.1103/PhysRevLett.94.123602.
- [120] N. E. Frattini, U. Vool, S. Shankar, A. Narla, K. M. Sliwa, and M. H. Devoret. 3-wave

- mixing Josephson dipole element. *Applied Physics Letters*, 110(22):222603, May 2017. ISSN 0003-6951, 1077-3118. doi: 10.1063/1.4984142.
- [121] M. Żukowski, A. Zeilinger, M. A. Horne, and A. K. Ekert. “Event-ready-detectors” Bell experiment via entanglement swapping. *Physical Review Letters*, 71(26):4287–4290, December 1993. ISSN 0031-9007. doi: 10.1103/PhysRevLett.71.4287.
- [122] C. W. Gardiner. Driving a quantum system with the output field from another driven quantum system. *Physical Review Letters*, 70(15):2269–2272, April 1993. ISSN 0031-9007. doi: 10.1103/PhysRevLett.70.2269.
- [123] Matthew Reagor, Wolfgang Pfaff, Christopher Axline, Reinier W. Heeres, Nissim Ofek, Katrina Sliwa, Eric Holland, Chen Wang, Jacob Blumoff, Kevin Chou, Michael J. Hatridge, Luigi Frunzio, Michel H. Devoret, Liang Jiang, and Robert J. Schoelkopf. Quantum memory with millisecond coherence in circuit QED. *Physical Review B*, 94(1):014506, July 2016. ISSN 2469-9950, 2469-9969. doi: 10.1103/PhysRevB.94.014506.
- [124] A. A. Clerk and D. Wahyu Utami. Using a qubit to measure photon-number statistics of a driven thermal oscillator. *Physical Review A*, 75(4):042302, April 2007. ISSN 1050-2947, 1094-1622. doi: 10.1103/PhysRevA.75.042302.
- [125] Daniel Sank, Zijun Chen, Mostafa Khezri, J. Kelly, R. Barends, B. Campbell, Y. Chen, B. Chiaro, A. Dunsworth, A. Fowler, E. Jeffrey, E. Lucero, A. Megrant, J. Mutus, M. Neeley, C. Neill, P. J. J. O’Malley, C. Quintana, P. Roushan, A. Vainsencher, T. White, J. Wenner, Alexander N. Korotkov, and John M. Martinis. Measurement-Induced State Transitions in a Superconducting Qubit: Beyond the Rotating Wave Approximation. *Physical Review Letters*, 117(19):190503, November 2016. ISSN 0031-9007, 1079-7114. doi: 10.1103/PhysRevLett.117.190503.
- [126] Raphaël Lescanne, Lucas Verney, Quentin Ficheux, Michel H. Devoret, Benjamin Huard, Mazyar Mirrahimi, and Zaki Leghtas. Escape of a Driven Quantum Josephson Circuit into Unconfined States. *Physical Review Applied*, 11(1):014030, January 2019. ISSN 2331-7019. doi: 10.1103/PhysRevApplied.11.014030.

- [127] L. Olislager, J. Cussey, A. T. Nguyen, P. Emplit, S. Massar, J.-M. Merolla, and K. Phan Huy. Frequency-bin entangled photons. *Physical Review A*, 82(1):013804, July 2010. ISSN 1050-2947, 1094-1622. doi: 10.1103/PhysRevA.82.013804.
- [128] D. F. Walls and G. J. Milburn. *Quantum Optics*. Springer, Berlin, 2nd ed edition, 2008. ISBN 978-3-540-28573-1.
- [129] S. Shankar, M. Hatridge, Z. Leghtas, K. M. Sliwa, A. Narla, U. Vool, S. M. Girvin, L. Frunzio, M. Mirrahimi, and M. H. Devoret. Autonomously stabilized entanglement between two superconducting quantum bits. *Nature*, 504(7480):419–422, December 2013. ISSN 0028-0836, 1476-4687. doi: 10.1038/nature12802.
- [130] P. G. Kwiat, A. M. Steinberg, and R. Y. Chiao. High-visibility interference in a Bell-inequality experiment for energy and time. *Physical Review A*, 47(4):R2472–R2475, April 1993. ISSN 1050-2947, 1094-1622. doi: 10.1103/PhysRevA.47.R2472.